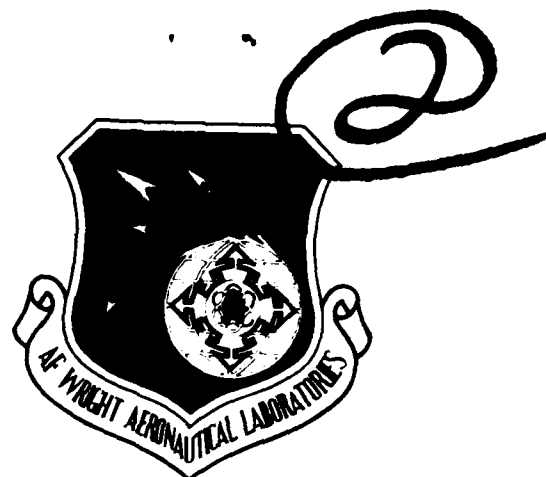AFWAL-TR-81-1294

ELECTRON DEVICE CONTACT STUDIES

Philip E. Wigen

Marlin O. Thurston

The Ohio State University Research Foundation
1314 Kinnear Road
Columbus, Ohio 43212

May 1982

Final Report - November 1, 1976 - March 31, 1981

Approved for public release; distribution unlimited.

DTIC
ELECTED
JUL 7 1982
D

82 07 07 082

NOTICE

This report has been reviewed by the Office of Public Affairs (ASD/PA), and is releasable to the National Technical Information Service (NTIS). At NTIS, it will be available to the general public, including foreign nations.

This technical report has been reviewed and is approved for publication.

MILLARD G. MIER, Project Engineer
Electronic Research Branch

FOR THE COMMANDER

PHILIP E. STOVER, Chief
Electronic Research Branch
Avionics Laboratory

REPORT DOCUMENTATION PAGE		READ INSTRUCTIONS BEFORE COMPLETING FORM
1. REPORT NUMBER AFWAL-TR- 31-1294	2. GOVT ACCESSION NO. AD-A116 656	3. RECIPIENT'S CATALOG NUMBER
4. TITLE (and Subtitle) ELECTRON DEVICE CONTACT STUDIES		5. TYPE OF REPORT & PERIOD COVERED Final Report Nov 1, 1976 - March 31, 1981
		6. PERFORMING ORG. REPORT NUMBER 764596/710525-710526
7. AUTHOR(s) Philip E. Wigen and Marlin O. Thurston		8. CONTRACT OR GRANT NUMBER(s) F33615-77-C-1002
9. PERFORMING ORGANIZATION NAME AND ADDRESS The Ohio State University Research Foundation, 1314 Kinnear Road Columbus, Ohio 43212		10. PROGRAM ELEMENT, PROJECT, TASK AREA & WORK UNIT NUMBERS 2305/R1/70
11. CONTROLLING OFFICE NAME AND ADDRESS AFWAL/AADR Wright-Patterson Air Force Base, Ohio 45433		12. REPORT DATE May 1982
		13. NUMBER OF PAGES 148
14. MONITORING AGENCY NAME & ADDRESS(If different from Controlling Office)		15. SECURITY CLASS. (of this report) Unclassified
		15a. DECLASSIFICATION/DOWNGRADING SCHEDULE

16. DISTRIBUTION STATEMENT (of this Report)

Approved for public release; distribution unlimited.

17. DISTRIBUTION STATEMENT (of the abstract entered in Block 20, if different from Report)

18. SUPPLEMENTARY NOTES

19. KEY WORDS (Continue on reverse side if necessary and identify by block number)

Contacts, Gallium Arsenide, Ohmic, Tunneling

20. ABSTRACT (Continue on reverse side if necessary and identify by block number)

This report describes the initial half of a program of investigation and characterization of contacts made to GaAs. A theoretical model of contact behavior based on electron tunneling is adapted to GaAs and will be used to compare experimental results of Au contacts fabricated on Sn diffused, n-type, GaAs surface layers. The fabrication of n-type layers using spin-on dopant sources and a semi closed chamber, in an open tube diffusion process are explained. The characterization of contact performance with a value of
(continued)

20   (Abstract) continued

specific contact resistance, R_c, and the measurement of R_c using
the transfer length method are covered.   Investigation into In-au
GaAs alloyed type contacts is also presented.

PREFACE

The research report contained herein was supported by the Avionics Laboratory, Wright-Patterson Air Force Base, Ohio, under Contract No. 33615-77-C-1002, "Electron Device Contact Studies." Research described in Sections I-VI was performed at The Ohio State University, Department of Electrical Engineering. Research covered in Section VII was performed at The Ohio State University, Department of Physics. This report covers a period from November 1, 1979 to June 30, 1981.

The main objective of this research program is to investigate the fabrication of low resistance contacts to gallium arsenide (GaAs) and to examine their behavior with respect to theoretical models. This report covers the background theory used in the modeling of the contacts and gives the processing steps developed for the fabrication of Au-GaAs contacts.

Accession For		
NTIS GRA&I	☒	
DTIC TAB	☐	
Unannounced	☐	
Justification		
By		
Distribution/		
Availability Codes		
Dist	Avail and/or Special	
A		

DTIC
COPY
INSPECTED
2

iii

TABLE OF CONTENTS

Table of Contents (Contd.)

LIST OF ILLUSTRATIONS

List of Illustrations (Contd.)

viii

List of Illustrations (concluded)

LIST OF TABLES

SECTION I
INTRODUCTION

1.1 Purpose and motivation for this research

There has been considerable recent interest in using GaAs as the basis for high speed electronic device applications. As with any practical device, making reliable contacts to the operating areas of the device is of utmost importance. An ideal contact, more specifically an ideal ohmic contact, is one which allows current to flow in either direction without presenting to the carriers any resistance at the interface. If the interface is not ideal, the contact can still be considered ohmic if the resistance is small and the potential drop developed across the interface is essentially linear with respect to the current.

In practice, a potential barrier is nearly always present at the interface and presents an impediment to the current flow preventing the contact from being ideally ohmic. Often the contact is highly non-ohmic or rectifying as a result of a non-linear current-voltage (I-V) characteristic. The object of contact studies is to determine where contact non-linearities arise and how they affect contact properties and to use that knowledge to minimize the effects of the barrier and to reduce interface resistance to as small a value as possible.

As will be discussed in detail later on, contacts which present little resistance to current through the interface are referred to as "ohmic contacts" and whatever resistance they do have can be related to the contact area by defining a quantity,"specific contact resistivity", R_c. The units are usually in $\Omega\text{-cm}^2$ and, for a contact of given area, the resistance the contact presents to current flow can be easily determined. Ideally R_c is zero, but practically R_c is very small, $\sim 10^{-6}$ $\Omega\text{-cm}^2$, in typical contacts being made today.

The difficulty is that when most metals are applied to make a contact to a semiconductor a potential barrier forms at the interface. Commonly this potential barrier causes the current to be a non-linear function of applied bias voltage and an R_c can be defined only in a piece-wise sense. The usual assumption is that ohmic contacts in the presence of such a barrier are made possible by quantum mechanical tunneling through the barrier. In such a case the barrier ceases to be significant and low values of R_c may result.

1

Tunneling is initiated in a metal-semiconductor (MS) contact by doping the semiconductor area beneath the contact to a high concentration. This high doping causes the formation of a very thin space charge region. If the doping is high enough to reduce the space charge region to a thickness of a few lattice constants, tunneling can occur.

The literature on ohmic contacts to GaAs is quite extensive and the amount of supporting and related literature on contacts to other semiconductors, especially Si, is even larger. Several particularly useful reviews have been given by Rideout (1), Yoder (2), and Eckhardt (3) with an introductory textbook-monograph having been written by Rhoderick (4).

Research on the theory of metal-semiconductor (MS) interfaces and their current transport characteristics is usually considered to have begun with the work of Mott (5) and Schottky (6). The diffusion theory of Schottky and the thermionic emission theory of Bethe (7) were subsequently combined into the modern thermionic emission-diffusion theory by Crowell and Sze (8). A good explanation of the essentials of all the above can be found in Sze (9).

The above research was concerned with MS contacts in which emission over the barrier is the dominant mechanism. Ohmic contacts, on the other hands, are related to carriers tunneling through interface potential barriers. A classic reference for this type of tunneling is given by Nordheim (10) . The most extensive theoretical work on the I-V characteristics of MS tunneling contacts is found in the papers of Padovani and Stratton (11), Crowell and Rideout (12) and Chang and Sze (13). Padovani (14) gives a good summary, with additions and corrections, of the work of Padovani and Stratton. Using the above, Yu (15) formulated the basic theoretical development of the specific contact resistivity of tunneling MS contacts. Change, et. al. (16) also performed a numerical analysis for R_c based on Chang and Sze (13).

The initial experimental work on developing alloyed type ohmic contacts to GaAs was performed by Cox and Strack (17). Since that time, various "recipes" for making ohmic contacts have been examined. The usual technique utilizes the alloying of a Au-Ge contact mixture into the GaAs surface (18-22). The Ge is believed to move into the GaAs surface thereby creating a highly doped region which forms a thin space charge layer through which electrons can tunnel. Usually the alloying is performed thermally but laser annealing and electron beam annealing (3) are receiving much current interest. Ion implantation has also been tried (23).

Even though alloying results in good ohmic contacts with low R_c, many problems associated with alloying are present. Some arise from the non-uniform way in which the alloying occurs (19). However, the most serious problems arise from the redistribution of the Au, Ge, and Ga during the alloying (21, 24-26). This redistribution can occur to

quite a large depth into the semiconductor and has severe implications
if alloying is used for contacts to the thin electronic structures
employed in advanced integrated circuits. This problem has initiated
much recent research into the possibility of making ohmic contacts via
a non-alloying approach (27-30). The research described in this report
deals in part with the possibility of fabricating a non-alloyed, low
R_c, contact to GaAs using a Sn diffusion.

One large problem with experimental research up to this point is
that beyond giving "recipes", little work has been done in trying to
determine whether the low values of R_c are in fact due to tunneling
through the barrier. There are other possibile schemes whereby low
R_c's might be obtained, especially since the alloying step can
drastically alter the morphology of the interface. Part of the problem
lies in the fact that after fabrication of a low R_c contact via
alloying, the data necessary to relate contact performance, namely R_c
and current-voltage (I-V) response, to theory is difficult to obtain.
The data needed are primarily the potential barrier height, ϕ_B, at the
interface and the semiconductor doping, N_D, beneath the contact. The
value of N_D especially is almost impossible to determine after the
alloyed contact has been fabricated.

Models have been developed in which the tunneling I-V response
of MS contacts can be theoretically determined. The main thrust of
this research was to attempt to relate experimental performance of some
non-alloyed Au-GaAs contacts to those models to see whether they can
accurately predict contact behavior. If so, then contact performance
can indeed be assumed to be due to tunneling phenomena and, more im-
portantly, the use of such models in predicting contact performance
under various conditions is justified. The application of an accurate
model in the attempt to fabricate contacts that are even more ideally
ohmic would allow a somewhat more scientific approach to be taken
rather than the "hit and miss recipe" approach now often used.

1.2 Fabrication procedure

In this research, since a comparison to theoretical models was
desired, the fabrication process needed to be one which allowed the
important parameters of ϕ_B and N_D to be determined accurately. This
meant that the normal approach of making contacts via alloying could
not be used. The method decided upon was based on highly doping the
GaAs surface so that carrier tunneling was expected but doing so by
diffusing the dopant into the surface first and then applying the con-
tact metal. This method of fabrication was a two-step process instead
of a single step alloying but, of utmost importance, it allowed the
determination of the N_D parameter before the contact was actually made,
and therefore allowed for accurate comparisons between theoretical
predictions and analysis. It was, of course, necessary that the
application of the metal should not affect the doping at depths
critical for tunneling.

3

The diffusion of Sn into a p-type GaAs wafer was used to create an n-type surface layer with a high value of surface dopant concentration, C_s, and since C_s is large, a thin space charge region is formed and tunneling can occur. The theoretical treatment is actually based on the assumption of uniform dopant distribution, N_D, beneath the contact. However, even though the actual dopant distribution has a definite profile, with C_s indicating dopant concentration only at the surface, the value of C_s can be substituted for N_D in the theoretical equations with little error. This is done in this research, but both C_s and N_D symbols will still be used since it is desirable at times to keep clear the designation between actual dopant profile and theoretical assumption.

The choice of a p-type substrate was based on the desire to form a thin, isolated layer for conduction, allowing easy determination of the data needed to calculate C_s and R_c.

1.3 Data collection and interpretation

To determine the value of C_s for the diffused layer, a van der Pauw measurement was performed and a value of diffused layer sheet resistivity was obtained. Junction lapping and staining was then used to determine layer thickness. From the above data a value of average resistivity for the layer, $\bar{\rho}$, could be determined. An "Irvin curve", a theoretical curve relating $\bar{\rho}$ of the diffused n-type layer to the value of C_s, was developed and used with the measured $\bar{\rho}$ to determine an experimental value for C_s.

To develop the value of ϕ_B, curve fitting of experimental contact I-V data to theoretical equations for the contact I-V response was performed. The curve fitting yeilds both ϕ_B and C_s parameters and allowed a check on the value of C_s as determined from the $\bar{\rho}$ measurements.

Using the values of ϕ_B and C_s as obtained above, theoretical values of R_c were calculated. As a more complete check on the applicability of the model, the variation of R_c with temperature was predicted theoretically and then compared to experimental R_c vs. T data.

The above model and procedures were also applied to the analysis of annealed-alloyed Au-Sn diffused layer contacts and also to annealed-alloyed Au-Ge contacts. Values of ϕ_B and C_s were calculated and compared as a function of annealing time and temperature. This part of the research program was performed to see whether the model used in the analysis of non-alloyed contacts could also be usefully applied to understanding what changes alloyed contacts undergo as they are fabricated and why these changes result in the contact eventually exhibiting improved ohmic behavior.

4

BLANK PAGE

SECTION II

THEORETICAL BACKGROUND

2.1   Ohmic contacts

A discussion of contact performance and ohmic contacts must first clarify the meaning of the word "ohmic". To define the term it is necessary to consider the structure of the metal-semiconductor (MS) interface.

The joining of a metal and a semiconductor causes the formation of a potential barrier at the interface. Figure 2.1 shows the band diagram of a MS contact on a moderately doped semiconductor. This type of barrier is commonly referred to as a Schottky barrier. In the figure, E_c and E_v represent semiconductor conduction and valence bands, respectively. The Fermi level energy is E_F. The potential barrier height is given by ϕ_B and the space charge region width is W.

Classically ϕ_B is determined from:

$$\phi_B = \phi_M - X_S \quad , \tag{2.1}$$

where ϕ_M is the metal work function and X_S is the electron affinity of the semiconductor (63). If $\phi_M > \phi_S$, where ϕ_S is the semiconductor work function, the barrier of Fig. 2.1 results. This type of barrier presents an impediment to current flow and even for relatively low values of current, rather large voltage drops appear across the interface. If, at this point, a piecewise linear approximation of the contact I-V response is made, these large voltage crops result in a large contact resistance.

If $\phi_M < \phi_S$, ϕ_B can become zero or even negative. For such a case the carriers crossing the junction see essentially no resistance since no barrier exists. Therefore, the potential drop across the junction is very small, ideally going to zero. Such a contact has zero contact resistance and is the classical definition of an "ohmic" contact. (For the above discussion, a MS contact to an n-type semiconductor was illustrated. For a p-type semiconductor similar barriers to hole flow will result but for the opposite conditions of ϕ_M and ϕ_S. Since that treatment is analogous, and since n-type samples were used in this research, only n-type examples will be discussed further.)

7
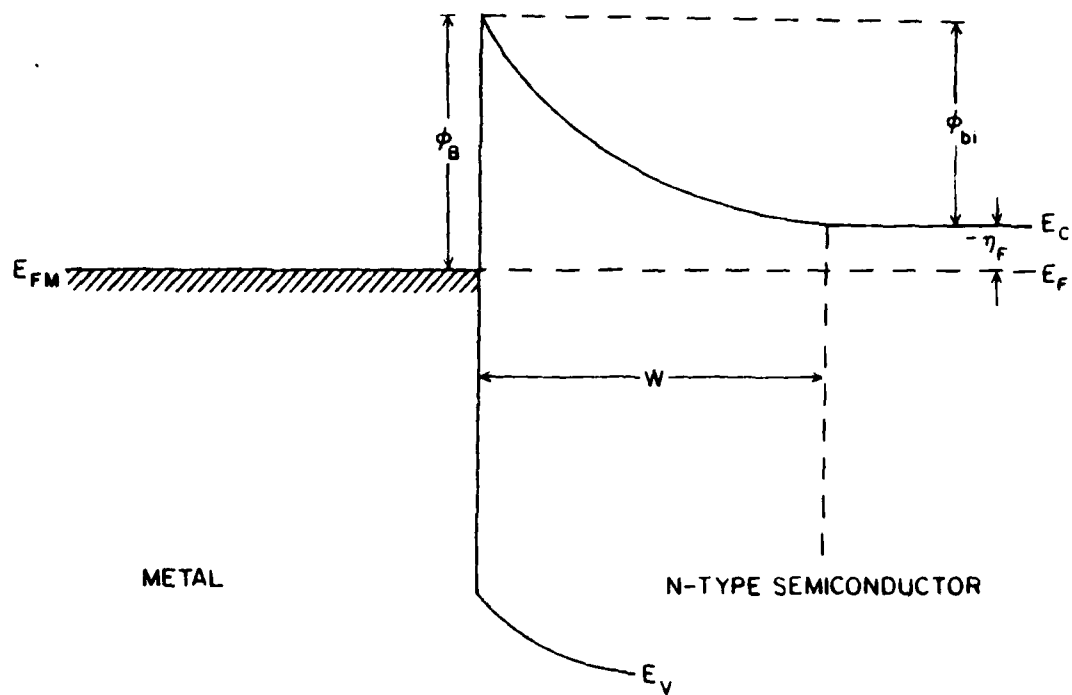
Figure 2.1 Schottky barrier contact on a
moderately doped, n-type
semiconductor

8

For device fabrication, the most desirable contacts are ohmic contacts as the word is defined above. However, for most practical combinations of metals and semiconductors the ϕ_M, X_S relation is in a direction to produce a barrier. Moreover, other effects such as surface states act to pin the Fermi level at a fixed position resulting in a ϕ_B independent of ϕ_M or X_S (31-35). For such cases the formation of a Schottky barrier is inevitable. However, ohmic contacts can still result from other conduction mechanisms, but the word "ohmic" takes on a slightly different meaning.

In the most general case of contacts to devices, the goal is to have the voltage drop across the contact interface much smaller than the voltage drop across the bulk region of the device. In this way the contact properties or contact I-V response do not affect overall device performance. In addition, the I-V response of the contact should be essentially resistive or linear. However, the description of "ohmic" now becomes a relative one, being compared to the bulk resistance of the device itself. This viewpoint is useful and for many practical contacts is perfectly valid in characterizing them as being ohmic.

2.2 Contact resistivity

A more quantitative way to describe contact performance as it relates to ohmicity is in terms of contact resistivity, R_c, which is usually given in units of Ω-cm^2. The definition of R_c implies that the effects of the contact interface on carrier flow can be lumped into a distributed resistance. If the I-V response of the interface is fairly linear, the value of R_c is applicable over a wide range of contact voltage drops. If the I-V response is non-linear, then the R_c value is strictly applicable at only one particular value of I and V. In most cases, the value of R_c is fairly low, making the voltages drop across the contact small, and typical contact I-V response over this region of voltage drops is fairly linear.

Lower values of R_c are, of course, desirable. When contact current flow is perpendicular to the interface, the actual resistance of a contact of given area, A, can be determined from:

$$R_{CONT} = \frac{R_c}{A} \qquad . \qquad (2.2)$$

The voltage drop across the contact can then be calculated from:

$$V_{CONT} = I R_{CONT} \qquad . \qquad (2.3)$$

For current flow in a planar contact, or other structure where current flow is not all perpendicular to the interface, equation (2.3) usually cannot be applied directly. In such cases current crowding effects are present and a different method must be used to relate the value of V_{CONT} to the values of I and R_c (36-37). However, even in such cases the concept of R_c is valid and is the best way to characterize contact

performance at the interface level. Therefore, in current terminology, "ohmic" contacts refers to contacts with sufficiently small R_c values. Values of R_c in the range of $10^{-3} \Omega\text{-cm}^2$ to $10^{-6}\Omega^2$ are those most often referred to in the literature as being ohmic (17-23, 27-31).

2.3 Practical ohmic contacts

In section 2.1 it was stated that for most cases of MS contacts a positive ϕ_B will be formed. For Au-n-type GaAs contacts, other workers have measured a ϕ_B in the range of 0.8 to 1.0 eV, with 0.9 eV being the value most often reported (31-35). The value of ϕ_B is usually observed to be constant and independent of GaAs doping level implying that the Fermi level is pinned due to the action of surface states.

A simple model explaining Fermi level pinning as being due to surface states has been developed by Bardeen (38). There is still some question as to whether the surface states are intrinsic or whether they are induced by the deposition of the contact metal but, the important point is that when an Au contact is made to GaAs a Schottky barrier with $\phi_B \approx 0.9$ eV can be expected. Subsequently, such a barrier will result in a poor contact unless it is thin enough to allow carrier tunneling.

For a MS contact with a barrier height ϕ_B , the width of the insulating space charge layer beneath the contact is given by:

$$ W = \left[\frac{2\varepsilon}{qN_D} \left(V_{bi} - \frac{kT}{q} \right) \right]^{1/2} , \qquad (2.4) $$

where ε = semiconductor permittivity = $\varepsilon_r \varepsilon_0$

q = electronic charge

N_D = semiconductor donor density

k = Boltzmann's constant

T = temperature

V_{bi} = built in voltage (barrier height as seen by electrons in conduction band of the semiconductor)

$V_{bi} = \phi_B + n_F$

n_F = Fermi potential = $E_F - E_c$

or if $n_B \gg n_F$, $\frac{kT}{q}$ as is the usual case,

$$W \approx \left[\frac{2\epsilon}{qN_D} (\phi_B) \right]^{1/2} . \qquad (2.5)$$

For moderate dopings, W is too large to allow electrons to tunnel and any flow must be over the barrier. Such a contact exhibits rectification and the I-V response of the contact is given by the familiar diode equation:

$$J = A \exp \left(-\frac{\phi_B}{kT} \right) \left[\exp \left(\frac{qV}{kT} \right) - 1 \right]^{1/2} , \qquad (2.6)$$

where

$$A = \text{Richardson's constant} = \frac{4\pi m^*(kT)^2}{h^3} \qquad (2.7)$$

h = Plank's constant
m^* = electron effective mass

For contacts with a given I-V response, the value of specific contact resistivity R_C is defined, in the limit as contact voltage goes to zero, as:

$$R_C = \left. \frac{dV}{dJ} \right|_{v \to o} \qquad (2.8)$$

or equivalent, since the I-V response is single valued in J for all V,

$$R_C = \left[\frac{dV}{dJ} \right]^{-1}_{v \to o} \qquad (2.9)$$

Applying the definition of R_C to the diode equation, applicable for semiconductors with moderate doping, results in values for R_C on the order of kilo-ohms-cm^2. The incremental resistance is, of course, in parallel with a depletion layer capacitance and the result is clearly not a useful contact characteristic.

However, if the doping, N_D, is large, the band diagram as seen in Figure 2.2 is present. The barrier slope is quite steep and W is very small. For values of W on the order of a few lattice spacings, electrons can quantum mechanically tunnel through the barrier under an applied voltage and give rise to a current. The tunneling currents can be quite large even for a small contact voltage drop and therefore the resistance of the contact can be quite low.

11
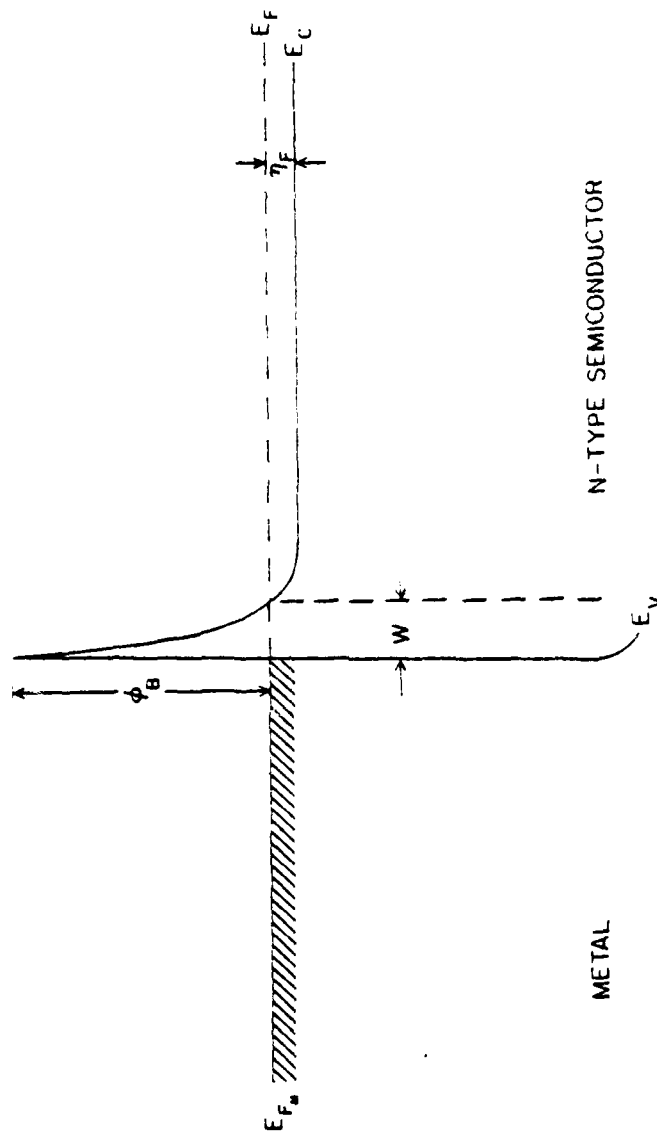
Figure 2.2   Schottky barrier contact on a heavily
doped (degenerate), n-type semiconductor

12

Theoretical equations giving the I-V response of tunneling contacts have been developed by various authors such as Padovani and Stratton (11), Crowell and Rideout (12), and Change and Sze (13). Their results are all similar, but the work of Chang and Sze is based on a computer numerical solution, using Schroedinger's equation, with the least number of simplifying assumptions. Subsequently, Chang and Sze's results are not given in a closed analytical form and therefore, a closed expression for R_C cannot readily be developed from their graphs. It is easier to work from the results of Padovani and Stratton or Crowell and Pideout where I-V equations are given. The most comprehensive treatment of tunneling, outlining the development of the tunneling I-V equations, is given in Padovani (14). Here Padovani has taken the earlier work of himself and Stratton (11), as well as Stratton (39), and presented a more unified development. It is largely from this cource that the equations used in this research are taken and the development of these equations is reviewed herein.

2.4 General aspects of tunneling

The basis for the Development of the I-V response of a tunneling contact results on relating current flow to the probability of electron transmission through a thin potential barrier. The classic work of Nordheim (10) gives an expression:

$$P = \exp\left[-\frac{2(\phi_B - qV - n_F)}{3E_\infty}\right] , \qquad (2.10)$$

where P represents the transmission probability for an electron through a triangular potential barrier of total height $\phi_B - qV - n_F$. Where:

V = applied basis voltage
n_F = Fermi level referred to E_c

The term E_∞ represents a characteristic tunneling energy and is given by:

$$E_\infty = \frac{q\hbar}{2}\left[\frac{N_D}{\epsilon m^*}\right]^{1/2} , \qquad (2.11)$$

where $\hbar$ = Plank's constant $/2\pi$
N_D = Semiconductor doping
ϵ = Semiconductor permittivity
m^* = effective mass of the carrier (in this case an electron).

13

The tunneling current is proportional, in first order, to P and therefore has an exponential dependence on applied forward voltage. The energy E_∞ can be easily shown to be inversely proportional to the space charge width, W. A decrease in W, meaning a thinner barrier and increased probability for tunneling, results in a larger value for E_∞ which via the above also leads to a larger value of P. An increase in N_D results in a thinner space charge region, and as is obvious from Eq. (2.11) also increases E_∞. Also, since the electron effective mass, m^*, for an electron in GaAs is very small,

$$m^* = 0.068 \, m_0$$

where

$$m_0 = 9.1 \times 10^{-31} \, kg \, ,$$

(2.12)

the value for E_∞ in GaAs is much larger than for other semiconductors where m^* is larger, and therefore, for similar doping levels, electron tunneling is much more probable for barriers made to GaAs. This is why tunneling is believed to be the main mechanism giving rise to low resistance contacts to GaAs.

Even though a Schottky barrier can be approximated to first order as a triangular barrier, the actual relationship between electron tunneling and current flow is much more complex. The reason is that the electrons are distributed in a range of states throughout the conduction band and the contribution of all the electrons must be considered. The relationship between electron tunneling probability and current flow in the x direction is given by:

$$J = \frac{2q}{h^3} \, {}_0\!\int^\infty F_1(E_1) - F_2(E_1) \int P(E_1, p_y, p_z) dp_y \, dp_z \, dE_1$$

(2.13)

The subscripts 1 and 2 refer to the conductors where the electrons originate and where they are destined respectively. For a MS contact with an n-type semiconductor under forward bias, "1" represents the semiconductor and "2" represents the metal. The $F_1(E_1)$ and $F_2(E_1)$ are Fermi functions, predicting whether or not an electron state at energy E_1 is occupied. The transmission probability is $P(E_1, p_y, p_z)$ and the integration is performed over all energies and momenta in the conduction band.

One large problem in using the above equation lies with the formulation of P for a given barrier shape. For any specific barrier shape, an analytical solution of Eq. (2.13) using an extraction expression for P is extremely difficult. Instead, P is usually formulated using the WKB approximation which results in:

$$P = \exp \{-\frac{2}{h} \int_{x_1}^{x_2} [-(p_x)^2]^{1/2} \, d_x\}$$

The value of p_x is the x component of electron quasi-momentum in the space charge region. For a total momentum of $p^2 = p_x^2 + p_y^2 + p_z^2$, the transmission of electrons in the x direction is dependent on p_x. Letting $p_\perp^2 = p_y^2 + p_z^2$, Eq. (2.14) can then be rewritten as:

$$P = \exp - \frac{2}{h} \int_{x_1}^{x_2} (p_\perp^2 - p^2)^{1/2} d_x \quad . \tag{2.15}$$

The minus sign in $-(p_x)^2$ in Eq. (2.14) arises from the WKB approximation because between x_1 and x_2, the classical barrier turning points where $p_x = 0$, the value of p_x^2 is <0 since the electron is within a potential barrier $\phi(x)$, whose energy is larger than that of the tunneling electron.

One large analytical difficulty remains. The expression for $\ln P$, Eq. (2.15), is still difficult to use, as is, in Eq. (2.13). The simplification used to overcome this problem is to expand $\ln P$ into a Taylor series. This procedure has been done by Stratton et.al. (40), and results in a series for an expansion in $(p_\perp)^2$ of

$$-\ln P = b + \frac{(P_\perp)^2}{P_{01}^2} + K(p_\perp)^2 \tag{2.16}$$

with the coefficients b and P_{01} defined as:

$$b \equiv \frac{2}{h} \int_{x_1}^{x_2} \bar{p} \, d_x \tag{2.17}$$

$$P_{01}^2 \equiv \frac{1}{h} \int_{x_1}^{x_2} \frac{1}{\bar{p}} \, d_x \quad , \tag{2.18}$$

where $\bar{p} = -p^2$ (again since within the barrier region $p^2 < 0$). Since terms above $p_\perp^2$ will not be used, K need not be given.

The further simplification of Eq. (2.16) involves expanding b into a Taylor series around the energy level from which the electrons are tunneling. This will result in two different regions of operation, field emission (FE) and thermionic field emission (TFE) which will be treated separately in the following sections.

2.5 Field emission

In the case of field emission, the electrons tunnel from states around the semiconductor Fermi level, n_F, as shown in Figure 2.3. The applied forward bias is V and $\phi(x)$ is the potential barrier.
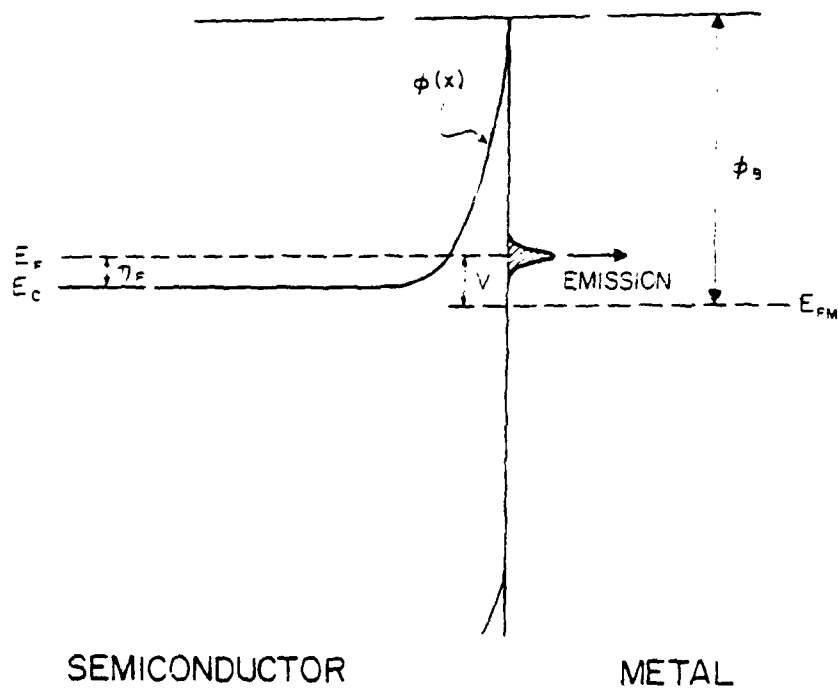
Figure 2.3 Electron tunneling under field emission for an
applied forward bias.

Since electrons are tunneling around n_F, the simplification for Eq. (2.16) is to expand b in terms of a Taylor series around the Fermi level (40). The series is given by:

$$b = b_1 + c_1(E-n_F) + f_1(E-n_F)^2 + \cdots \quad , \tag{2.19}$$

where the coefficients b, c_1, and f_1 are given by:

$$b_1 = b \Big|_{n_F} = \frac{2}{\hbar} \int_{x_1}^{x_2} (\bar{p})_{n_F} \, d_x \tag{2.20}$$

$$c_1 = \frac{2}{\hbar} \int_{x_1}^{x_2} (\frac{d\bar{p}}{d})_{n_F} \, d_x \quad , \tag{2.21}$$

$$f_1 = \frac{1}{\hbar} \int_{x_1}^{x_2} (\frac{d^2\bar{p}}{dE^2})_{n_F} \, d_x \tag{2.22}$$

and

$$\frac{1}{P_{01}^2} = \frac{1}{\hbar} \int_{x_1}^{x_2} (\frac{1}{\bar{p}})_{n_F} \, d_x \quad , \tag{2.23}$$

where all integrals are evaluated at $E = n_F$. Substitution of the coefficients into Eq. (2.19) and use of Eq. (2.19) in Eq. (2.16) and then in Eq. (2.13) for J gives:

$$J = \frac{2\pi q}{h^3} (P_{01})^2 \exp(-b_1) \int_0^\infty [F_1(E)-F_2(E)] \exp[-c_1(E-n_F)] \, dE$$

$$\times [1- \frac{1}{2\pi} \int_0^{2\pi} \exp(\frac{-P_M^2}{P_{01}^2}) \, dp] \tag{2.24}$$

which is valid as long as (42)

$$\frac{1}{kT} - c_1 < (2f_1)^{1/2} \quad . \tag{2.25}$$

The next step in the analysis is to choose the appropriate relationship between momentum, p, and energy, E, so the coefficients can be evaluated. The assumption used here is that of a parabolic energy-momentum relationship in all directions given by:

$$p^2 = 2m*(E-n_F) \quad . \tag{2.26}$$

17

For electrons tunneling through a barrier, $\phi(x)$, Eq. (2.26) becomes:

$$p^2 = 2m*(E - n_F - \phi) \tag{2.27}$$

and within the barrier (space charge layer) $E > n_F$ but $E < \phi$, therefore using $\bar{p}^{-2} = -p^2$ as the quasi momentum in the barrier:

$$\bar{p}^2 = 2m*[\phi - (E - n_F)] \tag{2.28}$$

It is from Eq. (2.28) that the coefficients p_{01}, b_1, c_1, and f_1 are determined. The ϕ term also includes a dependence on applied bias V.

Padovani (14) states that with the assumption of a parabolic energy-momentum relationship and with the assumption that m* can be used to describe the electron while it is tunneling through the barrier, for most values of applied voltage, energy levels, and barrier heights:

$$\frac{P_m^2}{P_{01}^2} = C_1 E \quad . \tag{2.29}$$

This relationship, if applied in Eq. (2.24), results in:

$$J = \frac{A}{(c_1 kT)^2} \exp(-b_1)\{ \frac{\pi c_1 kT}{\sin(\pi c_1 kT)} [1 - \exp(-c_1 qV)] - c_1 qV \exp(c_1 n_F)\} \tag{2.30}$$

valid when:

$$\exp\left| \frac{(n_F - qV)}{kT} \right| >> 1 \quad . \tag{2.31}$$

The previous Eq. (2.7) gives the value of the Richardson constant.

As seen from Eq. (2.31), the above expression for J is valid only for the case of small applied biases, and is somewhat less valid at room temperature (higher kT) than for lower temperatures where tunneling conduction is usually·considered to be dominant.

If

$$\exp\left| \frac{(n_F - qV)}{kT} \right| << 1 \tag{2.32}$$

as would be the case for larger forward biases, then Eq. (2.24) becomes:

$$J = \frac{A}{(c_1 kT)^2} \exp(-b_1)\left\{\frac{\pi c_1 kT}{\sin(\pi c_1 kT)} - (1+c_1 n_F)\exp(-c_1 n_F)\right\} \qquad (2.33)$$

The coefficient b_1, c_1, and f_1 used in Eq. (2.25) are the same for both Eq. (2.30) and Eq. (2.33), and must be determined after the shape of the potential barrier, $\phi(x)$ is defined. If a standard parabolic Schottky barrier of height ϕ_B formed on material with a doping of N_D is used as $\phi(x)$, then the coefficients becomes:

$$b_1 = \frac{n_F}{E_\infty}\left\{\left[\frac{(\phi_B - qV + n_F)^{1/2}(\phi_B - qV)^{1/2}}{n_F}\right]\right.$$

$$\left. -\ln\left\{\left[\frac{(\phi_B - qV + n_F)^{1/2}(\phi_B - qV)^{1/2}}{n_F^{1/2}}\right]\right\}\right\} \qquad (2.34)$$

$$c_1 = \frac{1}{E_\infty}\ln\left\{\left[\frac{(\phi_B - qV + n_F)^{1/2}(\phi_B - qV)^{1/2}}{n_F^{1/2}}\right]\right\} \qquad (2.35)$$

and

$$f_1 = \frac{1}{4E_\infty n_F}\left[\frac{\phi_B}{(\phi_B - n_F)}\right]^{1/2} . \qquad (2.36)$$

The term E_∞ is the characteristic tunneling energy and is given by Eq. (2.11). The applied voltage, V, is in volts, and all other energies E_∞, ϕ_B, n_F are given in joules.

In most practical cases $n_F \ll \phi_B - qV$ and therefore the coefficients will simplify to:

$$b_1 \approx \frac{\phi_B - qV}{E_\infty} , \qquad (2.37)$$

$$c_1 \approx \frac{\ln\left[\frac{4(\phi_B - qV)}{n_F}\right]}{2E_\infty} \qquad (2.38)$$

19

and

$$f_1 \approx \frac{1}{4E_\infty n_F} \tag{2.39}$$

The above coefficients are substituted in Eq. (2.30) or Eq. (2.33) to get the form of the I-V response for a given range of bias voltage.

For the case of large applied bias, (Eq. 2.33)) it is seen that the dominant term for the voltage response is the $\exp(qV/E_\infty)$ term. It is then possible to rewrite Eq. (2.33) as :

$$J = J_S \exp\left(\frac{qV}{E_\infty}\right) \tag{2.40}$$

where

$$J_S = \frac{A}{(c_1 k)^2} \exp\left(-\frac{\phi_B}{E_\infty}\right) \left\{ \frac{\pi q kT}{\sin(\pi q kT)} \right\} - (1 + c_1 n_F)\exp(-c_1 n_F)\} \tag{2.41}$$

with J_S representing a saturation current. Note that in this case J does not go to zero for $V = 0$. This is because, for low bias, Eq. (2.30) must be used instead, which does give $J = 0$ for $V = 0$. It is interesting to note the similarity between Eq. (2.30) and Eq. (2.10) from Nordheim. The same dependence on $\exp(qV/E)$ is seen, as well as the $\exp(-\phi_B/E_\infty)$ dependence which was incorporated into J_S in the above.

The theoretical definition of contact resistivity was given by Eq. (2.9) as:

$$R_C = \left[\frac{dJ}{dV}\right]^{-1}_{V \to 0} \tag{2.9}$$

Since R_C is given in the limit of $V \to 0$, the appropriate J-V equation to use to compute R_C is Eq. (2.30). This has been done by Yu (15) and the resulting equation giving R_C for a FE type contact is:

$$R_C = \frac{A\pi q}{kT\sin(\pi q kT)} \exp\left(-\frac{\phi_B}{E_\infty}\right) - \frac{Agq}{(c1kT)^2} eqp\left(-\frac{\phi_B}{E_\infty} - c_1 n_F)\right] \tag{2.42}$$

The coefficients b_1, c_1, and f_1 are also evaluated at $V = 0$ and are:

20

$$b_1 \approx \frac{\phi_B}{E_\infty} \,, \tag{2.43}$$

$$c_1 \approx \frac{\ln\left[\dfrac{4\phi_B}{n_F}\right]}{2E_\infty} \tag{2.44}$$

and

$$f_1 \approx \frac{1}{4E_\infty n_F} \tag{2.45}$$

With values of N_D and ϕ_B chosen, b_1, c_1, and f_1 are calculated and Eq. (2.25) is used to determine whether the contact is conducting in the FE range. If Eq. (2.25) is not satisfied then Eq. (2.42) cannot strictly be used.

Chang and Sze (13) have calculated theoretical I-V curves for a MS contact based on an equation similar to Eq. (2.13). However, they consider a total response of both tunneling and thermionic emission components together instead of treating separate areas of conduction as outlined with the conditions given by Eq. (2.25). They also solve for the transmission coefficient, $P(E)$, by a numerical integration of Schroedinger's equation within the barrier region. Their results are therefore not in closed form, as is Eq. (2.30) and Eq. (2.33), and cannot be used to directly derive an expression for R_c. However, they do make a comparison between their numerical solution for $P(E)$ and a WKB approximation for $P(E)$ and show that if electron tunneling occurs at points other than near the top of the barrier, the value of $P(E)$ as predicted by the WKB approximation is very close to the exact value. This means that the WKB approximation is valid over most of the range of doping, N_D, and applied bias, V, used in this research.

Change, Fang, and Sze (16) have made a numerical calculation of R_c based on the computer analysis of Chang and Sze and have presented curves giving R_c for various values of N_D and ϕ_B as well as curves of R_c vs. T for MS contacts ot GaAs. Their results, as expected, are very similar to the values of R_c as predicted by Eq. (2.42). The disadvantage of the computer calculation is the necessity of performing the tedious numerical integration for each change in parameter N_D, ϕ_B, or T. Therefore, the simplification in calculation and interpretation available with the use of Eq. (2.42) is worth whatever small loss of accuracy results from using the WKB approximation.

2.6 Thermonic field emission

If, for a particular choice of N_D, ϕ_B, and T, Eq. (2.25) is not satisfied, then the contact may be conducting in the thermionic field emission (TFE) range. This range can also be called thermally assisted tunneling. Figure 2.4 illustrated TFE conduction. The electrons are not being emitted from states around E_F, as they are in FE, but rather from states higher up in the band around a maximum, E_M.

The theoretical calculation of J for TFE involves the same procedure used in the base of FE, except that instead of expanding the Taylor series for P around E_F, it is expanded around E_M. Padpovani and Stratton (11), working from Stratton (41), performed such a calculation on a Schottky barrier with the results.

$$ J = \frac{A}{2\pi kT} \{\exp [(\frac{n_F}{kT})-b_M-(\frac{E_m}{kT})]\} \; (\frac{\pi}{f_m})^{1/2}[1-\mathrm{erf}(E_m f_m^{1/2}] \quad (2.46) $$

where E_m is the peak of the energy distribution of the emitted electrons and is given by:

$$ c_m kT = 1 \quad\quad (2.47) $$

[Note: Padovani and Stratton include an extra $\frac{1}{\pi}$ factor in Eq. (2.46) which is not in Stratton's original article.] Equation (2.46) is applicable to forward biases greater than a few kT/q.

The calculation of the coefficients b_m, c_m, and f_m follow analogously from the previous equations given for the FE case after an assumption as to the shape of the emitted electron distribution has been made. The assumption of a Gaussian distribution with half width:

$$ \Delta = (\ln 2)^{1/2} (\frac{1}{f_m^{1/2}}) \quad\quad (2.48) $$

was used by Padovani and Stratton (11) and for a forward biased Schottky barrier the coefficients were calculated to be :

$$ b_m = \frac{1}{E_\infty} [(\phi_B - qV + n_F)^{1/2}(\phi_B - qV + n_F + E_m)^{1/2} - \frac{E_\infty E_m}{kT}] , $$

$$ (2.49) $$

$$ c_m = \frac{1}{E_\infty} \ln \{ \frac{[(\phi_B - qV + n_F)^{1/2}(\phi_B - qV + n_F + E_m)^{1/2}]}{E_m^{1/2}} \} $$

$$ (2.50) $$
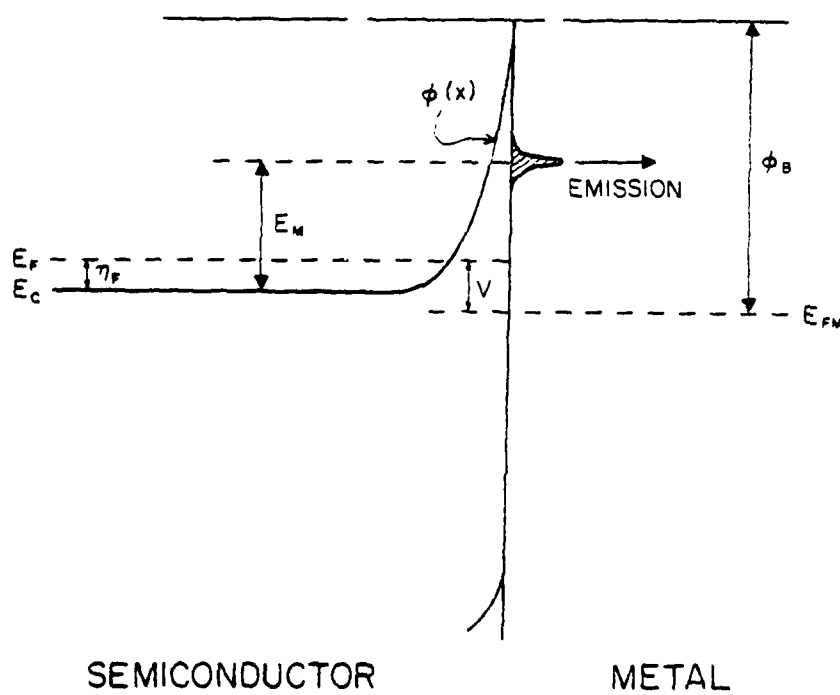
Figure 2.4 Electron tunneling under thermionic-fields
emission for an applied forward bias.

and

$$f_m = \frac{1}{4E_\infty E_m} \qquad (2.51)$$

with

$$E_m = \frac{(\phi_B - qV + n_F)}{\cosh^2\left(\dfrac{E_\infty}{kT}\right)} \qquad (2.52)$$

E_∞ being as defined before.

The use of the above is also limited to cases where E_m is between E_F and the top of the barrier. This gives conditions:

$$c_1 kT > 1 \qquad (2.53)$$

$$P(E_m) < \exp(-1) \qquad (2.54)$$

where c_1 is given by Eq. (2.38) and $P(E_m)$ is the transparency of the barrier at E_m. The condition of Eq. (2.54) is from Murphy and Good (42). Substituting the coefficients in Eq. (2.46) and neglecting the erf term gives:

$$J = J_s \exp\left(\frac{qV}{E_o}\right) \qquad (2.55)$$

where

$$E_o = E_\infty \coth\left(\frac{E_\infty}{kT}\right) \qquad (2.56)$$

and

$$J_s = \frac{A[\pi E_\infty(\phi_B - qV + n_F)]^{1/2}}{\cosh^2\left(\dfrac{E_\infty}{kT}\right)} \exp\left[\frac{n_F}{kT} - \frac{\phi_B + n_F}{E_o}\right] \qquad (2.57)$$

However, this equation is still applicable only for values of forward bias, V, greater than a few kT/q. It is clear that Eq. (2.55) does not result in J = 0 for V = 0.

A more recent development of the I-V response of an MS contact in the TFE region has been given by Crowell and Rideout (12). Using

24

assumptions similar to the above for the shape of the emitted electron distribution (Gaussian) and the region where TFE dominates, they give an equation which is written as:

$$J = J_S \exp\left(\frac{qV}{E_o}\right)\left[1 - \exp\left(\frac{qV}{kT}\right)\right] \qquad (2.58)$$

and

$$J_S \approx \frac{A}{kT} \frac{\left[\pi E_\infty(\phi_B - qV + \eta_F)\right]^{1/2}}{\cosh\left(\frac{E_\infty}{kT}\right)} \left[\tanh\left(\frac{E_\infty}{kT}\right)\right]^{1/2}$$

$$\exp\left(\frac{\eta_F}{kT} - \frac{\phi_B + \eta_F}{E_o}\right) \qquad (2.59)$$

This equation differs from Eq. (2.55) in the extra $\left[1-\exp\left(-\frac{qV}{kT}\right)\right]$ term in Eq. (2.58). Also, Eq. (2.59) has an extra $\left[\tanh\left(\frac{E_\infty}{kT}\right)\right]^{1/2}$ term. Otherwise the equations are the same.

However, the recent presentation by Padovani (14) of Padovani and Stratton's (11) results show that whereas Eq. (2.46) is applicable only for V greater than a few kT/q it can be made to apply at all forward biases with the inclusion of a $\left[1-\exp\left(-\frac{qV}{kT}\right)\right]$ term. Also given in Padovani (14) is a new equation for f_m, Eq. (2.51), which becomes:

$$f_m = \left[4E_\infty E_m\left(1 - \frac{E_m}{\phi_B}\right)\right]^{-1} . \qquad (2.60)$$

The new term, $\left(1 - \frac{E_m}{\phi_B}\right)$, is reported to be a "correction" term to the original Eq. (2.51).

If the new f_m coefficient, Eq. (2.60), and the original values of b_m, c_m, and E_m, Eqs. (2.49), (2.50), and (2.52), are used in Eq. (2.46), and if Eq. (2.46) is multiplied by the $\left[(1 - \frac{qV}{kT})\right]$ term, the

result is the same as Eq. (2.59). That is, the results of the I-V response in the TFE case as derived by Crowell and Rideout will match those of Padovani and Stratton if the above mentioned corrections are carried through. The same assumption used in the FE case, that $\phi_B \gg V + n_F$, is used here.

It should be noted, however, that even though Padovani (14) outlines the above correction to Padovani and Stratton, he still uses Padovani and Stratton's original equation (Eqs. (2.55), (2.56), and (2.57)) in describing the TFE response. Obviously, the more correct form is that of Eqs. (2.58) and (2.59) and these equations will be used in this research.

The equations for the TFE I-V response also have a range of T, ϕ_B, and N_D over which they are adequate approximations. This range is given by Eq. (2.53) and Eq. (2.54). Using Eq. (2.38) for c_1, and Eq. (2.53):

$$kT > 2E_\infty \left\{ \ln \left[\frac{4(\phi_B - qV)}{n_F} \right] \right\}^{-1} \tag{2.61}$$

must be satisfied in order to have TFE conduction occuring.

The other limitation to TFE is Eq. (2.54). Padovani shows that this limit results in :

$$\frac{\cosh^2 \left(\frac{E_\infty}{kT} \right)}{\sinh^3 \left(\frac{E_\infty}{kT} \right)} < \frac{2(\phi_B + n_F - V}{3E_\infty} \ . \tag{2.62}$$

If Eq. (2.62) is not satisfied, the contact I-V properties are governed by thermionic emission (TE) rather than thermionic field emission. In the TE range the I-V response is that of a MS diode with rectifying properties. This type of contact does not exhibit ohmic properties, and therefore operation in the TE range will not be considered in this research. For the most part, with the values of ϕ_B, N_D and T used in this research, Eq. (2.62) is always satisfied.

Some additional clarification must be made concerning the conditions expressed in Eq. (2.25) and Eq. (2.53). If Eq. (2.25) is rewritten slightly it becomes:

$$c_1 kT < 1 - kT(2f_1)^{1/2} \ . \tag{2.63}$$

Therefore, if $c_1 kT > 1 - kT(2f_1)^{1/2}$, the contact is not operating strictly in the FE range. For certain values of T, f_1, and c_1,

$$1 - kT(2f_1)^{1/2} < c_1 kT < 1 \tag{2.64}$$

is satisfied. The left hand inequality means that the contact is not in the FE range but at the same time the right hand inequality means that the contact is not yet strictly into the TFE range.

The problem here is not that neither FE or TFE conduction is occuring, but that in this transition range the Taylor expansion used in determining P(E) is not strictly accurate. The actual type of emission consists of both FE and TFE occuring simultaneously. In such a case the strict use of either FE or TFE equation for the I-V response will lead to slight errors.

For conditions that depart only slightly from Eq. (2.25) the equation for the FE I-V response can be used as an approximation. Otherwise, the TFE I-V response can be used and will result in slight errors until the conditions are such that Eq. (2.53) becomes satisfied.

The determination of an expression for R_c in the TFE range, as given in Yu (15), is again based on the use of Eq. (2.4). Using this with the I-V response given by Eq. (2.58) and ignoring the minor voltage dependence in the J_s term of Eq. (2.59), the value of R_c for the TFE range is given by:

$$R_c = \frac{kT}{qA} \frac{kT}{[\pi E_\infty(\phi_B + n_F)]^{1/2}} \left[\coth\left(\frac{E_\infty}{kT}\right) \right] \cosh\left(\frac{E_\infty}{kT}\right) \exp\left(\frac{\phi_B - n_F}{E_o} - \frac{n_F}{kT}\right),$$

$$\tag{2.65}$$

with E_o being given by Eq. (2.56). This equation is applicable if Eq. (2.61) is satisfied and can be used to give a fairly close approximation until the condition given by Eq. (2.25) is approached. A transition to Eq. (2.42) can then be made.

2.7 Theoretical calculation of R_c based on FE and TFE equations

Using Eq. (2.42) and Eq. (2.65) with $T = 23°C$ and ϕ_B as a parameter, Figure 2.5 results. The range of N_D is from $10^{18}/cm^3$ to $10^{20}/cm^3$. The range in ϕ_B of 0.7 eV to 1.1 eV covers the values usually reported in the literature for Au contacts on GaAs. The most often reported value of ϕ_B is $\approx$ 0.9 eV. The curves in the upper left portion of the figure are for the TFE range of operation and those in the lower right are for the FE range. The dotted line in the center represents
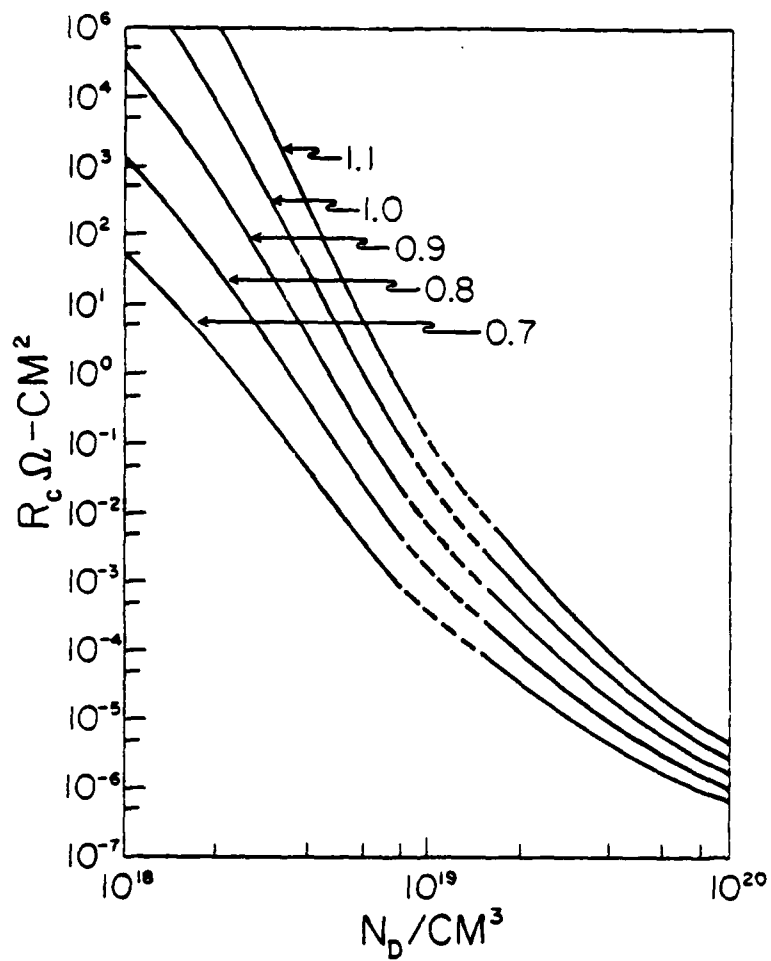
Figure 2.5 Variation of contact resistivity with doping
level and barrier height at $T = 23^{\circ}C$.

28

the transition region where the TFE and FE equations for R_c are not strictly valid. The dotted line is merely a smooth fit curve joining the solid lines together.

It is evident from this figure that for $\phi_B = 0.9$ eV, an N_D on the order of $10^{19}/cm^3$ can initiate FE type tunneling but in order for R_c to become very small, on the order of $10^{-6}\Omega$-cm^2 , a value of N_D near $10^{20}/cm^3$ is necessary. Also evident from the figure is that the value of R_c is extremely sensitive to N_D. In the near $10^{19}/cm^3$ range, a factor of two change in N_D gives rise to nearly an order of magnitude change in R_c.

Based on the same equations, Figure 2.6 gives the temperature variation of R_c in the FE range with $\phi_B = 0.9$ eV and N_D as a parameter. For R_c to remain in the FE range at room temperature, with $\phi B = 0.9$ eV, NG needs to be above $\approx 2 \times 10^{19}/cm^3$. Figure 2.7 gives the temperature response or R_c in the FE range for $N_D = 6 \times 10^{19}/cm^3$ with ϕ_B as a parameter. It is evident from both the figures that, as the contact properties are pushed more into the FE range by larger N_D of lower ϕ_B, the value of R_c becomes more independent of temperature. This is the expected characteristic of a contact where carrier transport is by tunneling instead of by a thermally assisted emission process.

Figure 2.8 gives the temperature response of R_c in the TFE range of $\phi_B = 0.9$ eV and N_D as a parameter. It should be noted that toward the upper end of N_D, ($N_D \approx 8 \times 10^{18}/cm^3$) the TFE equation for R_c is not strictly valid and the R_c values shown in this region are the approximation made by using the TFE equation. Figure 2.9 gives the temperature response for R_c in the TFE range for $N_D = 6 \times 10^{\infty}/cm^3$, the upper end of the TFE region, with ϕ_B as a parameter. In both cases it is seen that since TFE is a thermally assisted tunneling process, there exists a larger temperature variation in R_c .

The theoretical equations for R_c under TFE and FE, and their resulting plots of R_c vs. N_D and R_c vs. T , are the predictions with which the experimental data in this research will be compared. If good correlation between theoretical prediction and experimental data is observed, then the Schottky model would appear to be adequate for describing contact properties and could therefore be used with more confidence in future contact studies.
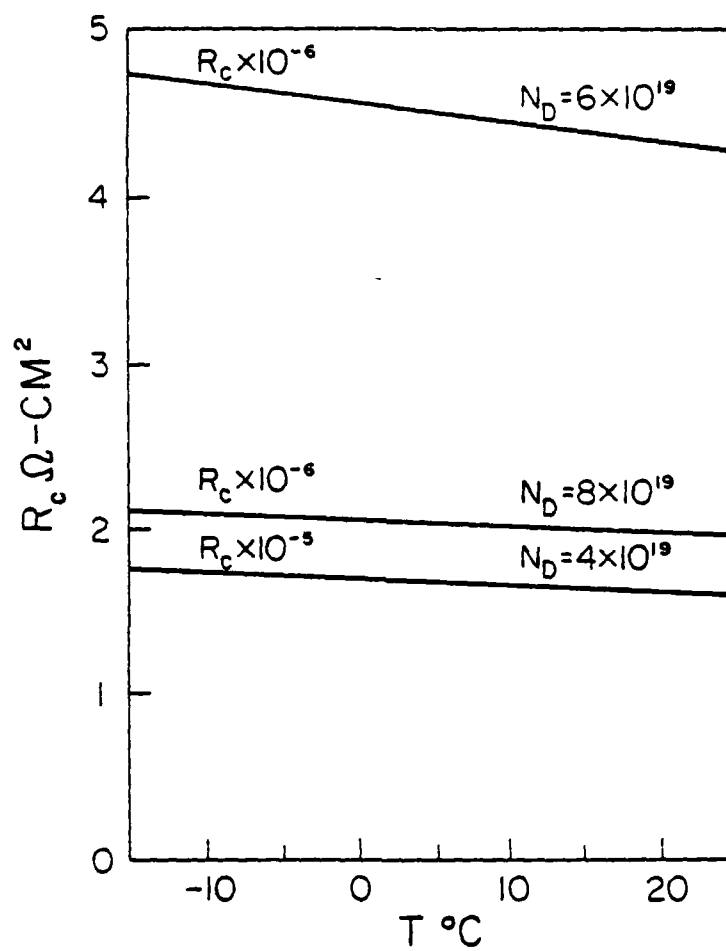
Figure 2.6 Variation of contact resistivity with temperature
and doping level. FE range with $\emptyset_B$ = 0.9 eV.
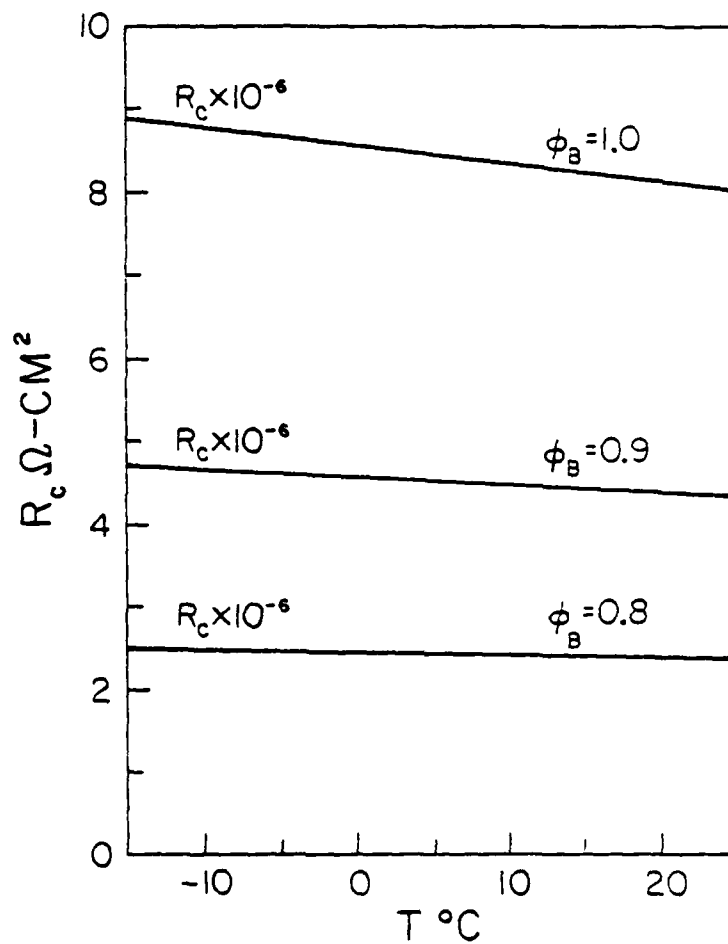
Figure 2.7 Variation of contact resistivity with temperature
and barrier height. FE range with $N_D = 6 \times 10^{19}/cm^3$.

31
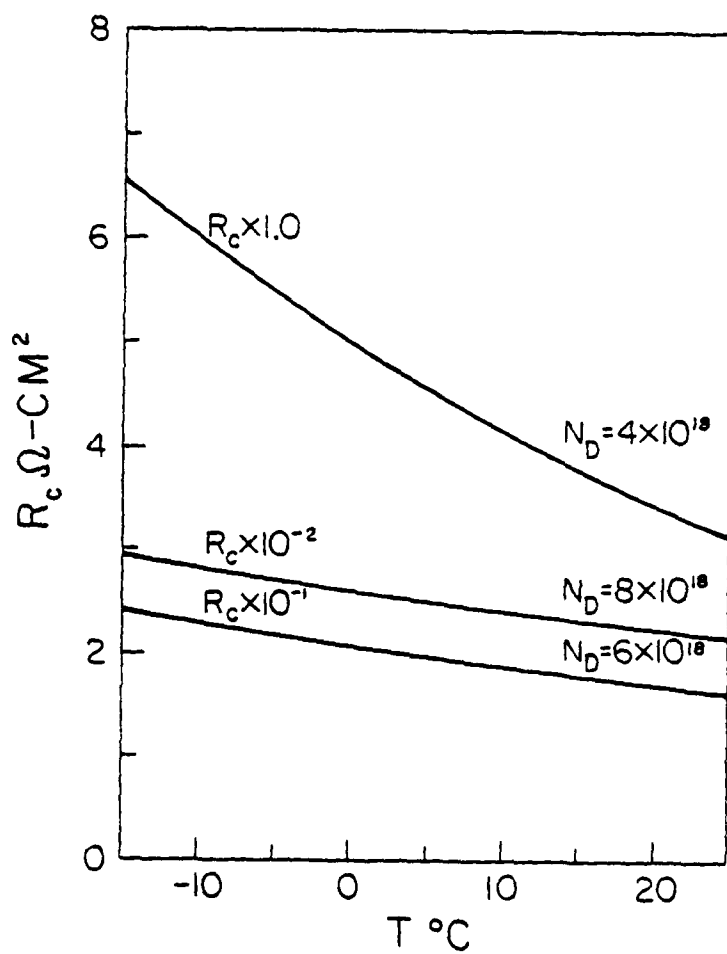
Figure 2.8 Variation of contact resistivity with temperature
and doping level. TFE range with $\emptyset_B$ = 0.9 eV.

32
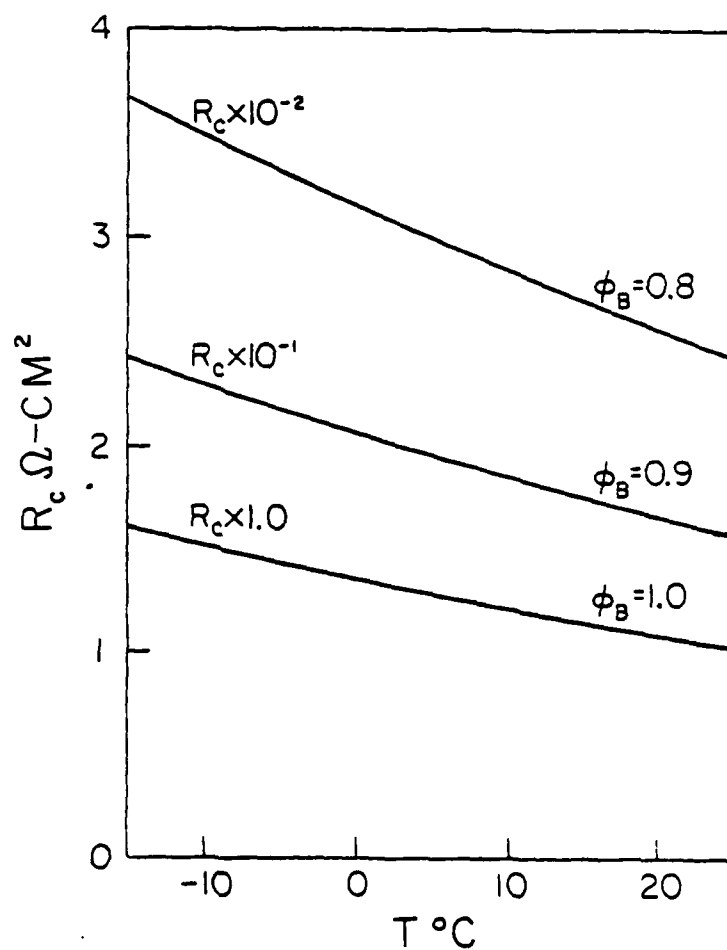
Figure 2.9 Variation of contact resistivity with temperature
and barrier height. TFE range with $N_D = 6 \times 10^{18}/cm^3$.

BLANK PAGE

SECTION III

EXPERIMENTAL METHOD

3.1 Fabrication and characterization of Sn doped surface layers

The contacts investigated in this research were fabricated on n-type layers diffused into the surface of a p-type GaAs wafer. Diffused layers were chosen over bulk n-type GaAs material because it was necessary to be able to vary the concentration of dopant in the GaAs to determine how this variation affected the value of contact resistance. For tunneling contacts, the n-type layer surface dopant concentration, C_s, is the parameter used in place of N_D in the theoretical equations. A p-type substrate was used because the junction formed between the n-type region and substrate would provide isolation for the actual current carrying layer and would allow for a straightforward determination of C_s.

The fabrication of the diffused layers utilized a Sn bearing oxide layer spun on the p-type substrate surface. The formation of n-type diffused layers in GaAs using Sn in an oxide layer source has been demonstrated by other workers. To overcome this problem, diffusions are usually performed by enclosing the GaAs wafer in an evacuated and sealed or a partially sealed quartz box or ampoule containing some elemental As or extra pieces of GaAs. In such a closed environment the As escaping from the additional pieces of As and GaAs creates an overpressure of As which prevents the escape of As from the wafer surface.

In this research, open tube diffusions were tried initially and the problems of As loss and undesirable surface disruption were observed. It was therefore decided that a closed chamber type of environment was necessary. An evacuated and sealed ampoule structure was not used because of the relatively difficult fabrication. Instead a "semi-closed chamber" (SCC) type of vessel was used.

Figure 3.1 shows a picture of the SCC, made from a quartz inner-outer joint, the ends of which were closed as in a test tube. For the diffusion, the dopant coated GaAs wafers were placed inside the SCC along with some pieces of elemental As and extra pieces of GaAs. The two halves of the SCC were pushed together and the SCC was placed into an open quartz boat which allowed for easy insertion and removal
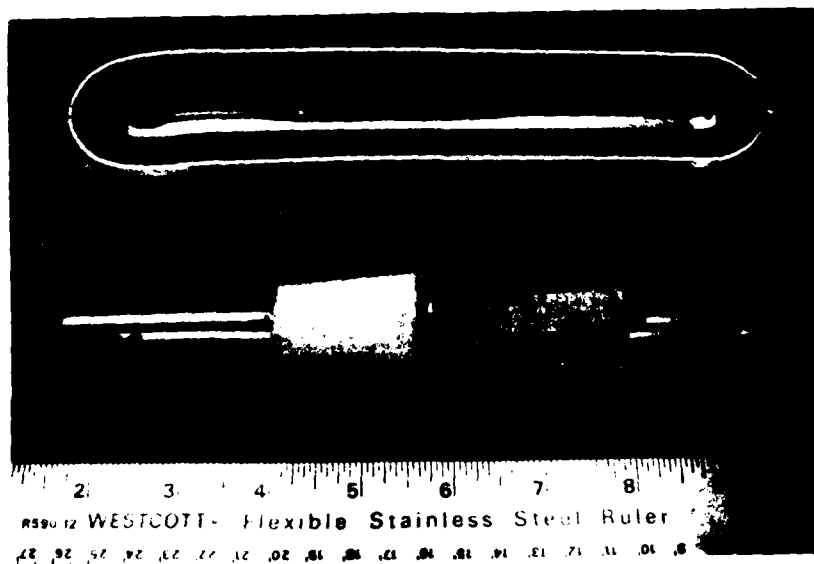
Figure 3.1   Photograph of the semi-closed chamber used in
the diffusions.

from the diffusion furnace. During the diffusion an Ar flow was main-
tained through the furnace.

During the initial period of the diffusion, the As in the SCC
vaporized and the increased pressure forced the SCC apart. This As
vapor escaped from the furnace tube and was exhausted through a
"scavenger box" at the furnace mouth. After this occured, the SCC was
obviously not totally enclosed but, with only a slight separation
between the halves of the SCC, the internal atmosphere was As saturated
and stagnant and this was enough to improve the surface quality very
much over the open tube diffusion case. In a few cases some slight
pitting was still seen but the surfaces generally remained specular in
appearance.

After the diffusion, pieces of the wafers were scribed out for
lapping and staining. The test pieces were hand lapped on a jig with
an angle of ~ 2°. The junction was then stained with a commercial
staining solution (48) which delineated the n-type surface layer from
the p-type bulk. The depth of the n layer (the junction depth), x_j,
was measured by examining the lapped and stained sample under a
microscope that was equipped with a Watson interferometer. The value
of x_j was calculated from:

$$x_j = n\left(\frac{\lambda}{2}\right) \qquad (3.1)$$

where λ is the wavelength of the illumination (in this case
$\lambda = 0.546~\mu$), and n was the number of whole fringe shifts from the
original surface, over the lapped edge, to the delineated junction.
With a little practice, shifts of half a fringe were easily apparent
with shifts of 1/4 of a fringe being harder to estimate. An accuracy
of ± 1/2 a fringe translates to ~ ± 0.14 μ accuracy in the measurement
of $\bar{x}_j$. The diffusion process parameters of time and diffusion
temperature were chosen to attempt to realize x_j values of ~ 1μ and
therefore the accuracy to which x_j could be determined with the above
measurement is on the order of 15%.

The remaining main portion of the diffused wafer, on which the
actual contact structures were made, was then tested to determine
values for sheet resistivity, R_s, average resistivity, $\bar{\rho}$, average Hall
mobility, μ_H, and average carrier concentration N_D. The measurement
was made by the van der Pauw (49) technique. Contact to the n-type
layer was made with small dots of In-Ga eutectic on the wafer surface
along the periphery of the wafer. The relative ohmicity of these
contacts was checked by examining the I-V curve of the diffused layer
between all contacts on a transistor curve tracer. A straight line
represented adequate contact ohmicity. (Actually, due to the
potentiometric nature of the measurement used in the van der Pauw
technique, relatively small contact non-ohmicity is unimportant.)

37

The resistance values obtained from the van der Pauw measurements were used to determine a value of $\bar{\rho}$ for the layer. The determination of $\bar{\rho}$ involved the use of the value of x_j determined earlier. Van der Pauw type Hall effect measurements were made to verify that the layer was n-type, and to determine values of $\bar{\mu}_H$ and N_D. The average mobility and electron concentration values are not directly useful in determining C_S but do give an order of magnitude check on similar values observed by other researchers for GaAs. It should also be noted that N_D gives the average ionized electron density and not the average donor dopant density, unless full ionization can be assumed.

The measurement of $\bar{\rho}$ is very important because $\bar{\rho}$ data is used to determine the value of dopant surface concentration C_S, and C_S is the most sensitive parameter controlling R_c. This is readily seen from Figure 2.5. Therefore, equally important is the way in which C_S is determined from $\bar{\rho}$ data. The method used in this research was to relate $\bar{\rho}$ to C_S through an "Irvin" curve (50).

An "Irvin" curve is a plot of C_S vs. $\bar{\rho}$ and is developed by considering how $\bar{\rho}$ is related to C_S, C_B and the shape of the diffused dopant profile. Because of the importance of the C_S term in accurately comparing theoretical predictions of R_c to experimental data, the rest of this section details the development of an "Irvin" ($\bar{\rho}$-C_S) curve for Sn diffusions in GaAs wherein several important facts unique to this research, are considered.

The development of the $\bar{\rho}$-C_S "Irvin" curve initially involves considering that for an n-type sample the resistivity is given by:

$$\frac{1}{\bar{\rho}} = q\mu_n n \tag{3.2}$$

where $\bar{\rho}$ = resistivity

   q = electronic charge

   μ_n = electron mobility

   n = electron concentration

In a diffused layer n is a function of distance into the wafer and therefore ρ is also a function of distance. The effect of the profile is to create an n-type layer which has an average ρ value, indicated by $\bar{\rho}$, and given by:

$$\frac{1}{\bar{\rho}} = \frac{q}{x_j} \int_0^{x_j} \mu_n (N)N(x)dx \tag{3.3}$$

38

Eq. (3.3) represents the effect of all individual $\rho(x)$ values taken in parallel and averaged over the entire surface layer from $x = 0$ to $x = x_j$.

The integral for $\bar{\rho}$ is not easily calculated because the mobility, μ_n, is a function of doping and is therefore also a function of x. The usual way to calculate Eq. (3.3) is to use a computer and approximate the integral with a numerical integration. However, the integral can first be simplified by removing the dependence on x_j.

The electron concentration, $N(x)$, is determined from the dopant distribution.

$$C(x) \quad = \quad C_s \, \text{erfc} \, \frac{x}{2\sqrt{Dt}} \tag{3.4}$$

where D = diffusion coefficient for Sn in GaAs
            at the diffusion temperature used

      t = time of the diffusion

Eq. (3.4) is the standard profile expected for a diffusion from an unlimited source as was the case for this research. A simple derivation of Eq. (3.4) can be found in Grove (51).

If a substitution of

$$y \quad = \quad \frac{x}{2\sqrt{Dt}} \tag{3.5}$$

is made then

$$dx \quad = \quad 2\sqrt{Dt} \, dy \tag{3.6}$$

$$y_j \quad = \quad \frac{x_j}{2\sqrt{Dt}} \tag{3.7}$$

and Eq. (3.3) becomes

$$\frac{1}{\bar{\rho}} \quad = \quad \frac{q}{y_j(2\sqrt{Dt})} \int_0^{y_j} \mu_n(N)N(y) \, 2\sqrt{Dt} \, dy \tag{3.8}$$

or simplified:

$$\frac{1}{\bar{\rho}} = \frac{q}{y_j} \int_o^{y_j} \mu_n(N)N(y) \, dy \qquad (3.9)$$

where y_j is given by the condition that at the junction the free electron concentration equals the background concentration of holes in the bulk p-type substrate. That is:

$$N(y_j) = C_B \qquad (3.10)$$

The simplification in Eq. (3.9) over Eq. (3.3) is that for the calculation, specific information on D or t is no longer needed since the averaging process removes the dependence on these variables. For any particular fabrication run in which D or t may vary, Eq. (3.10) must still be satisfied and therefore the given values of C_B and C_S alone determine $\bar{\rho}$. Most importantly, the curve developed from Eq. (3.9) is valid for any particular combination of D or t, as long as the assumptions concerning the shape of the profile are the same and Eq. (3.10) is satisfied.

In the development of the $\bar{\rho}$-C_S curve from Eq. (3.9) the value of $\mu_n(N)$ does not have to be given with respect to x or y because in the computer calculation, at each y increment points, $N(y)$ is calculated first and then $\mu_n(N)$ is determined. Therefore, a μ_n vs. N variation is sufficient. The relationship for μ_n and N used in this calculation was obtained by fitting an equation for μ_n in terms of N to the experimental data for μ_n vs. N given in Sze (9).

(Some important facts should be noted concerning the μ_n vs. N graph for electrons in GaAs as given in Sze. The graph is labeled as μ_n vs. "impurity concentration" instead of "electron or carrier concentration". However, in the original article of Sze and Irvin (5), from which the graph was taken, the statement is made that the plot is actually of μ_n vs. carrier (electron) concentration for various bulk n-type GaAs samples. The authors used the assumption that in GaAs at room temperature all donor impurities were ionized and therefore carrier concentration was equivalent to impurity concentration.)

From this point, further development of the $\bar{\rho}$-C_S curve depends on the formulation of the $N(x)$ term in Eq. (3.9). It is therefore necessary to consider the relationship between the Sn dopant concentration profile, $C(x)$, and active electron concentration profile, $N(x)$. Specifically , an assumption must be made as to the degree of dopant ionization. Tuck and Badawi (44) confirmed that the Sn concentration in GaAs can be accurately characterized by an erfc profile as given in Eq. (3.4). However, they also made some measurements which implied that not all Sn donors were ionized, meaning that $N(x)$ was not the same as $C(x)$, as it would be for full ionization.

The problem of determining whether or not all Sn donors are ionized can be analyzed by considering the physics of electron conduction. For this research, diffusions with rather large dopant concentrations, in the 10^{18} to 10^{20} per cm^3 range, were attempted. In this range one would expect that the dopant is not fully ionized. Therefore, a calculation must be made to theoretically determine the Fermi level and degree of ionization. This straightforward calculation is based on the charge balance equation (53):

$$n = N_D^+ - p - N_A^- \qquad (3.11)$$

where for an n-type layer, $p \approx 0$ and $N_A^- = C_B$. One crucial assumption used at this point is that even at these very high levels of dopping the Sn donors can be assumed to lie at a discrete energy level, $E_D \approx 5$ meV below E_c (54). The number of free electrons, n, can then be calculated using the expression:

$$n = N_c \left(\frac{2}{\sqrt{\pi}}\right) \int_0^\infty \frac{1}{1 + \exp\left(\epsilon - \frac{n_F}{kT}\right)} \sqrt{\epsilon} \, d\epsilon \qquad (3.12)$$

where

$$N_c = 2 \left(\frac{2\pi m^* kT}{h^2}\right)^{3/2} \qquad (3.13)$$

is the effective density of states in the conduction band

$$\epsilon = \frac{E}{kT} = \text{energy referenced to } E_c = 0$$

$$n_F = \text{Fermi level referenced to } E_c = 0$$

The above equation assumes a parabolic density of states vs. energy distribution for electrons in the conduction band.

The ionized donor density is given by:

$$N_D^+ = N_D \frac{1}{1 + 2\exp\left(\frac{n_F}{kT}\right)} \qquad (3.14)$$

where N_D = concentration of donor atoms .

With the above, Eq. (3.11) becomes:

41

$$N_C \left(\frac{2}{\sqrt{\pi}} \right) \cdot \int_0^\infty \frac{1}{1 + \exp \left(\epsilon - \frac{n_F}{kT} \right)} \sqrt{\epsilon} \, d\epsilon \quad =$$

$$\frac{N_D}{1 + 2 \exp \left(\frac{n_F - E_D}{kT} \right)} - C_B$$

(3.15)

Eq. (3.15) is solved to yield a value of Fermi level, n_F, and subsequently gives the value of electron concentration, n, for the chosen conditions of N_D, C_B, E_D, and T within the given assumptions.

When the $\bar{\rho}$-C_s ("Irvin") curve was being initially calculated to use in this research it was believed that, as opposed to a calculation performed by Galiga (55) in which the full ionization assumption of $N(x) = C(x)$ was made, partial ionization as included in Eq. (3.15) needed to be considered. Therefore, a computer numerical integration of Eq. (3.9) was performed and involved the following steps:

1. For a given C_s and T the dopant concentration N_D in Eq. (3.15) was given by

   $$N_D(y) = C(y) = C_s \, \text{erfc} \, y$$

2. At each integration point, y_i, Eq. (3.15) was used to determine n_F and subsequently $N(y_i)$. The value of the Fermi-Dirac integral for a particular value of n_F was evaluated using the series approximation of Battocletti (56).

3. Using the μ_n vs. N graph in Sze (9), from which a fitted equation of

   $$\mu_n = -1500 \, [N(y)] + 30,000 \, \frac{cm^2}{V\text{-}sec} \qquad (3.16)$$

   was obtained, a value of $\mu_n(y_i)$ was calculated.

4. The product of $\mu_n(y_i) \cdot N(y_i)$ gave the integrand value at y_i.

5. The integral was calculated using a Simpson's approximation (70) involving the summation of all the $\mu_n(y_i) \cdot N(y_i)$ products up to a point where $N(y_i) = C_B$, namely the junction at $y = y_i$.

6. $\bar{\rho}$ was then calculated using Eq. (3.9).

42

This sequence of calculations was performed for a range of C_S and C_B values and the graph of Figure 3.2 resulted. This graph and the preceding calculations were used to attempt to determine C_S for some of the experimental wafers but severe problems became apparent. As can be seen from the experimental data section in this report, experimental values of $\bar{\rho}$ in the low 10^{-3} range were measured. If the calculations given in Figure 3.2 were correct, C_S values very much greater than 10^{19} are indicated. The curve of C_S vs. $\bar{\rho}$ is increasing so rapidly in the low $\bar{\rho}$ region that values of $10^{20}/cm^3$ or $10^{21}/cm^3$ would be likely.

Given that the manufacturers specification for the dopant concentration of the undiluted spin on solution was only $10^{20}/cm^3$, the accuracy of above results and Figure 3.2 is highly doubtful. Also, if C_S values of $10^{20}/cm^3$ or more were present, the GaAs would be extremely highly doped and drastic changes in band structure could be expected, leading to inaccuracies in the assumptions used to derive the equations for C_S vs. $\bar{\rho}$.

For these reasons it was concluded that Figure 3.2 was not correct. The main discrepaancies lay with the assumption of partial ionization of the Sn dopant at a discrete level of E_D.

An explanation of electronic conduction in heavily doped semi-conductors, as given in various sources such as Fistul (57), Madelung (58), or Blakemore (59), point to the formation of an impurity band with associated impurity band conduction, especially for GaAs at the dopant levels used in this research. The extremely small value of E_D for Sn could quickly lead to band tailing such that a continuous extension of E_c down through E_D and into the band gap is possible.

As Sze (9) details, there have been some attempts at quantitatively determining the changes in the band structure resulting from high doping. These calculations are extremely difficult in themselves and incorporating such calculations into the calculation of $\bar{\rho}$ and then C_S would clearly be intractable. However, as Madelung (58) states, when such band tailing is present, the effect is to reduce E_D to zero and a reasonably accurate assumption is to consider that all the donor states are ionized.

With this in mind, the calculation of C_S vs. $\bar{\rho}$ was changed to incorporate the assumption of full ionization of all Sn donors. This results in the use of $N(y) = C(y) = C_S \, erfc(y)$ in Eq. (3.9). The value of μ_n was still given by Eq. (3.16). The use of the Sze graph for μ_n vs. N seemed valid since it is an experimental dataplot of actual mobilities. Regardless of the mechanism responsible for determining the actual ionization level of donors and their subsequent mobilities, in impurity bands or otherwise, Sze's graph gives the actual value of μ_n measured for a measured value of carrier concentration N. Therefore, the limiting assumption in calculating the C_S vs. $\bar{\rho}$ plot was not the use of Sze's graph in light of band tailing and the resulting

43
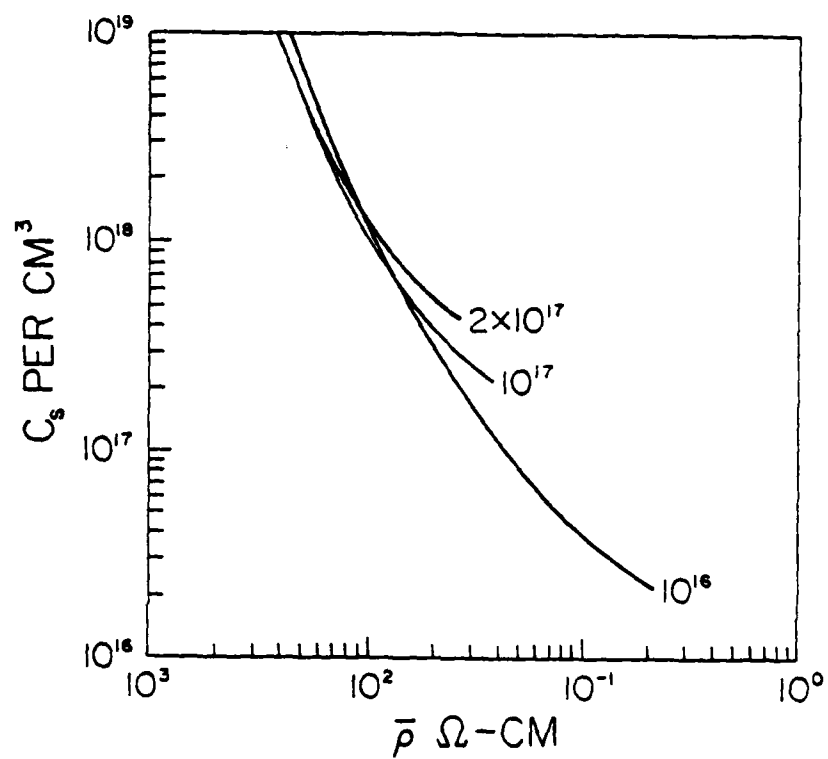
Figure 3.2 Variation of $\bar{\rho}$ and C_S for an erfc profile, n-type
diffusion in GaAs. P-type substrate, background
concentration, C_B. Partial ionization of Sn
donor atoms.

change in conduction specifics, but rather the assumption that doping a sample with C(y) Sn atoms resulted in N(y) = C(y) free electrons.

When the full ionization assumption was used and the same integral calculation procedure was performed on Eq. (3.9), Figure 3.3 resulted. Since this assumption and general calculation procedure was the same as used by Baliga (55) the results should be the same. A comparison of his C_s vs. $\bar{\rho}$ graphs and Figure 3.3 shows that the values are nearly identical.

As to the validity of the assumption of full ionization, experimental data given later on will show that the value of C_s determined from a measurement of $\bar{\rho}$ and the use of Figure 3.3, agrees well with the values of C_s determined from I-V measurements on the test samples. The agreement of these two C_s values indicates that the assumption of full ionization is valid. This point will be discussed again in later sections.

3.2 Fabrication of contact structures

The contact structure used in this research is shown in Figure 3.4. The squares at both ends are the contacts to be tested. The interior strips are voltage pick-off strips which allow the measurement of the IR drop along the n-type layer. This structure allowed the determination of Rc by the transfer length method as will be detailed in the next section.

The fabrication of the contact structures utilized a photolithographic lift-off technique. After the n-type layers had been diffused and the dopant film removed, a layer of photoresist was spun on the surface. The photomask used to expose the photoresist consisted of a photographic emulsion plate negative having five identical contact structures. This allowed the fabrication of five test structures at one time on the same diffused layer. After exposure and development of the photoresist the resulting pattern consisted of holes in the photoresist layer, exposing the GaAs surface where contacts were to be made.

The next step was to evaporate a layer of Au onto the photoresist covered wafer. An Au-GaAs MS contact was formed in those areas where there were holes in the photoresist layer.

To remove the unwanted Au and to form the final contact pattern of Figure 3.4, the wafer having the photoresist coating and Au film was placed in a beaker filled with acetone. The acetone dissolved the photoresist and lifted off the Au not in contact with the GaAs, leaving behind the desired contact structure pattern.

After the contact structures were formed, each separate structure was scribed apart to make an individual test element. Each
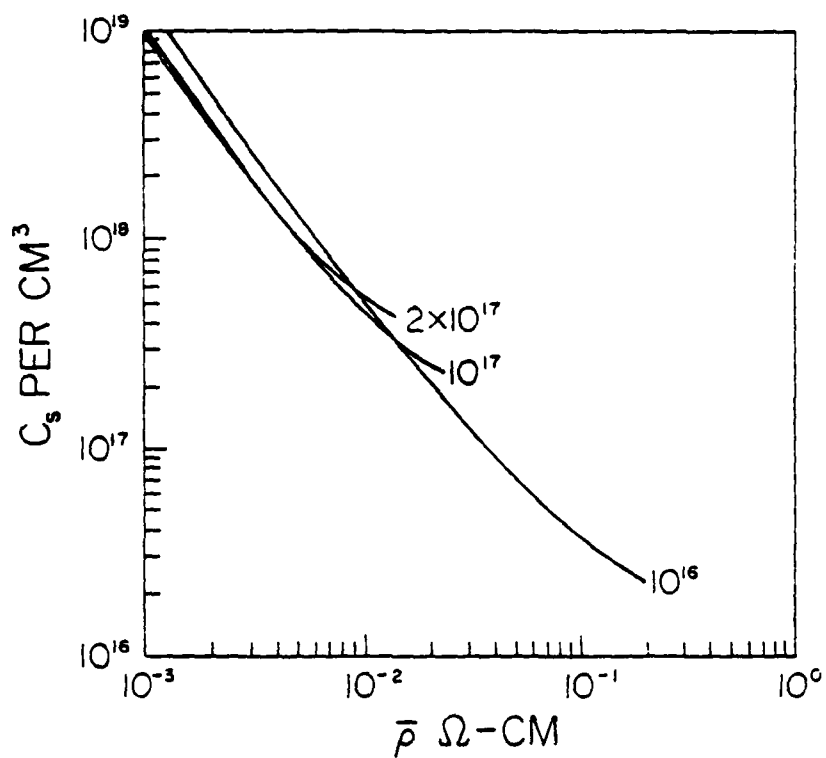
Figure 3.3 Variation of $\bar{\rho}$ and C_S for an erfc profile, n-type diffusion in GaAs. P-type substrate, background concentration, C_B. Full ionization of Sn donor atoms.

TOP VIEW

SIDE VIEW
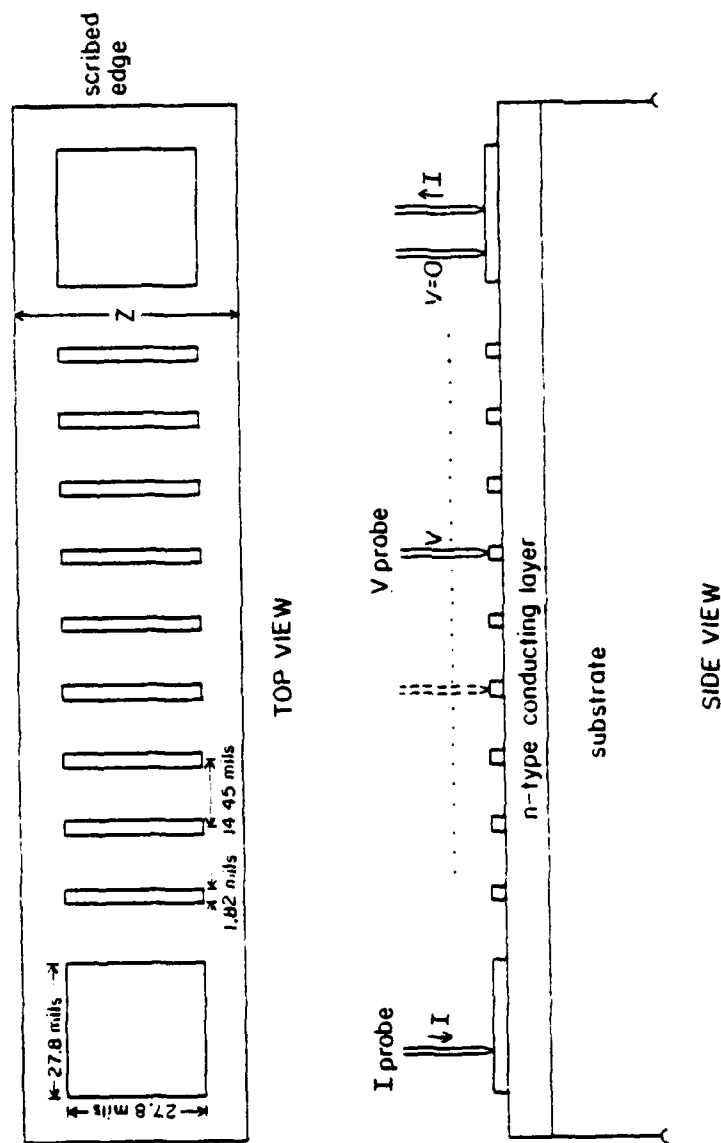
Figure 3.4   Diagram of the contact structure

47

of these structures was composed of the Au pattern on top of an n-type diffused layer, separated by p-n junction isolation from the p-type substrate beneath. The scribed structure was chosen over a mesa-etched type of separation because of the ease with which pieces of GaAs can be scribed apart and the relatively smooth cleave edge which results. Etching apart the individual structures would have also have involved another masking step. Overall, etching would have resulted in more complicated processing without any overriding advantage.

The formation of individual n-type test islands in the p-type substrate was also attempted but the process was not used because of difficulties associated with the initial oxide layer needed to mask the Sn diffusion into the non-island areas of the substrate.

3.3 Transfer length measurement

The transfer length measurement (60), also known as the Schottky method, is actually an extension of the general transmission line method (TLM) (61) of measuring R_c. In the transfer length method, the actual measured quantity is the transfer length, L_T , which gives R_c through the expression

$$R_c = R_s L_T^2 \qquad (3.17)$$

The derivation of Eq. (3.17) and an understanding of the physical meaning of transfer length can be based on the model of an MS contact with planar current flow as shown in Figure 3.5(a). Figure 3.5(b) shows the variation of the voltage in the conducting layer versus distance from the contact in Figure 3.5(a). The conducting layer (in this case n-type) is characterized by a sheet resistance, R_s. The non-ideally conducting properties of the interface are lumped into the term R_c which, in the model, represents a distributed resistance of the contact. Theoretically R_c is given by Eq. (2.9).

In Figure 3.5(a), for purposes of this initial calculation, the contact length is assumed to be infinite. Practically, this assumption is valid as long as the L_T value is much less than the contact length. The contact edge defines the $x = 0$ point with $x < 0$ representing the non-contacted diffused n-type layer. The contact metal is assumed to be perfectly conducting and therefore at a uniform potential, in this case ground.

Current is flowing into the layer under the contact from the left. For $x < 0$ the voltage drop, $V(x)$, with respect to x is dependent only on the IR drop along the R_s of the layer. Or:

$$I = - \frac{Z_s}{R_s} \frac{dV(x)}{dx} \qquad (3.18)$$
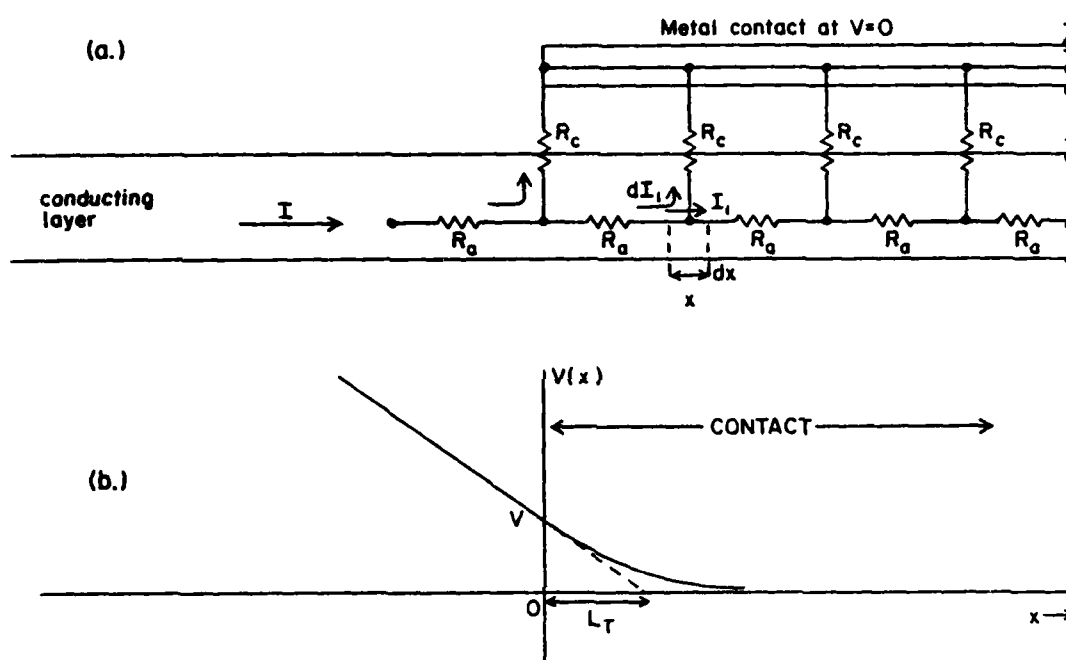
Figure 3.5 Model of a MS contact used to determine
transfer length. (a) Lumped element
model. (b) Voltage distribution.

where Z_s is the width of the contact structure through which the current flows.

For $x < 0$, a plot of $V(x)$ vs. x yields a straight line of slope $= -IR_s/Z_s$. Such an experimental plot of $V(x)$, as measured from the voltage pick off strips, versus the separation of the strips, is called the transfer length plot and the value of R_s can be calculated from the slope since I and Z_s are known.

Eq. (3.18) is valid up to the contact edge at $x = 0$. At some point $x_1 > 0$, some current is lost to the contact through R_c. In the interval dx around x_1 this amount of current is:

$$dI_1 \quad = \quad - \frac{Z}{R_c} d_x V(x) \bigg|_{x = x_1} \tag{3.19}$$

and the current remaining in the conducting layer at $x = x_1$ is

$$I_1 \quad = \quad I(x = x_1) \quad = \quad - \frac{Z}{R_s} \frac{dV(x)}{dx} \bigg|_{x = x_1} \tag{3.20}$$

Taking the derivative of Eq. (3.20)

$$\frac{dI}{dx} \bigg| \quad = \quad - \frac{Z}{R_s} \frac{d^2 V(x)}{dx^2} \bigg|_{x = x_1} \tag{3.21}$$

or rewritten:

$$dI \bigg|_{x = x_1} \quad = \quad - \frac{Z}{R_s} \frac{d^2 V(x)}{dx^2} dx \bigg|_{x = x_1} \tag{3.22}$$

which must be equal to Eq. (3.19). Therefore:

$$- \frac{Z}{R_s} \frac{d^2 V(x)}{dx^2} dx \quad = \quad \frac{Z}{R_c} d_x V(x) \tag{3.23}$$

or

$$\frac{1}{R_s} \frac{d^2 V(x)}{dx^2} - \frac{1}{R_c} V(x) \quad = \quad 0 \tag{3.24}$$

which has the solution:

$$V(x) = V(0) \exp\left(-\frac{x}{L_T}\right) \tag{3.25}$$

where $L_T = [R_c/R_s]^{1/2}$ which is Eq. (3.17).

The slope of Eq. (3.25) at $x = 0$ is:

$$\left.\frac{dV(x)}{dx}\right|_{x=0} = -\frac{V(0)}{L_T} \tag{3.26}$$

and must be the same as dV/dx for $x < 0$.

Therefore, if a plot of $V(x)$ vs. x is made and the line for $x < 0$ is extended with the same slope past $x = 0$, the intersection of this extended line with the $V(x) = 0$ axis will occur at $x = L_T$. A typical transfer length plot showing the value of L_T is given in Figure 3.6. In this figure the right hand contact is ground and $V(x)$ is measured with respect to this point. The voltage at each pick off strip is assumed to be the voltage at a point along the surface which is the center of the strip. This does not give rise to large errors since the width of the strip is small compared to their separation.

A value of L_T for the left hand contact, where the current enters, can also be found. In this case L_T is the difference between the contact edge and the point on the extended line where $V(x)$ is equal to the applied voltage, V_{APP}. Any asymmetry in contact fabrication due to processing will show up as different values of L_T.

In the above derivation any voltage drop in the vertical direction due to vertical current flow in the conducting layer has been implicitly neglected. Schuldt (36) analyzed the exact case and showed that for thin layers, as in the case here, the above approximation leads to very little error.

An interesting point should be noted concerning the actual resistance of the contact, R_{CONT}. A non-zero value for R_{CONT} gives rise to a finite, measurable voltage drop across the contact, which is the $V(0)$ given by Eq. (3.25). $V(0)$ can be calculated from Eq. (3.26) and from the slope dV/dx for $x < 0$ which is

$$\left.\frac{dV(x)}{dx}\right|_{x<0} = -\frac{IR_s}{Z} \tag{3.27}$$

Substituting gives:

51
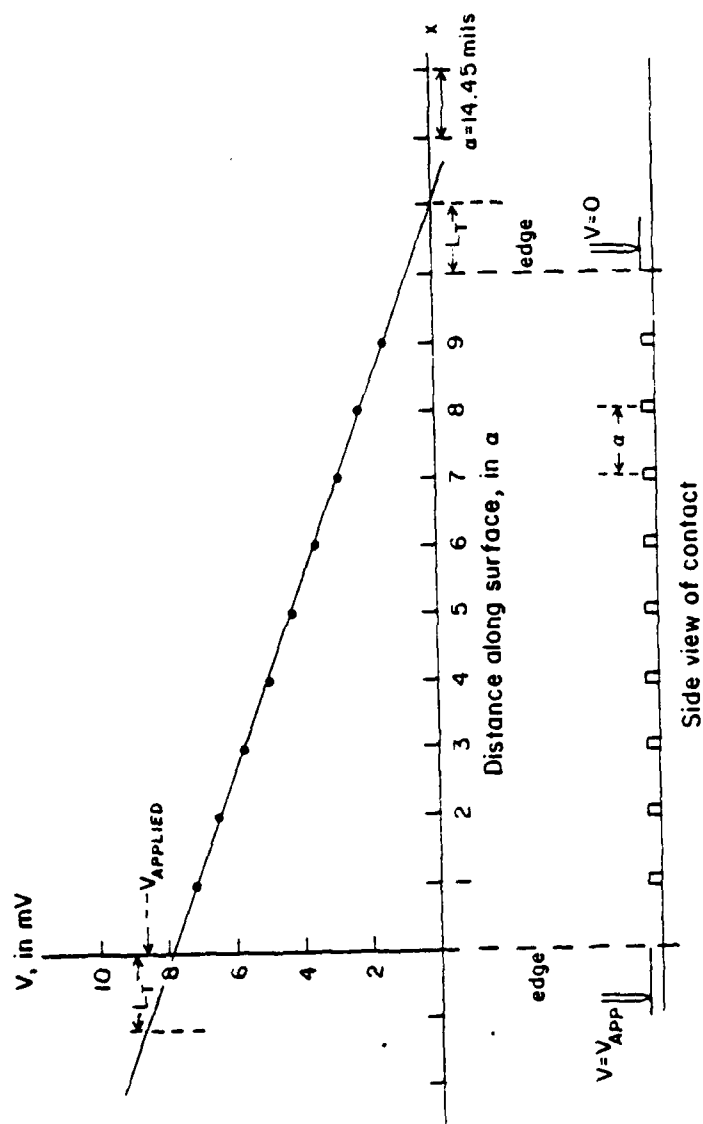
Figure 3.6 Typical transfer length plot

52

$$V(0) = \frac{I R_s L_T}{Z} \tag{3.28}$$

or:

$$R_{CONT} = \frac{V(0)}{I} = \frac{R_s L_T}{Z} \tag{3.29}$$

and substituting Eq. (3.17) for R_s gives:

$$R_{CONT} = \frac{R_c}{Z L_T} \tag{3.30}$$

Normally, when current flow is perpendicular to the interface, the contact resistance R_{CONT} is determined from R_c as:

$$R_{CONT} = \frac{R_c}{AREA} \tag{3.31}$$

However, for the above case, with lateral current flow into a planar contact, the apparent contact area is $Z L_T$ and is independent of actual contact length. Therefore, in a planar contact with a value of Rc giving rise to a small L_T, the current will crowd into the edge of the contact within an effective distance of L_T. In order to lower R_{CONT} for such contacts, the width, Z, can be made wider, but increasing the contact length, and with it the apparent area, will not reduce R_{CONT} through Eq. (3.31) as is commonly thought. Fang, et. al. (37) discuss this idea further.

According to the previous development, if $R_c = 0$ then $L_T = 0$. However, if $R_c = 0$ then the vertical IR drop through the conducting layer is no longer negligible in comparison to the IR_c drop and the previous treatment is in error. Hower (60) and Berger (61) give a correction factor but in most cases of non-zero R_c it can be neglected with little resulting error.

For the previous development an important assumption was that the contact length was infinite. Practically, if a transfer length plot is made and yields a value of L_T which is very much shorter than the physical length of the contact, then Eq. (3.17) is valid to use to determine R_c.

However, for cases in which R_c is not sufficiently small, as was the case for many contacts in this research, a transfer length plot can

53

yield an L_T value which is greater than the physical contact length, xc. Clearly in such a case the above assumption of an infinitely long contact is not valid and a more exact analysis must be performed.

The more exact analysis is based on the model given in Figure 3.7. This model is very similar to that of Figure 3.5 except for a finite contact length x_C and a change in coordinates. In this case, since it will be easier to perform an integration of current from right to left, the origin of the coordinate system is at the right end of the contact.

The basic assumptions used previously still hold. The conducting layer is described by a sheet resistivity of R_S. The layer is thin and voltage drops due to the vertical flow of current are negligible. The contact itself is perfectly conducting and is at ground potential. The effect of the MS interface is lumped into the distributed specific contact resistivity term R_C. Current enters the contact from the left of $\lambda = x_C$ and begins to be taken to ground through R_S. The contact width is equal to Z.

At any point, λ, the current lost to the contact, $dI(\lambda)$, is given by:

$$dI(\lambda) = \frac{V(\lambda)}{R_C} Z \, d\lambda \qquad (3.32)$$

Since all the current entering from the left, I_{TOT}, must eventually go into the contact between $\lambda = x_C$ and $\lambda = 0$:

$$I_{TOT} = \int dI(\lambda) = \int_0^{x_C} \frac{V(\lambda)}{R_C} Z \, d\lambda \qquad (3.33)$$

and this gives a boundary condition on $V(\lambda)$.

If V_0 represents $V(\lambda = 0)$, a constant which will be calculated later, the voltage $V(\alpha)$ at any point $0 < \alpha < x_C$, is the sum of V_0 and the total $R_S dI$ voltage drops up to that point giving:

$$V(\alpha) = V_0 + \int_0^\alpha dI(\lambda) \frac{R_S}{Z} (\alpha - \lambda) \qquad (3.34)$$

The $[R_S/Z](\alpha-\lambda)$ term is the resistance along the conducting layers up to the point $\lambda = \alpha$, through which $I(\lambda)$ flows creating a voltage drop.

If Eq. (3.34) is rewritten using Eq. (3.32) the result is:
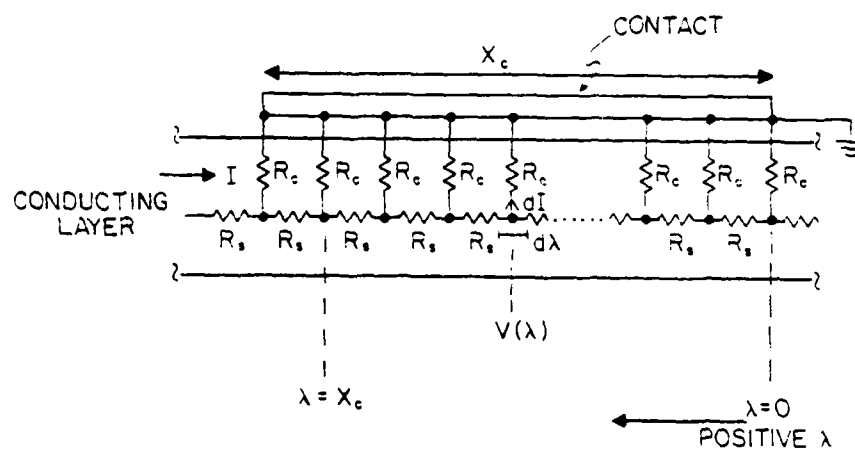
Figure 3.7   Model used for a finite length contact.

$$V(\alpha) = V_0 + \int_0^\alpha \frac{V(\lambda)}{R_c} R_s(\alpha-\lambda) \, d\lambda \qquad (3.35)$$

and this is the equation which must be solved to determine $V(\lambda)$.

If the derivative with respect to α is taken on both sides of Eq. (3.35) the result is:

$$\frac{d^2 V(\alpha)}{d\alpha^2} - \frac{R_s}{R_c} V(\alpha) = 0 \qquad (3.36)$$

which is the same as Eq. (3.24). This is to be expected since the only difference between the previous model and this more exact model lies in the boundary conditions. Therefore, the same relationship of

$$L_T = \left[\frac{R_c}{R_s} \right]^{1/2} \qquad (3.37)$$

can be made to define a transfer length relating R_c to R_s.

The solution to Eq. (3.36) with the condition of a finite V_0 at $\lambda = 0$ is:

$$V(\alpha) = V_0 \cosh \left(\frac{\alpha}{L_T} \right) \qquad (3.38)$$

If Eq. (3.38) is applied in the boundary condition of Eq. (3.33) for the total current, the result is:

$$V_0 = \frac{I_{TOT} R_c}{Z L_T \sinh\left(\frac{x_c}{L_T}\right)} \qquad (3.39)$$

and

$$V(\alpha) = \frac{I_{TOT} R_c}{Z L_T \sinh\left(\frac{x_c}{L_T}\right)} \cosh \left(\frac{\alpha}{L_T} \right) \qquad (3.40)$$

If, for comparison, the coordinate system is changed back to the same as that in the previous development, then :

$$\alpha = x_c - x \qquad (3.41)$$

and

$$V(x) = \frac{I_{TOT} R_c}{Z L_T \sinh\left(\frac{x_c}{L_T}\right)} \cosh \left(\frac{x_c - x}{L_T} \right) \qquad (3.42)$$

Eq. (3.42) is the more exact expression for Eq. (3.25). Given that:

$$\sinh \left(\frac{x_c}{L_T}\right) = \frac{\exp \left(\frac{x_c}{L_T}\right) - \exp \left(\frac{x_c}{L_T}\right)}{2} \tag{3.43}$$

and

$$\cosh \left(\frac{x_c - x}{L_T}\right) = \frac{\exp \left(\frac{x_c}{L_T}\right) \exp \left(\frac{x_c}{L_T}\right) + \exp \left(\frac{x_c}{L_T}\right) \exp \left(\frac{x_c}{L_T}\right)}{2}$$

$$\tag{3.44}$$

for the case of an infinitely long or semi-infinite contact in which $L_T \ll x_c$:

$$\frac{x_c}{L_T} \gg 1 \tag{3.45}$$

then

$$\sin h \frac{x_c}{L_T} \approx \frac{\exp \left(\frac{x_c}{L_T}\right)}{2} \tag{3.46}$$

and

$$\cosh \left(\frac{x_c - x}{L_T}\right) \approx \frac{\exp \left(\frac{x_c}{L_T}\right)}{2} \exp\left(- \frac{x}{L_T}\right) \tag{3.47}$$

and if Eqs. (3.46) and (3.47) are substituted into Eq. (3.42) the
result is:

$$V(x) = \frac{I_{TOT} R_c}{Z L_T \left[\frac{\exp \left(\frac{x_c}{L_T}\right)}{2}\right]} \frac{\exp \left(\frac{x_c}{L_T}\right)}{2} \exp \left(\frac{x_c}{L_T}\right) \tag{3.48}$$

or

$$V(x) = \frac{I_{TOT} R_c}{Z L_T} \exp \left(- \frac{x}{L_T}\right) \tag{3.49}$$

Since from Eq. (3.37):

$$R_c = R_s L_T^2 \tag{3.50}$$

Substituting into Eq. (3.49) gives:

$$V(x) = \frac{I_{TOT}R_c}{Z} \exp\left(-\frac{x}{L_T}\right) \tag{3.51}$$

which is the same as Eq. (3.25) and shows that the exact expression, given by Eq. (3.42), does become Eq. (3.25) in the limit of the simplified model's assumption of infinite contact length.

For the conducting layer portion $x < 0$:

$$\frac{dV(x)}{dx} = -\frac{I_{TOT}R_s}{Z_s} \tag{3.52}$$

Since Eq. (.52) must equal the slope of dV/dx at $x = 0$ as determined from Eq. (3.42),

$$\frac{dV(x)}{dx} = \frac{I_{TOT}R_c}{ZL_T\sinh\left(-\frac{x_c}{L_T}\right)} - \left(\frac{1}{L_T}\right) \sinh\left(\frac{x_c-x}{L_T}\right) \tag{3.53}$$

and at $x = 0$:

$$\left.\frac{dV(x)}{dx}\right|_{x=0} = \frac{I_{TOT}R_c}{ZL_T\sinh\left(-\frac{x_c}{L_T}\right)} - \left(\frac{1}{L_T}\right) \sinh\left(\frac{x_c-x}{L_T}\right) \tag{3.54}$$

or

$$\left.\frac{dV(x)}{dx}\right|_{x=0} = \frac{I_{TOT}R_c}{ZL_T^2} \tag{3.55}$$

and using Eq. (3.50),

$$\left.\frac{dV(x)}{dx}\right|_{x=0} = \frac{I_{TOT}R_s}{Z} \tag{3.56}$$

which is the same as Eq. (3.52) if $Z \approx Z_s$ is assumed.

The transfer length plot yields a value of transfer length when the $V(x)$ line is extended past the point $x = 0$, with a slope given by Eq. (3.52), and intersected with the $V(x) = 0$ axis. The equation of this extended line is given by:

$$V(x) = - \frac{I_{TOT}R_s}{Z}(x) + V(0) \qquad (3.57)$$

where $V(0)$ depends on whether Eq. (3.25) or Eq. (3.42) is used. For the case of an infinite contact, from Eq. (3.25):

$$V(0) = - \frac{I_{TOT}R_s L_T}{Z} \qquad (3.58)$$

therefore:

$$V(x) = - \frac{I_{TOT}R_s}{Z}(x) + \frac{I_{TOT}R_s L_T}{Z} \qquad (3.59)$$

and when $V(x) = 0$, $x = L_T$.

For the more exact case, using Eq. (3.42):

$$V(0) = - \frac{I_{TOT}R_c}{ZL_T} \frac{\cosh\left(\frac{x_c}{L_T}\right)}{\sinh\left(\frac{x_c}{L_T}\right)} \qquad (3.60)$$

and therefore (using $R_s = R_c/L_T^2$ in the $-I_{TOT}R_s/Z$ term):

$$V(x) = - \frac{I_{TOT}R_c}{ZL_T^2}(x) + \frac{I_{TOT}R_s L_T}{ZL_T} \frac{\cosh\left(\frac{x_c}{L_T}\right)}{\sinh\left(\frac{x_c}{L_T}\right)} \qquad (3.61)$$

and when $V(x) = 0$,

$$x = x_{LT} = L_T \frac{\cosh\left(\frac{x_c}{L_T}\right)}{\sinh\left(\frac{x_c}{L_T}\right)} \qquad (3.62)$$

where x_{LT} is referred to in this research as the apparent transfer length.

It is clear from Eq. (3.62) that for a given combination of R_C and R_S, a transfer length plot can yield a value of x_{LT} greater than x_C. In such cases a calculation of :

$$R_C = R_S(x_{LT})^2 \tag{3.63}$$

would be in error.

The solution, for cases in which the assumption is not valid, is to take the value of x_{LT} as determined from a transfer length plot and using the measured value of x_C in Eq. (3.62), calculate the proper value of L_T to use in Eq. (3.50).

Figure 3.8 is a graph of Eq. (3.62) giving the relationship between x_{LT} and L_T for an observed value of x_{LT} with respect to x_C. The figure was determined by first rewriting Eq. (3.62) as:

$$\frac{x_{LT}}{x_C} = \frac{L_T}{x_C} \frac{\cosh\left(\frac{x_C}{L_T}\right)}{\sinh\left(\frac{x_C}{L_T}\right)} = \frac{\cosh\left(\frac{x_C}{L_T}\right)}{\left(\frac{x_C}{L_T}\right)\sinh\left(\frac{x_C}{L_T}\right)} \tag{3.64}$$

Then, for various values of x_C/L_T, the right hand side of Eq. (3.64) was calculated to give x_{LT}/x_C. The product of the chosen x_C/L_T value and the resultant x_{LT}/x_C value gives the value of x_{LT}/x_C value gives the value of x_{LT}/L_T from:

$$\frac{x_C}{L_T} \cdot \frac{x_{LT}}{x_C} = \frac{x_{LT}}{L_T} \tag{3.65}$$

The figure then represents a plot of x_{LT}/x_C vs. x_{LT}/L_T.

To use Figure 3.8, first a measurement of x_{LT} is made and a value of x_{LT}/x_C is calculated. From the figure, the corresponding value of x_{LT}/L_T is found and L_T is calculated and used to find R_C/

The other approximation extreme is that $x_C/L_T \gg 1$ or even $x_C/L_T < 1$. This would occur if R_C was very much larger than R_S leading to a large L_T. In such a case, in the limit when $x_C/L_T \ll 1$:

$$\cosh\left(\frac{x_C}{L_T}\right) \approx 1 \tag{3.66}$$

and

$$\sinh\left(\frac{x_C}{L_T}\right) \approx \frac{x_C}{L_T} \tag{3.67}$$
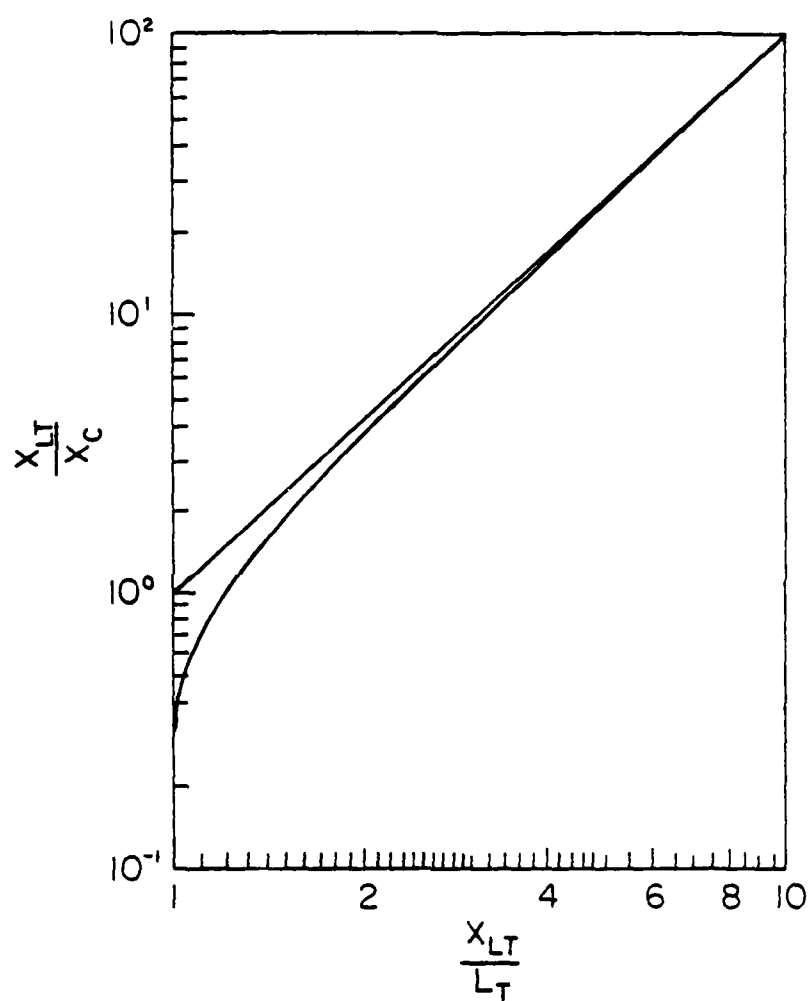
Figure 3.8 Relationship between apparent transfer length,
X_{LT}, actual transfer length, L_T, and contact
length, X_C.

61

These substituted into Eq. (3.60) give:

$$V(0) \approx \frac{I_{TOT}R_c}{ZL_T} \left[\frac{1}{\left(\frac{x_c}{L_T}\right)} \right]$$

simplifying to:

$$V(0) = \frac{I_{TOT}R_c}{Zx_c} \tag{3.68}$$

or

$$R_c = \frac{V(0)}{I_{TOT}} (Zx_c) \tag{3.69}$$

Eq. (3.69) is a statement that for R_c large in comparison to R_s, the IR drop in the contact is almost entirely across R_c. In such a case current crowding at the contact leading edge is minimal and most of the I_{TOT} current flow is perpendicular to the contact. With $V(0)$ being the voltage drop across this contact due to I_{TOT} and Zxc being the total contact area, Eq. (3.69) is the same as Eq. (3.31) giving R_{CONT} for a nonplanar contact.

In Figure 3.8, the straight line represents a plot of the equation:

$$\frac{x_{LT}}{x_c} = \left(\frac{x_{LT}}{L_T}\right)^2 \tag{3.70}$$

which is for the case when $x_c/L_T \ll 1$. The derivation of Eq. (3.70) from Eq. (3.64) is made using the above assumption and Eqs. (3.66) and (3.67).

From Figure 3.8 it is seen that if the value of $x_{LT} < 0.4\ x_c$, then the infinite x_c approximation of $x_{LT} = L_T$ is valid to about 1%. Also if $x_{LT} > 10\ x_c$, Eq. (3.69) can be used in a simple calculation using $V(0)$, I_{TOT} and contact area to find R_c accurate to about 1%.

Berger (61), using a transmission line model similar to Figure 3.7, developed equations for $V(x)$ and $I(x)$ which could be used to calculated Eq. (3.42) and the other subsequent equations. However, the development given in this section closely parallels the development presented on infinite length contacts, and therefore comparisons to to that case are more straightforward than if the method of Berger was used.

For the case of $x_c/L_T \ll 1$, it is very easy to determine R_c from Eq. (3.69) and from a measurement of the voltage, V_1 of the pick-off contact strip just before the end contact. The voltage drop across the contact, $V(0)$, is then given by:

$$V(0) = V_1 - \frac{I_{TOT}R_s\Delta L}{Z} , \qquad (3.71)$$

where ΔL is the separation between the voltage pick-off strip and the contact edge.

The model as shown in Figure 3.5 and Figure 3.7 strictly depicts current flow for a reverse biased MS contact when an n-type conducting layer is used. Actual contact performance in terms of R_c and the I-V response were measured on the opposite, forward biased contact, of the contact structure. However, all the equations developed herein can also be applied to the forward biased contacts since the models used are still the same. The only changes are in the sign of the current and the reference for the contact voltage, being V_{APP} instead of ground.

If an arbitrary reference of $V_{APP} = 0$ is used, then $V(x)$ for the forward bias contact will be negative and will represent the voltage difference between V_{APP} and the voltage in the conducting layer. The value of transfer length L_T or x_{LT} will have the same meaning and can be used in all the equations developed previously.

3.4 Current-voltage (I-V) measurement

Another important experimental measurement used in this research was the variation of current with voltage. It is easily seen from the I-V equations derived in Chapter II that the FE or TFE tunneling contact exhibits an exponential I-V response. For a forward bias greater than a few kT/q the slope of the I-V curve gives the value of E or E_o and from these the doping level under the contact can be determined. The extension of the I-V curve to the $V=0$ axis gives J_s, from which a value of ϕ_B can be calculated. Therefore, the major parameters used in detailing theoretical contact performance, ϕ_B and C_s, can be readily determined with I-V measurements.

The actual procedure used to determine ϕ_B and C_s by this method was first to measure I-V data on the various contact structures and then to curve fit the theoretical equations to the experimental data. A suitable fit meant that the general form of the equations, and therefore the general aspects of the Schottky model, were valid to use in explaining contact performance.

A stronger argument for the use of the tunneling model comes from relating the values of ϕ_B and C_s, as determined above, to values

63

of ϕ_B and C_s taken from other measurements. With the contact
structures used in this research, the other commonly used methods of
measuring ϕ_B were not applicable and a further discussion of this fact
will be given later. However, an independent measurement of C_s, using
the van der Pauw technique, did yield a value which could be compared
to that determined from an I-V measurements. If the values of C_s as
determined by the two different techniques are the same, then the
contacts are presumed to operate as tunneling contacts. A further
verification of tunneling operation was made when the ϕ_B and C_s values
from the I-V fit were used in the theoretical equations for R_c and
compared to the actual variation of R_c vs. temperature.

One problem in relating the theoretical I-V equations to
experimental data is that the current flow in the actual contact
structures is planar, giving rise to current squeezing at the edge of
the contact. The effect is analogous to the base current crowding in a
bipolar transistor and can be analyzed using the same equations (62).

However, for this research, a development of the effective I-V
response for the contact was performed using a model similar to those
given in the development of R_c. The only difference is that in the
model instead of a distributed R_c, distributed diodes with a response:

$$J = J_S \exp \left(\frac{qV}{E'}\right) \tag{3.72}$$

were used. The basic form of Eq. (3.72) is valid for both FE and TFE
operation, as can be seen by comparison to Eq. (2.40) and Eq. (2.58)
(for biases greater than a few kT/q). For the FE case:

$$E' = E_\infty \tag{3.73}$$

and for the TFE case:

$$E' = E_o \tag{3.74}$$

There is a slight dependence in J_S on V but since the effect of
V through the exponential term is the dominant factor, the dependence
in the J_S term can be neglected with only sight error.

Figure 3.9 shows the model of the contact as changed for use in
the development of the I-V equations. The figure shows the case of a
forward bias contact made on an n-type conducting layer with sheet
resistivity R_s. As before, voltage drops due to vertical current flow
in the conducting layer are neglected. For convenience, the voltage on
the metallic contact of length x_c is taken as ground. Therefore, the
values derived for voltage in the conducting layer, $V(x)$, will be nega-
tive.

The total current flowing through the contact is I_{TOT} and enters
the conducting layer a point $x = x_c$.   Since the voltage, $V(x)$, for

64
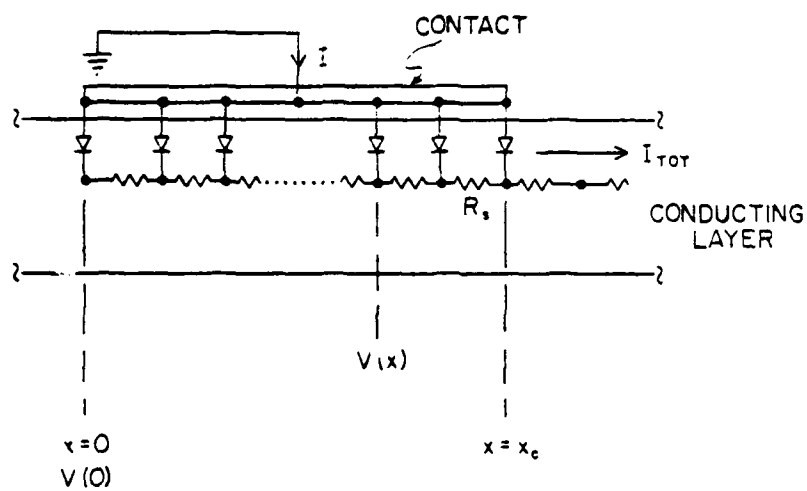
Figure 3.9 Model used to derive I-V equations for the
            planar contact structure.

$0 < x < x_c$ cannot actually be measured, experimental data consists of a measurement of I_{TOT} vs. $V(x = x_c)$/ Actually, $V(x_c)$ also cannot be directly measured but can be easily determined from the measured voltage, V_1, of the first voltage pick-off strip to the right of the contact. Namely:

$$V(x_c) = V_1 + \frac{I_{TOT}R_s\Delta L}{Z} \tag{3.75}$$

Eq. (3.75) is exactly the same as Eq. (3.71) taking into account that the direction of current flow is reversed. The ΔL is the difference in distance between the $x = x_c$ point and the location of the voltage pick-off strip.

The incremental current flow through the contact at any point x is given by:

$$I(x) = J(x)Zdx \tag{3.76}$$

where $J(x)$ is given by Eq. (3.72). The voltage at any point $0 < x < x_c$ is the difference between $V(x = 0)$ and the total IR_s drops up to point x. Therefore, analogously to Eq. (3.34):

$$V(x) = V(0) - \int_0^x J(y)Z \frac{R_s}{Z}(x-y)dy \tag{3.77}$$

Since $V(0)$ is a constant, taking the derivative of both sides gives:

$$\frac{dV(x)}{dx} = -\int_0^x J(y)R_s dy \tag{3.78}$$

Taking the derivative again gives:

$$\frac{d^2V(x)}{dx^2} = -J(x)R_s \tag{3.79}$$

and using Eq. (3.72) gives:

$$\frac{d^2V(x)}{dx^2} = -R_s J_s \exp\left(-\frac{qV(x)}{E}\right) \tag{3.80}$$

and this is the equation which must be solved for $V(X)$. (If the assumption is made, as used in the calculation of L_T, that $J(x)$ is given by a linear $V(x)/R_c$ term, then Eq. (3.36) results.)

The boundary conditions are determined from the fact that all incremental $dI(x)$'s must add up to I_{TOT} when $x = x_c$. Therefore:

$$\int_{o}^{x_c} J(y)Zdy = I_{TOT} \tag{3.81}$$

and using Eq. (3.78) gives the conditions:

$$\frac{dV(x)}{dx}\bigg|_{x = 0} = 0 \tag{3.82}$$

and

$$\frac{dV(x)}{dx}\bigg|_{x = x_c} = -\frac{R_s I_{TOT}}{Z} \tag{3.83}$$

The solution for $V(x)$ is easily calculated assuming a form:

$$V(x) = A \ln[u(x)] \tag{3.84}$$

with A a constant and $u(x)$ of the form:

$$u(x) = K \cos \gamma x \tag{3.85}$$

With the above assumptions, the solution is given by :

$$V(x) = \frac{2E'}{q} \ln\left[(\frac{qR_s J_s}{2E'})^{1/2} \frac{\cos \gamma x}{\gamma x} \right] \tag{3.86}$$

The parameter, γ , depends on the boundary conditions as given in Eq. (3.83) and is determined from:

$$\gamma \tan (\gamma x_c) = \frac{qI_{TOT}R_s}{2E'Z} \tag{3.87}$$

where Z = contact width

x_c = contact length

q = electronic charge

As a check on Eqs. (3.86) and (3.87) the limiting case of $R_s \rightarrow 0$ can be examined. For $R_- \rightarrow 0$, the IR_s voltage drops go to zero and the current crowding at the edge is reduced. In this case the dominant voltage drop is $V(x)$ across the contact itself and lateral current flow does not have a large effect. The contact itself and lateral current flow does not have a large effect. The contact I-V should tend to that

57

for a contact with perpendicular current flow.

From Eq. (3.87), when $R_s \to 0$ then $\gamma \to 0$ and therefore $\gamma x_c \to 0$. Therefore:

$$\sin(\gamma x_c) \to \gamma x_c \tag{3.88}$$

and

$$\cos(\gamma x_c) \to 1 \tag{3.89}$$

and

$$\tan(\gamma x_c) \to \gamma x_c \tag{3.90}$$

substituting in Eq. (3.87) gives:

$$\gamma^2 x_c = \frac{q I_{TOT} R_s}{2E'Z} \tag{3.91}$$

or

$$\gamma = \left[\frac{q I_{TOT} R_s}{2E' x_c Z} \right]^{1/2} \tag{3.92}$$

The voltage called the "contact voltage" in an experimental measurement is $V(x_c)$. Therefore, substituting Eqs. (3.92) and (3.89) in Eq. (3.86) for $V(x_c)$ gives:

$$V(x_c) = \frac{2E'}{q} \ln \left[\left(\frac{q R_s J_s}{2E'} \right)^{1/2} \left(\frac{2E' Z x_c}{q I_{TOT} R_c} \right)^{1/2} \right] \tag{3.93}$$

or simplified and rearranged:

$$I_{TOT} = J_s (Z x_c) \exp \left[-\frac{q V(x_c)}{E'} \right] \tag{3.94}$$

since $Z x_c$ is the contact area then, as expected, Eq. (3.94) is the I-V equation for a MS diode with perpendicular current flow for biases greater than a few kT/q.

In using Eq. (3.86) and (3.87) in curve fitting, the terms of R_s, Z, and x_c were given data. Terms Z and x_c were determined from dimensional measurements and R_s was determined from the van der Pauw measurement.

For an assumed value of E' and J_s, γ was calculated using Eq. (3.87) for a specified I_{TOT}. Then, using γ and Eq. (3.86), the corresponding contact voltage, $V(x_c)$, for that value of I_{TOT} was calculated. These steps were performed for a range of I_{TOT} values and the resulting I_{TOT} vs. $V(x_c)$ response was compared to the experimental I-V data. The initial assumptions of E' and J_s were then changed and the procedure repeated until a good fit between theoretical and experimental data was achieved.

In using the values of E' and J_s to find ϕ_B and C_s, the type of emission, FE or TFE, needed to be determined. The value of E' was first set equal to E_0 and Eq. (2.56) was used to find E_∞. This meant that the emission was initially assumed to be TFE. Using the resulting value of E_∞ in Eq. (2.11) the doping level, C_s, (actually N_D) was calculated.

Using the calculated value of C_s, a value for the Fermi level, n_F, was calculated. Using these values of E_∞ and n_F and using Eq. (2.45), a value of f_1 was calculated. Since Eq. (2.25) :

$$\frac{1}{kT} - C_1 > (2f_1)^{1/2} \tag{2.25}$$

must be satisfied in order for the emission to be FE, the calculated value of f_1, was used to find C_{1MAX} for the given T from:

$$C_{1MAX} = \frac{1}{kT} - (2f_1)^{1/2} \tag{3.95}$$

This value of C_{1MAX} was used in Eq. (2.44):

$$C_1 = \frac{\ln(\frac{4\phi B}{n_F})}{2E_\infty} \tag{2.44}$$

to determine a value of ϕ_{BMAX}. Since the value of J_s is inversely proportional to ϕ_B, use of ϕ_{BMAX} in Eq. (2.41) to determine J_s under FE, results in the minimum value of J_s, J_{SMIN}, which would be possible and still have the emission be FE.

69

Using the value of E' obtained from the best fit, a value of E_∞ was calculated and J_{SMIN} determined. If the value of J_S from the curve fit is less than J_{SMIN}, then a $\phi_B > \phi_{BMAX}$ is needed. However, $\phi_B > \phi_{BMAX}$ results in $c > c_{1_{MAX}}$ which violates Eq. (2.25) for the given E_∞. Therefore, if J_S from the curve fit is less than J_{SMIN} as determined above, the emission cannot be FE.

If J_S from the curve fit is greater than J_{SMIN} then a ϕ_B does exist in the range that allows Eq. (2.25) to be satisfied and still fit J_S and E_∞ to the FE equation. In such a case, the value of J_S is used in Eq. (2.41) to determine a value of ϕ_B . This ϕ_B and the value of C_S calculated before then represent the Schottky barrier conditions necessary to result in the experimental I-V data for that particular sample.

The initial assumption of $E' = E_o$ instead of $E' = E_\infty$ causes no problem in the above procedure, even though for the case where $J_S > J_{SMIN}$, and the emission is FE, the E' actually represents E_∞ and not E_o. This is because, in the range where Eq. (2.25) is satisfied and FE is indicated, the appropriate E_∞ values, when put into Eq. (2.56) result in $E_o \approx E_\infty$. Therefore, an initial assumption of $E' = E_o$, instead of $E' = E_\infty$, causes no problem even if FE is indicated in further calculation.

From some actual experimental data at room temperature, if the above calculation indicates that the emission is FE, then the value of E_o from Eq. (2.56) is equal to E_∞ well within 1%. Therefore, the initial assumption of $E' = E_o$ instead of $E' = E_\infty$ is only off by a very small factor.

For the case where the above comparison of J_S and the calculated J_{SMIN} results in $J_S < J_{SMIN}$, the emission is not FE and Eq. (2.41) was not used. This meant that the emission may be TFE. Using the same values of $E' = E_o$, and calculated values of E_∞ , n_F , and N_D, Eq. (2.59) with $V = 0$ was used to calculate a ϕ_B to match the measured J_S to the J_S expected under TFE.

To check whether the calculation for TFE was strictly valid, the calculated values of E_∞, n_F , and ϕ_B were used in Eq. (2.61). If Eq. (2.61) was satisfied then the use of Eq. (2.59) was strictly valid. If Eq. (2.61) was not satisfied then there is a combination of FE and TFE occuring and the value of J_S as calculated using Eq. (2.59) is slightly in error.

3.5 Other measurements

In addition to an I-V measurement, there are two other types of measurements which are commonly made to find ϕ_B, a C-V measurement, and a photoelectric measurement (9).

The C-V technique measures the variation in space charge region capacitance of a Schottky barrier with reverse bias voltage. A plot of $(1/c^2)$ vs. V_R gives a line whose slope is related to doping, C_s, and whose extrapolated intercept on the $(1/c^2) = 0$ axis gives ϕ_B.

For this research the C-V technique was attempted but was unsuccessful. The source of difficulty was the large tunneling current. In a normal diode structure the only current flow under reverse bias is due to leakage and saturation currents and is very small. In this research, because C_s is large in order to realize tunneling and give a low R_c, a large current flows under reverse bias and the presence of this current appears as a large leakage resistance. Most instruments cannot measure the variation in C when a large effective leakage resistance is present and such was the case here.

The photoelectric technique is used to measure the variation in photo-generated current versus photon energy for a Schottky barrier illuminated by a monochromatic light source. The mechanism involved is the photoelectric excitation of an electron, at the Fermi level in the metal, up over the Schottky barrier thereby contributing to current flow.

The problem encountered when such measurements were tried on the contact structures used in this research was that no detectable photo-current was observed. The reason is that the relatively thick metal layer does not allow the penetration of incident photons down to the region next to the MS interface where they could excite electrons. Electrons excited away from MS interface recombine before they can reach the junction and therefore do not give rise to any measurable photo current.

In addition to the problem of the thickness of the Au, the relationship between photon energy and ϕ_B in the presence of electron tunneling through a thin barrier is not well known. In the theory usually used with the photoelectric technique it is assumed that the photocurrent is due only to electrons emitted over the barrier. However, for this research, the contacts exhibited appreciable current flow due to tunneling. Electrons excited thermally, as in TFE, or photoelectrically would be expected to be able to tunnel in a similar manner and therefore photoelectric current data for contacts in which tunneling occurs may yield erroneous values of ϕ_B if the simple emission theory is used.

SECTION IV

EXPERIMENTAL DATA

4.1 Diffusions

The GaAs starting substrates were obtained from Crystal Specialities (64) and the manufacturer's specifications were:

p-type	Zn doped
Carrier concentration	$5 \times 10^{16}/cm^3$
Mobility	378.6 cm / V-sec
Orientation	(100)
Resistivity	0.37 Ω cm
Wafer thickness	18 mils
One side polished	

Small sections of each wafer were scribed out and cleaned with a trichloroethylene, acetone, methanol, and H2O wash sequence. Ohmic contacts were made to the periphery of the polished side by alloying small dots of In-- 2% Zn alloy in an annealing furnance at 225° for 10 min. The I-V curve of the sample and contacts was observed on a curve tracer to check for ohmicity.

Each main wafer was then retested to determine average resistivity, $\bar{\rho}$, carrier concentration, C_B, and mobility, μ_H, with the van der Pauw, Hall effect technique. Table 4.1 lists the results of this measurement. The entries in Table 4.1 differ from the manufacturer's data but these measured values were taken to be the more valid characterization of the starting wafers.

Before each diffusion, the wafers to be diffused were given a standard wash and etch preparation as listed in Table 4.2. The MB etch was reported to result in the least number of surface defects (21).

After cleaning, the Sn dopant solution was spun on the wafer surface. As explained in Section II, the spin-on dopant solution was a mixture of Sn bearing Tinsilicafilm and undoped Silicafilm. The proportions of the two solutions were varied to give different values of

73

dopant surface concentration. After spin on, the film was densified into a Sn bearing Si2 layer by hearing the wafer for 20 min to 1 hour at 200°C in a furnace. A normal air atmosphere was present.

The dopant coated wafers were placed in a closed but not tightly sealed capsule along with extra As and GaAs pieces. The diffusion was at 950°C for 6 hours. An Ar flow was maintained in the diffusion furnace. The arsenic released during the diffusion was kept out of the room by means of a scavenger box located at the mouth of the furnace. Figure 4.1 is a photograph of the diffusion furnace set up.

Table 4.1

GaAs Starting Substrate Specifications

Sample #	$\overline{\rho}$ Ω-cm x 10^{-1}	μ_H cm^2/V-sec x 10^2	C_B/cm^3 x 10^{17}
3A-1	1.65	1.937	1.95
4A-1	2.40	2.367	1.10
5A-1	1.46	2.135	2.00
6A-1	1.44	2.220	1.96
7A-1	1.46	2.155	1.98
8A-1	2.52	2.417	1.03

Table 4.2

Wafer Preparation Process

1. 1 min. wash in trichloroethylene in ultrasonic cleaner.

2. 1 min. wash in acetone in ultrasonic cleaner.

3. 1 min. wash in methanol in ultrasonic cleaner.

4. Rinse and soak in high purity (18 MΩ-cm) H_2O.

5. MB etch for 2 min.

   1 HF : 1 HCL : 4 H_2O +   1 drop H_2O_2/ 10 ml of solution

6. Rinse in 18 M Ω-cm H_2O.

7. Blow dry with prepurified N_2.

8. Store in petri dish.

Table 4.3

Diffused Layer Data Determined from van der Pauw Measurements

Diffused Sample #	x_j microns	$\bar{\rho}$ Ω-cm x 10^{-1}	μ_H cm^2/V-sec x 10^2	C_B/cm^3 x 10^{18}
4A-1	1.64	1.35	1.561	2.96
5A-1	1.37	1.31	1.431	3.33
6A-1	1.47	1.54	1.350	3.00
7A-1	1.02	2.46	1.365	1.87
8A-1	1.64	3.99	1.412	1.11
5-2	1.58	1.62	1.611	2.40
5-3	1.83	2.06	1.609	1.89
5-4	1.73	2.13	1.675	1.75
6-1	1.91	1.16	1.678	3.21
6-2	1.68	1.77	1.631	2.16
6-3	1.67	2.33	1.709	1.57
6-4	1.44	1.78	1.482	2.37
6-5	1.09	2.09	1.937	1.54
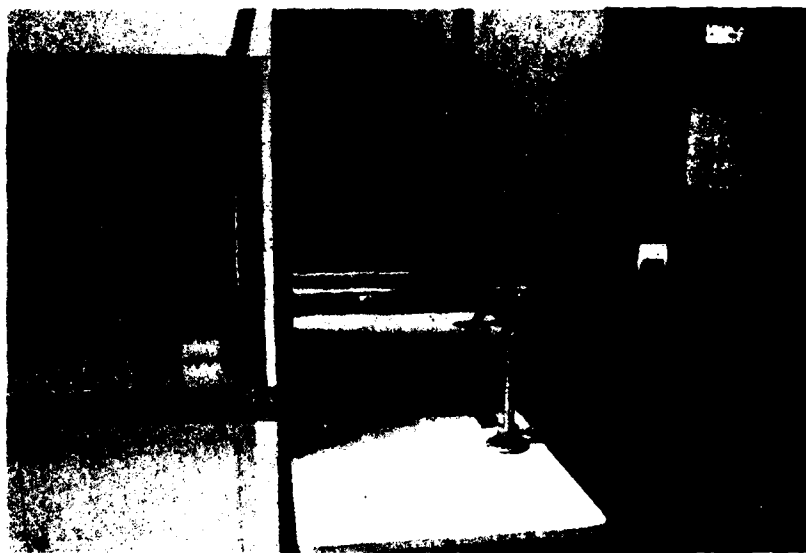
Figure 4.1   Photograph of the diffusion furnace equipment.

Pieces of the diffused wafers were hand lapped with 0.3 μ
alumina powder on a glass plate and the junction was delineated using a
commercial staining solution (48) and exposure to light from a micro-
scope lamp. Junction depths, x_j, were then measured with a Watson
interferometer.

The n-type layers were then characterized with van der Pauw Hall
effect measurements, and values of layer average resistivity, $\bar{\rho}$,
average Hall mobility, $\bar{\mu}_H$, and average carrier concentration $\bar{N}_D$, were
determined. The results of the junction depth measurements and van der
Pauw measurements are given in Table 4.3.

Using the curve of $\bar{\rho}$ vs. C_S for full ionization, Figure 3.3, and
the values of $\bar{\rho}$ from the van der Pauw measurements, the value of C_S for
each sample can be determined. These values are listed in Table 4.4.

C_S can also be determined using the equation:

$$C(x) = C_S \text{erfc} \frac{x}{\sqrt{Dt}} \qquad (4.1)$$

if the diffusion coefficient, D, for Sn in GaAs at the diffusion
temperature is known. Assuming full ionization, when $x = x_j$, then $C(x)$
$= C_B$. Therefore:

$$C_B = C_S \text{erfc} \frac{x_j}{2\sqrt{Dt}} \qquad (4.2)$$

and C_S cam be determined.

The value of D for Sn in GaAs has been investigated by various
researchers and is usually given in the form:

$$D = D_o \exp(-\frac{E_o}{kT}) \qquad (4.3)$$

and Fane and Goss (66) gave data from which values of

$$D_o = 4.957 \times 10^{-2} \qquad (4.4)$$

$$E_o = 2.725 \text{ eV} \qquad (4.5)$$

can be calculated. These are also reported in Kendall (67) and Casey
(68). Kendall, gives a plot of Eq. (4.3) based on Fane and Goss's
data, but Casey, stating that his listed values are also from Fane and
Goss's work, nevertheless gives different values of D_o and E_o. Casey
gives values of:

$$D_o = 3.8 \times 10^{-2} \tag{4.6}$$

$$E_o = 2.7 \text{ eV} \tag{4.7}$$

Goldstein and Keller (69), (also reported in Madelung (58)), give:

$$D_o = 6 \times 10^{-4} \text{ cm}^2/\text{sec} \tag{4.8}$$

$$E_o = 2.5 \text{ eV} \tag{4.9}$$

valid over their experimental temperature range of 1069° C to 1215° C, but possibly Eq. (4.3) can be extrapolated with their values down to the temperature range less than 1069° C.

Tuck and Badawi (44) report that the diffusion coefficient depends on the nature of the substrate, giving slightly different values if the substrate is undoped or previously doped n-type. They do not report data for a p-type substrate but their data for the undoped substrate case can be used as a comparison. Their values are:

$$D_o = 3.5 \text{ cm}^2/\text{sec} \tag{4.10}$$

$$E_o = 3.3 \text{ eV} \tag{4.11}$$

Using the above data, the value of D for a diffusion temperature of 950° C can be calculated, resulting in:

$$D_1 = 2.99 \times 10^{-13} \text{ cm}^2/\text{sec} \qquad \text{with Fane and Goss} \tag{4.12}$$

$$D_2 = 3.056 \times 10^{-14} \text{ cm}^2/\text{sec} \qquad \text{with Goldstein and Keller} \tag{4.13}$$

$$D_3 = 9.066 \times 10^{-14} \text{ cm}^2/\text{sec} \qquad \text{with Tuck and Badawi} \tag{4.14}$$

The research of Fane and Goss actually showed non-erfc profiles and their data was determined by a curve fit to a portion of their observed profiles. Goldstein and Keller observed Gaussian type profiles because of their limited source of Sn. Tuck and Badawi observed good erfc profile fits over a large portion of the Sn diffusion profile.

Using the values of D_1, D_2, D_3 in Eq. (4.3), along with t = 6 hours, a value of C_s can be determined for a given C_B and x_j. The results of such calculations are presented in Table 4.4. The results will be discussed in Section V.

4.2 Contact fabrication

After the diffusion had been characterized via the above, the wafers were prepared for Au contact fabrication. The wafers were given the same wash sequence as outlined in Table 4.2, except for the etch step. Each wafer was then coated with photoresist and exposed to the

Table 4.4

Values of Surface Concentration of the Diffused Layers

Determined from Resistivity Calculations

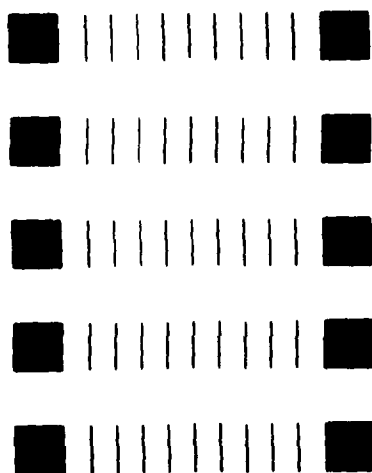| Sample #	x_j Microns	C_B/cm^3 $\times 10^{17}$	C_s from $\rho - C_s$ curve $\times 10^{18}$	C_s from D_1 $\times 10^{17}$	C_s from D_2	C_s from D_3 $\times 10^{19}$
4A-1	1.64	1.10	6.5	7.38	1.72×10^{22}	1.25
5A-1	1.37	2.00	6.3	8.77	1.23×10^{21}	0.70
6A-1	1.47	1.96	4.8	10.0	3.75×10^{21}	1.04
7A-1	1.02	1.98	2.5	5.33	4.05×10^{19}	0.18
8A-1	1.64	1.03	1.4	6.91	1.61×10^{22}	1.17
5-2	1.58	2.00	4.6	10.21	1.46×10^{22}	1.72
5-3	1.83	2.00	3.2	.87	4.22×10^{23}	5.78
5-4	1.73	2.00	3.0	1.56	1.04×10^{23}	3.50
6-1	1.91	1.96	7.7	2.11	1.33×10^{24}	8.60
6-2	1.68	1.96	4.0	1.40	5.18×10^{22}	2.70
6-3	1.67	1.96	2.7	1.38	4.55×10^{22}	2.57
6-4	1.44	1.96	4.0	9.56	2.64×10^{21}	0.92
6-5	1.09	1.96	3.1	5.80	7.26×10^{19}	2.40

81
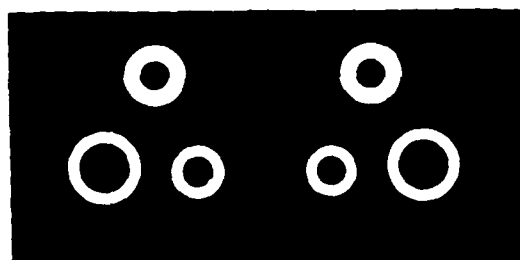
Figure 4.2   Contact mask.
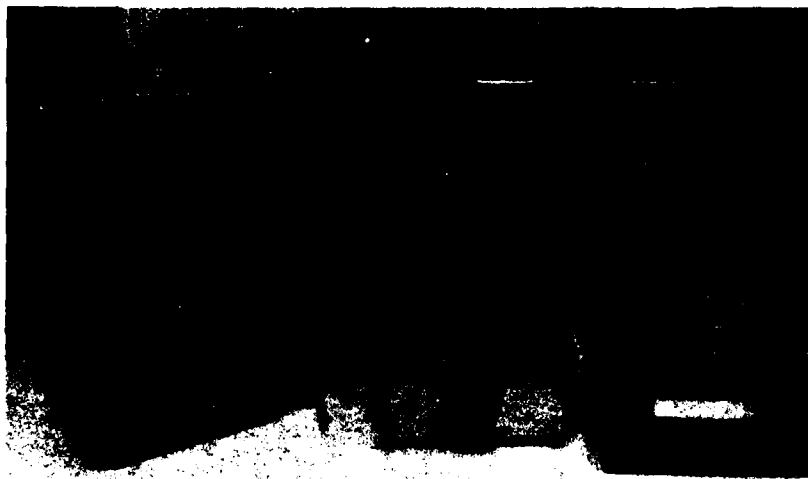
Figure 4.3   Photograph of the test apparatus used to

determine R_c from a measurement of transfer

length.
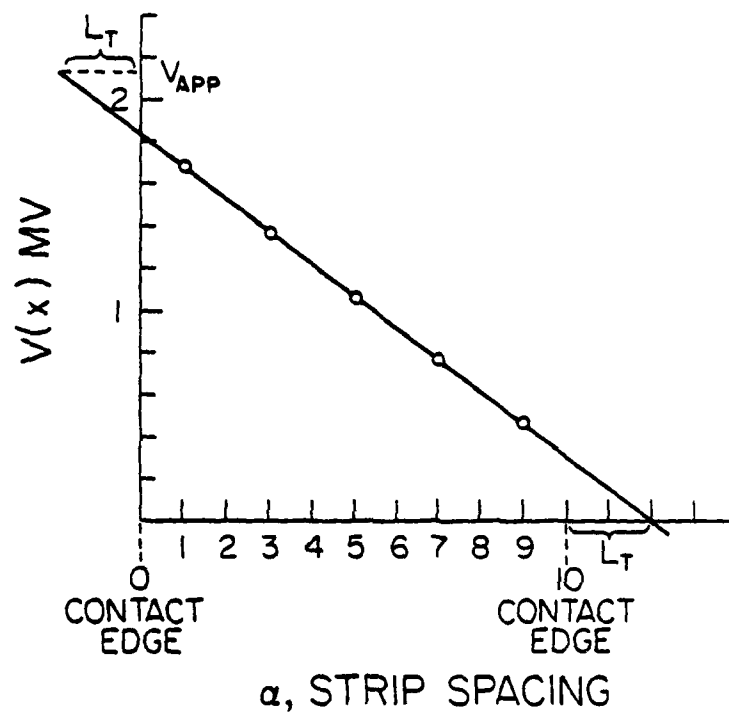
Figure 4.4 Example transfer length plot. Sample # 6-1B.
T = 18.8°C. I = 50 μA. (α = 3.66 x 10^{-2} cm.)

contact mask. The structure of the mask is shown in Figure 4.2. After the pattern was exposed and developed the photoresist layer had openings where the Au contacts would be made.

The patterned wafers were given a coating of approximately 1500Å of evaporated Au. The evaporation used 6" of 20 mil diameter Au wire placed in an evaporation boat 12" away from the substrates. The electrical power applied to the evaporation boat was gradually increased until evaporation began and was waintained at a level which resulted in all the gold in the boat being evaporated in two or three minutes.

After the evaporation, the Au coated wafers were soaked in acetone for up to one hour or until lift off of the unwanted Au occured. If a clean lift off was not obtained after the one hour, the beaker was given a short dip on an ultrasonic cleaner to force the unwanted Au to lift off. In most cases this technique gave acceptable results.

After the Au patterning, each wafer was given a low temperature, $\approx 250°$ C, anneal in N_2 for 5 minutes to promote better contact adhesion and to try and eliminate any possible interface nonuniformities. The individual contact structures were then scribed apart, ready for testing with the transfer length measurement.

4.3 Measurement of contact resistivity

For the transfer length measurements, a constant DC current was supplied through the sample using a Keithly 225 current source. The current level was chosen so that the voltage drop across the contact would be on the order of a few millivolts. This would give a good approximation to the V = 0 condition used in defining R_C. The voltages were measured with respect to the contact pad where the current exited using a Keithly 191 DVM. Contact to the pads and pick-off strips was made with tungsten tipped micromanipulator probes. Figure 4.3 is a photograph of the test set up. The probe stage rested on a thermoelectric cold plate which was used for subsequent measurements of Rc vs. T.

As an example, Figure 4.4 is the transfer length plot for sample #6-1B. The plot is for a temperature of 18.8° C, and the contact structure had a width, $Z_S = 0.0937$ cm.

The pick off strip spacing, α, is equal to 3.66×10^{-2} cm and the contact pad width and length is $\approx 7 \times 10^{-2}$ cm. Only voltages from every other pick off strip were taken. The current was I = 50 µA.

The straight line drawn on Figure 4.4 is a least squares fit to the data. The equation for the line is:

$$V(\alpha) \;=\; -0.154\,\alpha \;+\; 1.834 \text{ mV}$$

given in units of α. The total applied voltage was:

$$V_{APP} \;=\; 2.132 \text{ mV} \tag{4.16}$$

Therefore, the apparent transfer length, x_{LT}, for the forward bias contact is given as $|\alpha|$ when $V(\alpha) = V_{APP}$. Solving for α gives:

$$x_{LT} \;=\; |\alpha| \;=\; \left| \frac{2.132 \text{ mV} - 1.834 \text{ mV}}{-0.154 \text{ mV}/\alpha} \right|$$

$$x_{LT} \;=\; 1.94\,\alpha \tag{4.17}$$

and for the reversed bias contact (voltage reference contact), x_{LT} is found from α when $V(\alpha) = 0$. Or:

$$x_{LT} \;=\; \frac{1.834 \text{ mV}}{0.154 \text{ mV}/\alpha} \;-\; 10\,\alpha$$

$$x_{LT} \;=\; 1.92\,\alpha \tag{4.18}$$

It is seen that the values of x_{LT} are nearly the same in both cases. Actually, R_C for both forward and reverse biased contacts should become equal in the limit as $V \to 0$, since the I-V curve is continuous at $V = 0$. If x_{LT} values for the two contacts are very different, then contact non-uniformity due to processing variations is probably the cause.

The value of R_x can be calculated from:

$$R_S \;=\; - \frac{dV}{dx}\, \frac{Z_s}{I} \tag{3.18}$$

For sample #6-1B from Eq. (4.15):

$$\frac{dV}{dx} \;=\; -0.1538 \text{ mV}/\alpha \;=\; -4.20 \times 10^{-3} \text{ V/cm}$$

since $\alpha = 3.66 \times 10^{-2}$ cm. Therefore, with $Z_s = 0.0937$ cm and $I = 50$ μA:

$$R_S = \frac{(4.2 \times 10^{-3})\,(0.0937)}{50}$$

$$R_S = 7.87 \;\Omega/\text{square} \tag{4.19}$$

since for the diffused layer:

$$\bar{\rho} = R_S x_j \tag{4.20}$$

and with $x_j = 1.911 \times 10^{-4}$ cm for samples from wafer #6-1B :

$$\bar{\rho} = (7.87)\,(1.911 \times 10^{4})\;\Omega\text{-cm}$$

$$\bar{\rho} = 1.5 \times 10^{-3}\;\Omega\text{-cm} \tag{4.21}$$

This value of $\bar{\rho}$ is fairly close to the value of $\bar{\rho}$ in Table 4.3, determined by van der Pauw measurements. The difference is most likely due to the assumption that I flows through the entire structure width, Z_S whereas the actual contact pad width is somewhat less than Z_S.

Since the contact length, x_c, is $\approx 7 \times 10^{-2}$ and $x_{LT} \approx 1.9\,\alpha =$ 6.95×10^{-2} cm:

$$\frac{x_{LT}}{x_c} \approx 1$$

This means that the assumption of inifinite contact length as discussed in Chapter III is not strictly valid. From Figure 3.8 for $x_{LT}/x_c \approx 1$:

$$\frac{x_{LT}}{L_T} \approx 1.2 \tag{4.22}$$

or

$$L_T = \frac{x_{LT}}{1.2}$$

Therefore:

$$L_T = 5.8 \times 10^{-2}\; \text{cm} \tag{4.23}$$

and $R_c = R_S L_T^2$ gives:

$$R_c = (7.87)\,(5.8 \times 10^{-2})^2$$

$$R_c = 2.65 \times 10^{-2}\;\Omega\text{-cm}^2 \tag{4.24}$$

In most cases, the transfer length plot yielded a very linear $V(x)$ variation. Therefore, a much simpler method to find x_{LT} was used. For any particular contact structure, the width, Z_s, was measured and R_s was calculated from the van der Pauw value of $\bar{\rho}$ and x_j. Then Eq. (3.18) :

$$\frac{dV}{dx} = - \frac{I R_s}{Z_s} \qquad (4.25)$$

When Eq. (4.25) is given in units of α , then $\Delta V = -dV/d\alpha \cdot 10\alpha$ where ΔV is the IR drop along the entire conducting layer. The voltage drop across the contacts due to R_c was assumed to be equal and therefore:

$$V_{CONT} = \frac{V_{APP} - \Delta V}{2} \qquad (4.26)$$

The value of x_{LT} is then calculated from:

$$x_{LT} = \frac{V_{CONT}}{- \frac{dV}{d\alpha}} \qquad (4.27)$$

In most of the cases in this research, the level of C_s was such that $x_{LT} \gg x_c$, implying large values of R_c. Since the asymtotic approximation from Figure 3.8 is valid, R_c can be calculated from:

$$R_c = \frac{V_{CONT}}{I} x_c Z \qquad (4.28)$$

where x_c is the contact length and Z is the contact width.

Experimental values of R_c measured at $T = 23°$ C for various contact samples are shown in Figure 4.5. They are plotted against the value of C_s for that particular sample as determined from the van der Pauw measurement of $\bar{\rho}$ (Table 4.4).

Immediately apparent is the fact that not all the points lie on a single ϕ_B line as would be expected if ϕ_B were governed by Fermi level pinning. Since this result suggested that ϕ_B varied with processing, I-V curves for various contacts were measured to determine independently whether or not ϕ_B was varying.
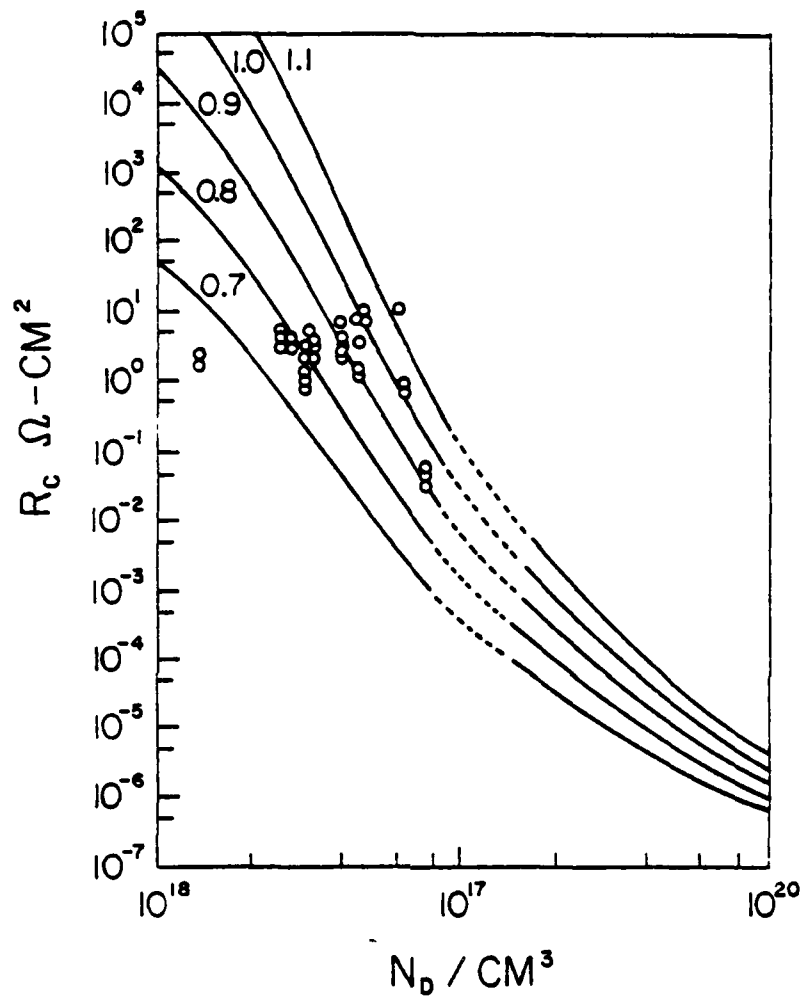
88

Figure 4.5 Measured values of R_c plotted against C_s for the
sample as determined from $\overline{\rho}$ measurements. Solid
lines are theoretical values. T = 23°C.

89

4.4 Current-voltage measurements

The measurement of the I-V response of the contacts was performed by the method explained in Section III. The DC current was supplied with a Keithly 225 DC current source and the voltage drops were measured with a Keithly 191 DVM. The voltage drop across the contact was taken to be the value of $V(x_c)$ and was determined using Eq. (3.75). This voltage was measured for a range of I_{TOT} and the resulting data gave the I-V response of the contact.

Figure 4.6 and Figure 4.7 give the I-V response of various contact structures. As expected, the I-V curves have an exponential response although the slope decreases at higher current because of the effect of R_S of the conducting layer. The slopes are not all the same, indicating differing values of C_S. Different values of ϕ_B also appear to be present since the effective values of J_S are not the same.

Figures 4.8 through 4.13 show the I-V response of some of the samples in Figures 4.6 and 4.7 along with curves fitted using the theoretical equations given in Chapter III. The central position of the I-V curves was taken to give the best fit. At the higher current levels the fit is poorer but at these points the experimental data are probably less exact because of sample heating.

Table 4.5 gives the value of J_S and E' determined from the curve fit. These values, along with data for R_S , x_c , and Z for any particular contact, were used in Eqs. (3.86) and (3.87) to give the theoretical I-V response. Also given are the values of C_S and ϕ_B as calculated using E' and J_S.

The label EST in the emission column means that for this particular combination of C_S and ϕ_B , the emission was out of the strict TFE range and moving into the FE range. These values of C_S and ϕ_B are calculated using the FE equation as an approximation and are therefore estimates. However, the values for C_S and ϕ_B are calculated using the FE equation as an approximation and are therefore estimates. However, the values for C_S should be very close to actual values with the values of ϕ_B being slightly more in error.

The variation in ϕ_B , the reason for the observed ϕ_B being breater than 0.9 eV, and comparison of the C_S values in Table 4.5 with those of Table 4.4 will be discussed in Section V.

4.5 Temperature variation of R_c

Using the probe station mounted on the thermoelectric cooler, as shown in Figure 4.3, transfer length measurements of R_c versus temperature were made. The experimental temperature range was from ~ -10° C to ~ +25° C. The temperature was measured using a copper-constantan thermocouple counted in the prove support plate
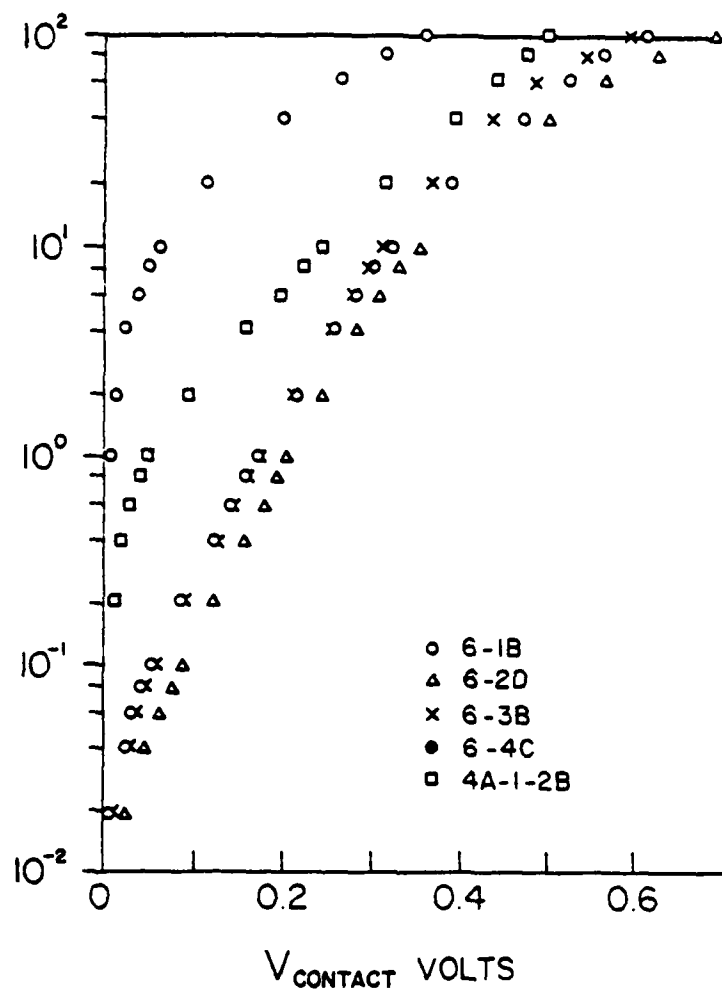
Figure 4.6   I-V response of Au-Sn diffused GaAs contact
structures.   T = 23°C.
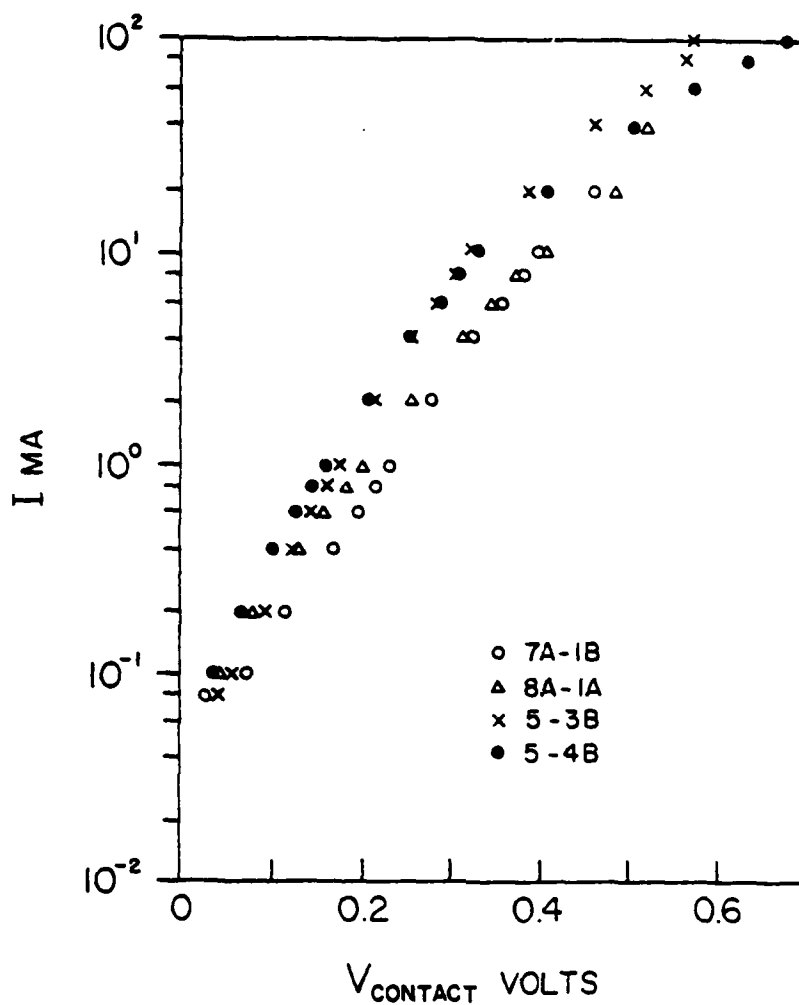
Figure 4.7 I-V response of Au-Sn diffused GaAs contact
structures. T = 23°C.
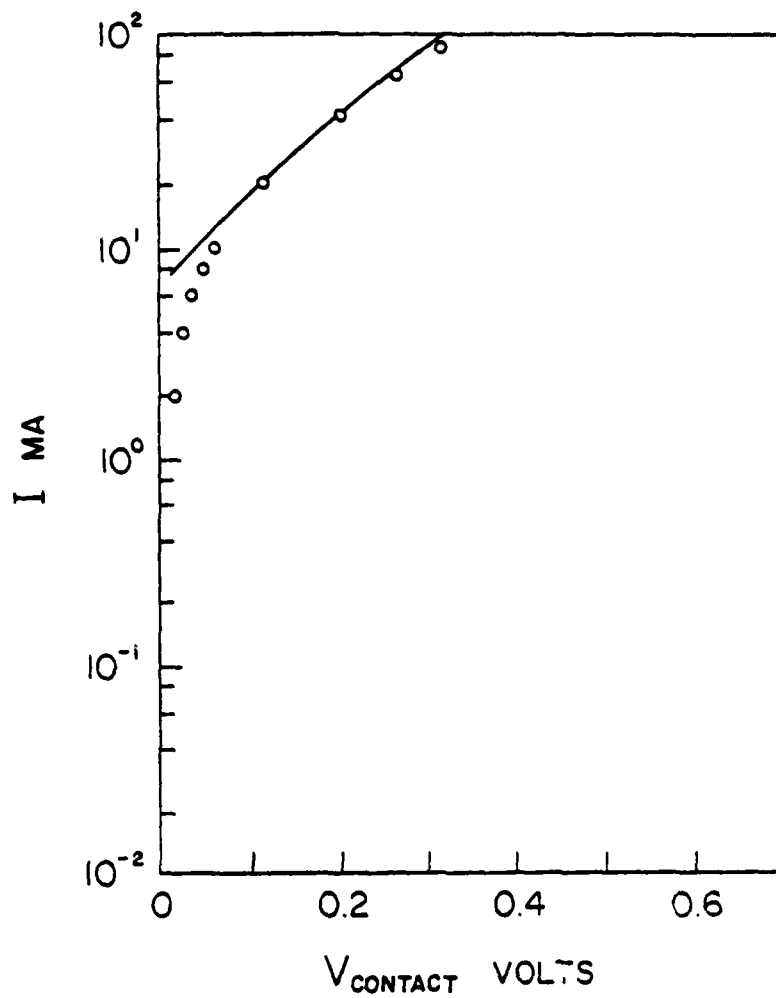
Figure 4.8 I-V response of Au-Sn diffused sample # 6-1B.
T = 23°C. Theoretical FE fit with $\emptyset_B$ = 1.223 eV.
C_S = 1.68 x 10^{19}/cm^3.
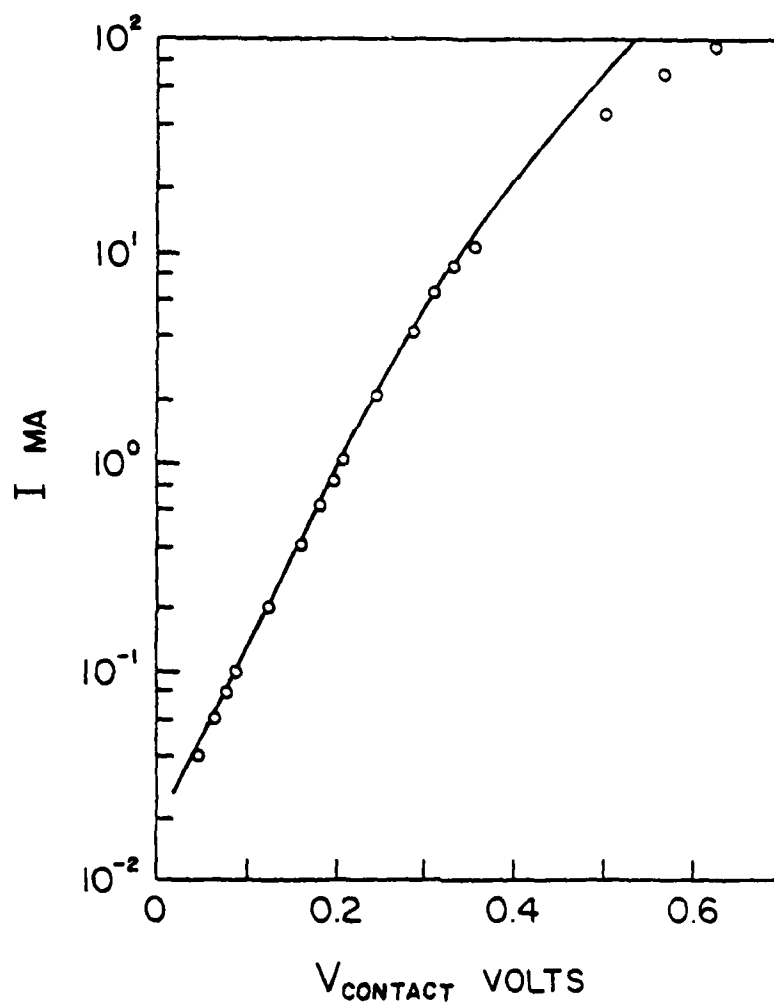
Figure 4.9 I-V response of Au-Sn diffused sample # 6-2D.
T = 23°C. Theoretical TFE fit with $\emptyset_B$ = 1.06 eV.
C_S = 5.45 x 10^{18}/cm^3.
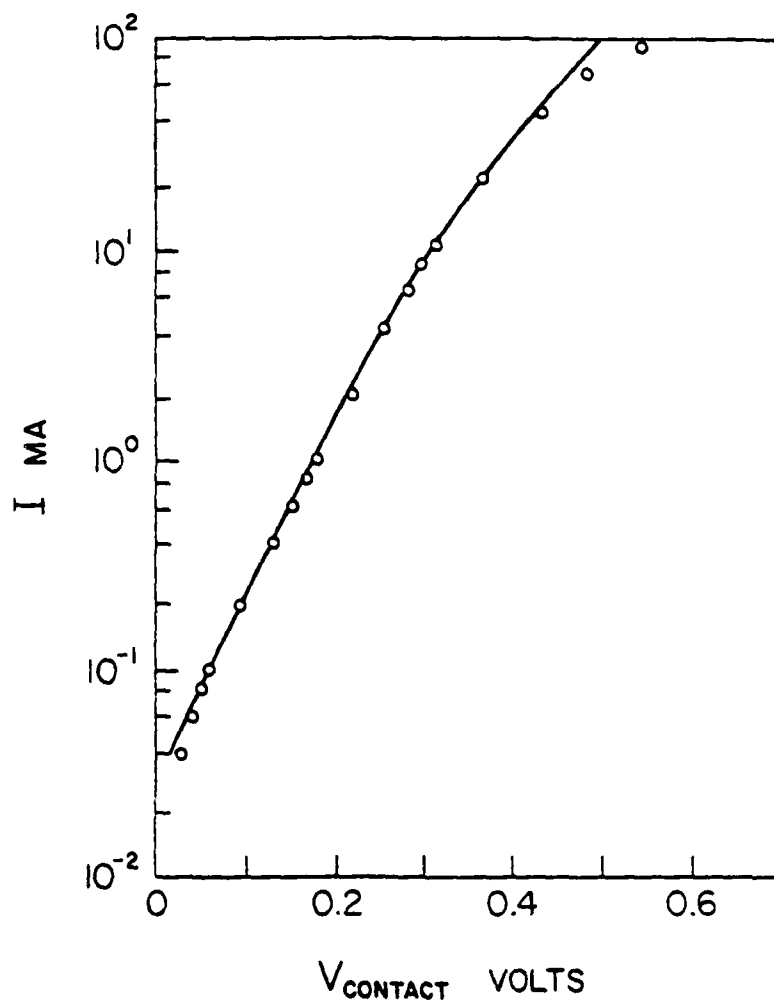
Figure 4.10   I-V response of Au-Sn diffused sample # 6-3B.
T = 23°C.   Theoretical TFE fit with $\emptyset_B$ = 0.975 eV.
C_S = 4.68 x 10^{18}/cm^3.
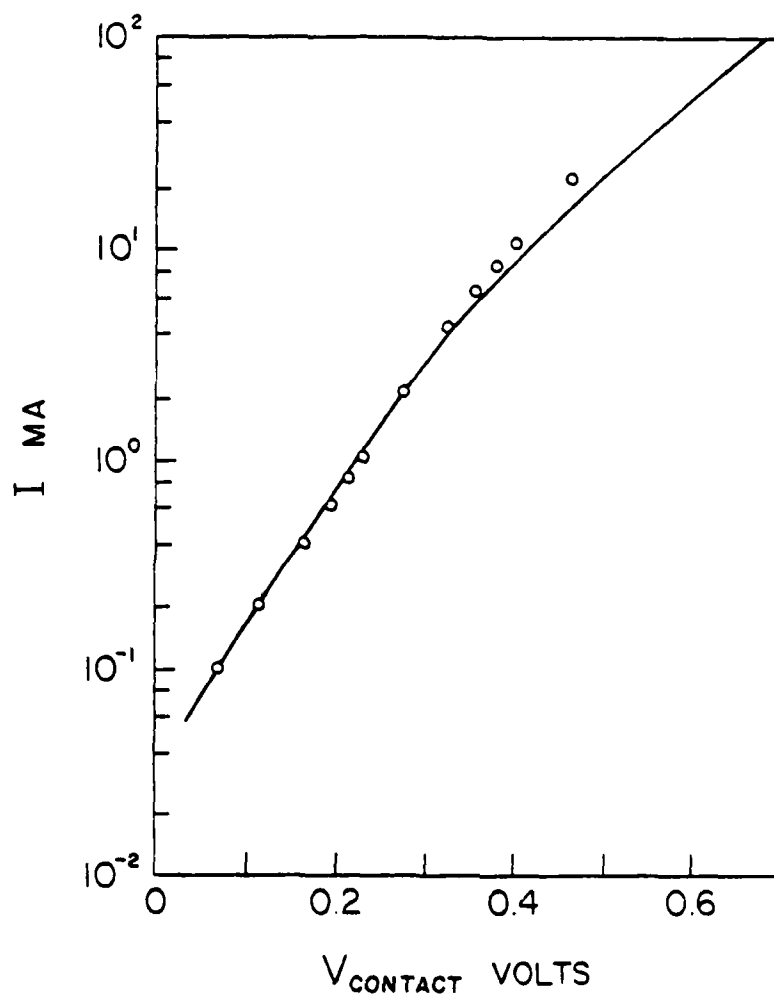
Figure 4.11 I-V response of Au-Sn diffused sample # 7A=1B.
T = 23°C.   Theoretical TFE fit with $\emptyset_B$ = 1.324 eV.
C_S = 9.64 x 10^{18}/cm^3.
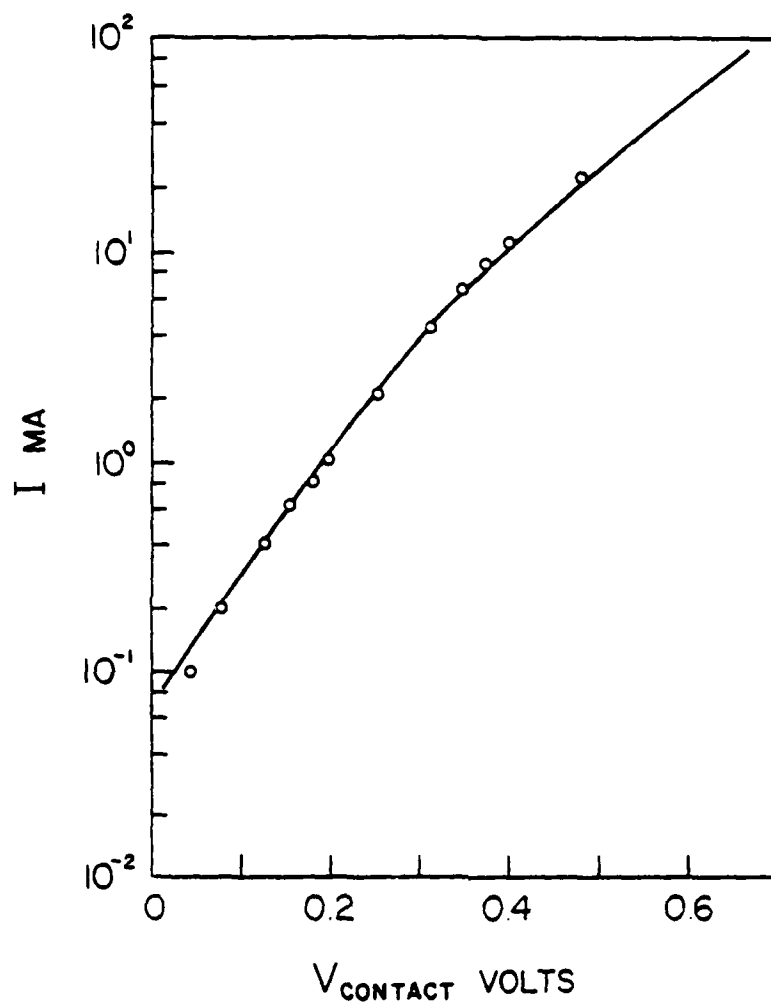
Figure 4.12   I-V response of Au-Sn diffused sample # 8A-1A.
T = 23°C.   Theoretical FE fit with $\emptyset_B$ = 1.417 eV.
C_S = 1.18 x 10^{19}/cm^3.

97
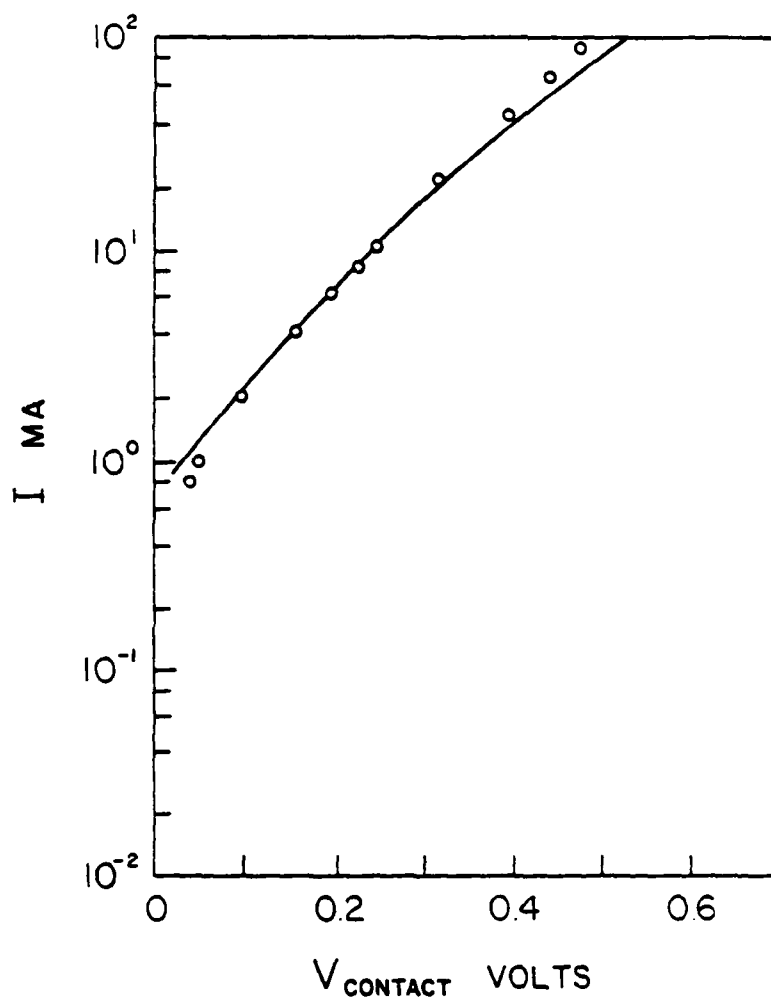
Figure 4.13 I-V response of Au-Sn diffused sample # 4A-1-2B.
T = 23°C. Theoretical FE fit with $\emptyset_B$ = 1.415 eV.
C_S = 1.65 x 10^{19}/cm^3.

directly beneath the sample. The R_C vs. T variation for selected
samples is given in Figure 4.14 to 4.19. The solid lines represent the
theoretical prediction of the R_C vs. T response using the values of C_S
and ϕ_B as given in Table 4.5. The fit is fair and the trends are
clearly indicated. More discussion will be given in Chapter V.

Table 4.5

I-V Response Data and Contact Parameters
Determined by Curve Fitting

Sample #	R_s $\Omega/$	E' eV $\times 10^{-2}$	J_s A/cm^2	C_s /cm^3 $\times 10^{18}$	ϕ_B eV	Type of emission
6-1B	6.05	8.43	1.544	16.7	1.22	EST FE
6-2D	10.52	5.03	3.69×10^{-3}	5.45	1.06	TFE
6-3D	13.95	4.73	5.69×10^{-3}	4.68	0.975	TFE
7A-1b	23.97	6.46	6.87×10^{-3}	9.64	1.32	TFE
8A-1A	24.36	7.063	1.40×10^{-2}	11.8	1.42	EST FE
4A-1-2B	8.25	8.34	1.42×10^{-1}	16.5	1.42	EST FE
5-3B	11.235	5.31	7.68×10^{-3}	6.19	1.079	TFE
5-4B	12.34	6.144	1.62×10^{-2}	8.60	1.20	TFE
6-4C	12.36	5.31	8.21×10^{-3}	6.23	1.08	TFE

For all contacts $Z = x_c = 7.11 \times 10^{-2}$ cm.
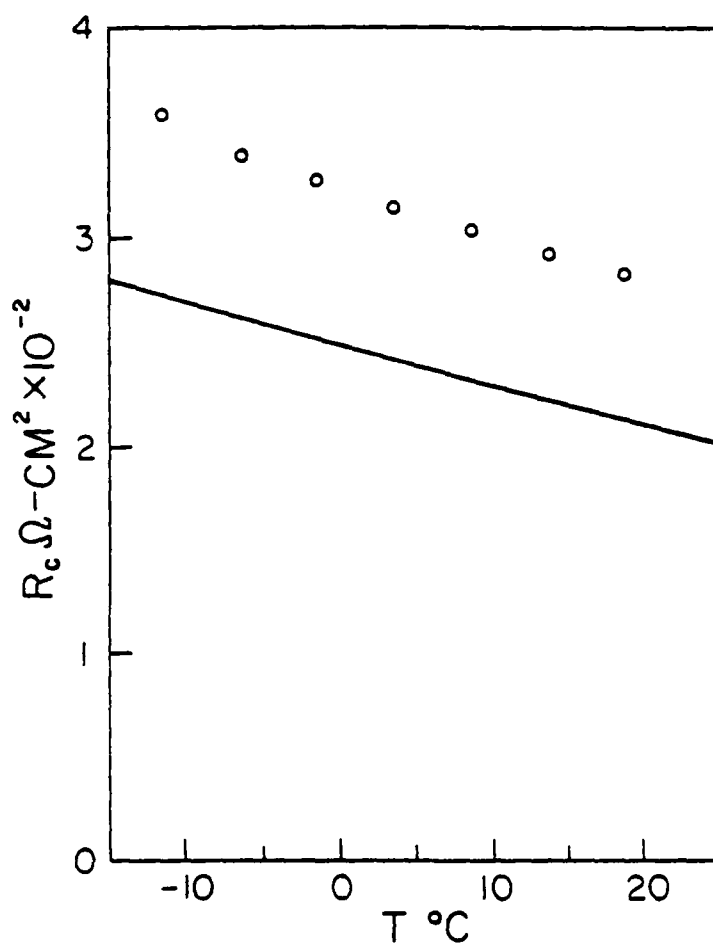
Figure 4.14   Temperature variation of R_c.   Sample # 6-1B.
Theoretical fit parameters same as for Figure 4.8.
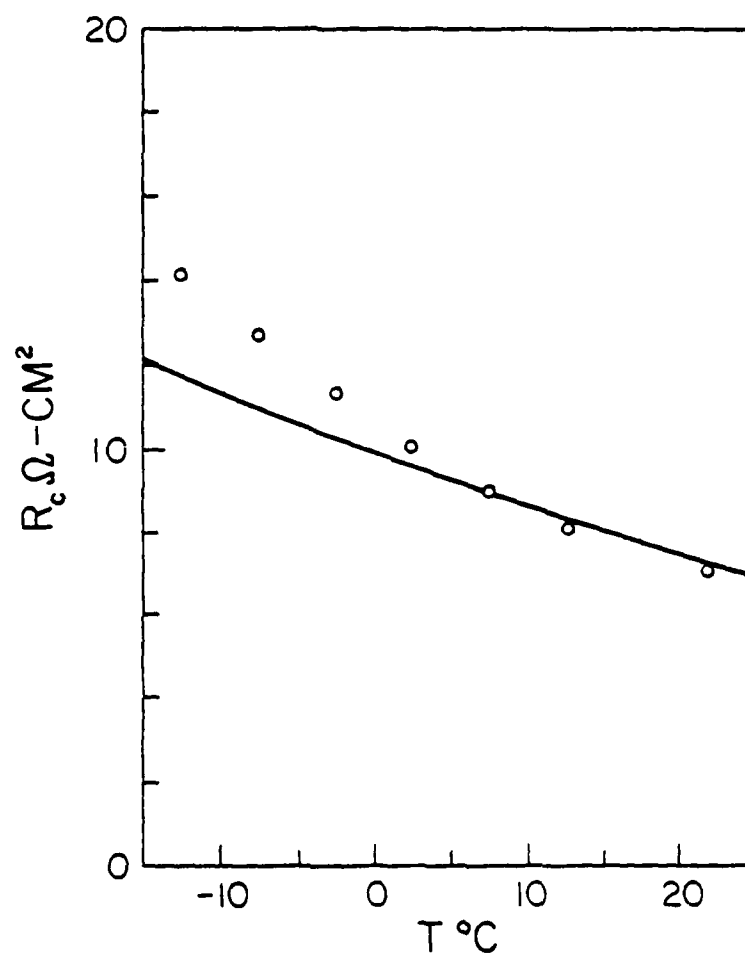
Figure 4.15   Temperature variation of R_c.   Sample # 6-2D.
Theoretical fit parameters same as for
Figure 4.9.
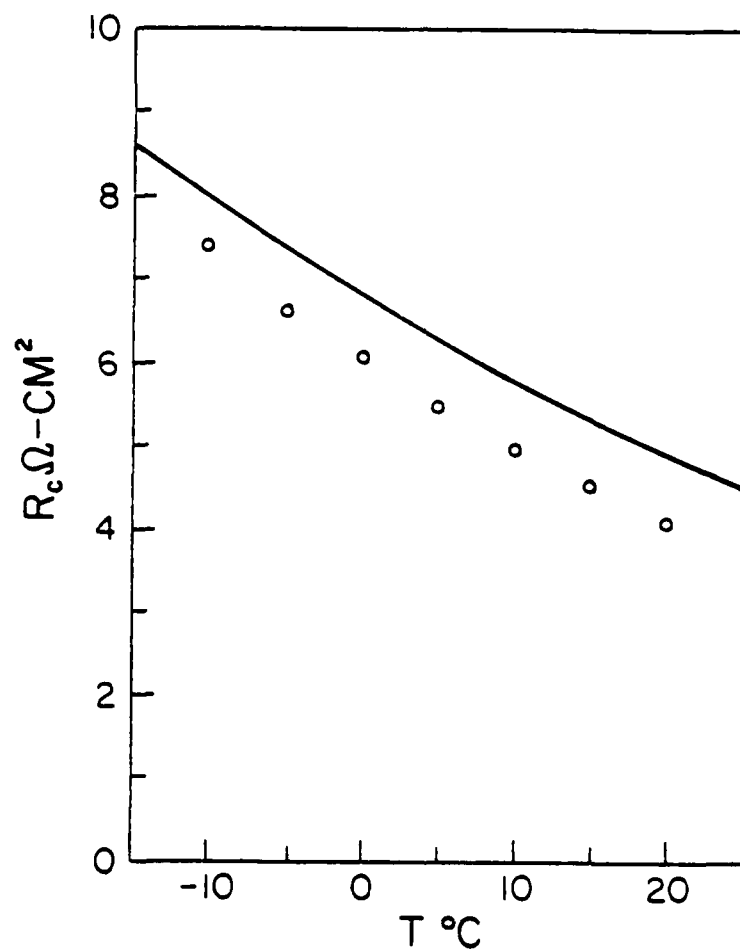
Figure 4.16 Temperature variation of R_c. Sample # 6-3B.
Theoretical fit parameters same as for
Figure 4.10.

103
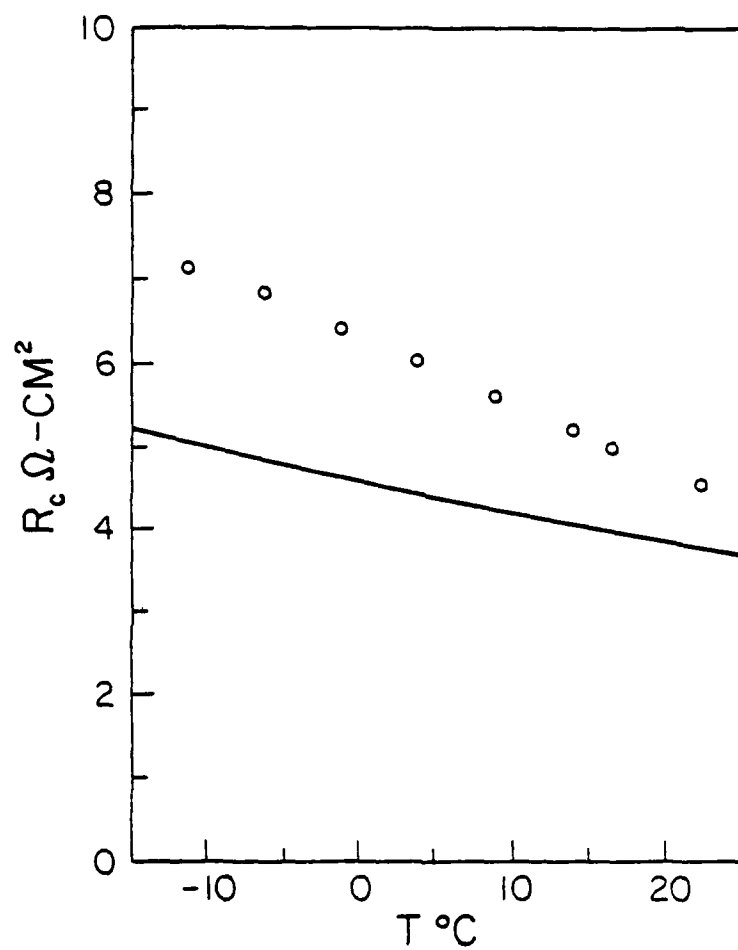
Figure 4.17 Temperature variation of R_c. Sample # 7A-1B.
Theoretical fit parameters same as for
Figure 4.11.
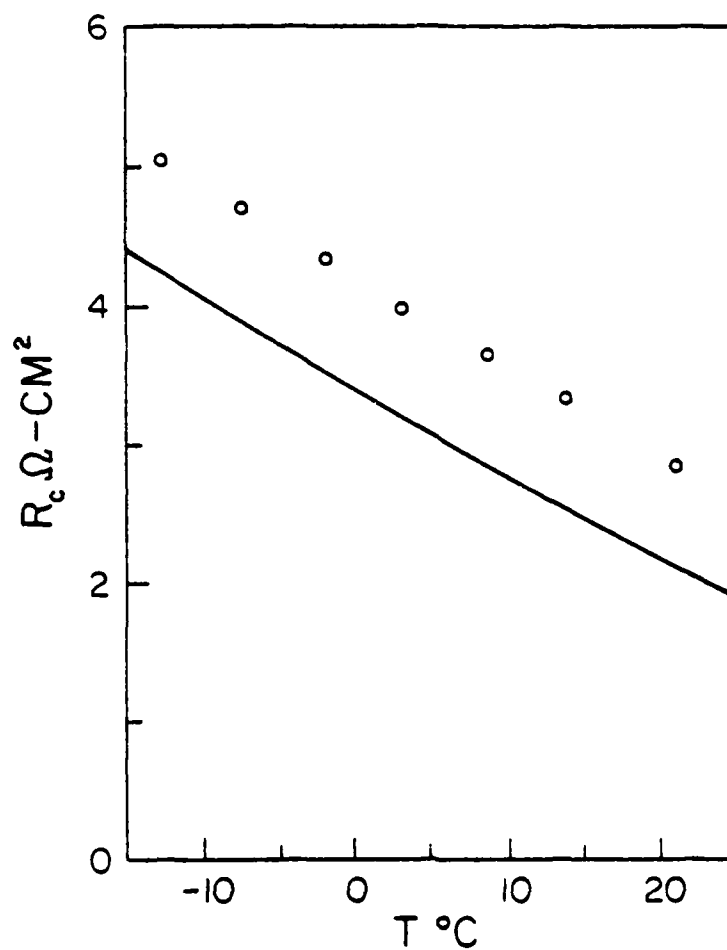
Figure 4.18   Temperature variation of R_c.   Sample # 8A-1A.
Theoretical fit parameters same as for Figure 4.12.

105
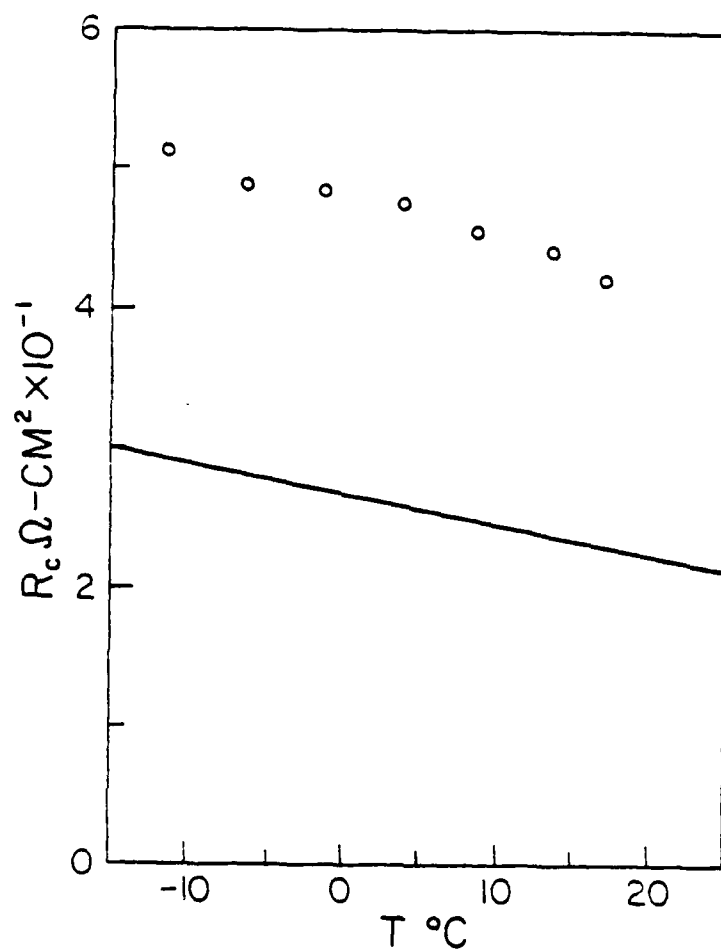
Figure 4.19 Temperature variation of R_c. Sample # 4A-1-2B.
Theoretical fit parameters same as for Figure 4.13.

SECTION V

DISCUSSION

5.1 Contact resistivity and Sn dopant
surface concentration

When this research was initiated, it was felt that experimental measurements of R_C on samples with varying C_S would yield a curve corresponding to a single ϕ_B line in Figure 4.5. This was because previous researchers had found strong evidence of Fermi level pinning in Au-GaAs Schottky barriers resulting in a relatively invariant $\phi_B \approx$ 0.9 eV.

The experimental data for R_C, plotted against the values of C_S determined from $\bar{\rho}$ measurements using Figure 3.3, do not line along a single ϕ_B line. The scatter in data points could be due to two factors. One being that the effective ϕ_B is not pinned and is in fact varying. The other is that the values of C_S as determined from $\bar{\rho}$ data are not accurate.

To resolve this uncertainty, contact I-V response was analyzed and yielded the data of Table 4.5. Immediately apparent from this table is the fact that the values of ϕ_B appear to be varying. They are also somewhat larger than the 0.9 eV usually associated with the Au-GaAs contact. Also evident is the fact that the values of C_S are greater than the values of C_S determined by $\bar{\rho}$ measurements.

For this research the value of C_S is one of the important parameters in contact characterization using the tuneling model. Therefore, various methods, as explained in Section IV, were used to try to determine an accurate value and to provide cross checks of that value. However, as seen by the C_S data in Table 4.4 and Table 4.5, the C_S values calculated using various methods are quite different for the same sample.

To determine which C_S value is the most accurate, it is necessary to consider the manner in which C_S was calculated in each case. The use of Eq. (4.2) with D given by either $D_1 = 2.99 \times 10^{-13}$ $D = 3.056 \times 10^{-14}$, or $D_3 = 9.066 \times 10^{-14}$ cm^2/sec resulted in the widest variation in C_S. This is to be expected, since the value of C_S is quite sensitive to the choice of diffusion coefficient, D.

Since the values of C_s as determined the the $\bar{\rho}$ measurements were in the right range, relative to the I -V data, the values of C_s as calculated using $D = D_1$, or $D = D_2$ appear to be inaccurate. Values of C_s in the $10^{17}/cm^3$ range, as obtained using D_1, are clearly too low to allow appreciable tunneling to take place. Values for C_s of 10^{22} to $10^{23}/cm^3$, as obtained using D_2, seem too high since such values are above the atomic concentration of GaAs. Also the Sn in the dopant film was only on the order of $10^{20}/cm^3$. For these reasons, the use of D_1 and D_2 in determination of C_s is not appropriate.

The C_s values obtained using $D = D_3$ and the values of C_s obtained from $\bar{\rho}$ measurements are in slightly better agreement. Also, a comparison of the C_s values determined from I-V data to those obtained using $D = D_3$ show fair agreement. The values of C_s as determined from the above three methods are plotted in Figure 5.1 against the value of $\bar{\rho}$ as determined from van der Pauw measurements. This value of $\bar{\rho}$ is valid since it was verified during the transfer length measurements. The data are also listed in Table 5.1.

It is evident from Figure 5.1 that the data for C_s from D_3 and that from the I-V measurements appear quite scattered. However, in general the C_s values from the I-V measurements lie above those from the $\bar{\rho}$ measurements and the C_s values from the $D = D_3$ calculation are the highest.

Using only Figure 5.1 it would be impossible to determine which C_s is the most accurate value. Therefore, a measurement of R_c versus temperature was made in order to determine which value of C_s was the most accurate. As seen from the R_c vs. T plot, Figures 4.14 to 4.19, the use of the C_s and ϕ_B values as obtained from the I-V response give acceptable fits. The fit is actually better than it first appears because the change in R_c for a given choice of ϕ_B and C_s is very sensitive and therefore by only a slight change in the values of C_s or ϕ_B used in the calculation, the experimental and calculated points could be made to fit even more closely. The point is that the C_s values as determined from the I-V curve fit do accurately predict the R_c vs. T response, and therefore these C_s values should be considered to be the most accurate.

With this as a basis, the values of C_s as calculated from Eq. (4.2) with $D = D_3$ are too large, meaning that the actual D is not quite equal to D_3. Also the values of C_s as determined by a measurement of $\bar{\rho}$ are too small. However, in order for these conclusions to be valid the question of the scatter in the data, as seen in Figure 5.1, must also be addressed.

The scatter in the C_s vs. $\bar{\rho}$ data may be partly due to inaccuracy in the value of $\bar{\rho}$ against which the C_s data was plotted. The $\bar{\rho}$ values were determined from a van der Pauw measurement as explained in Section III. However, the van der Pauw measurement actually yields a value of

Table 5.1

Values of C_S Determined Using Various Methods of Calculation

Sample #	$\bar{\rho}$ Ω-cm $\times 10^{-3}$	C_S from $\bar{\rho}$-C_S /cm^3 $\times 10^{18}$	C_S from $\bar{D}_3$ /cm^3 $\times 10^{19}$	C_S from I-V /cm^3 $\times 10^{18}$
6-1B	1.16	7.7	8.60	16.8
6-2D	1.77	4.0	2.70	5.45
6-3B	2.33	2.7	2.57	4.68
7A-1B	2.46	2.5	1.81	9.64
8A-1A	3.99	1.4	1.17	11.8
4A-1-2B	1.35	6.5	1.25	16.5
5-3B	2.06	3.2	5.78	6.19
5-4B	2.13	3.0	3.50	8.60
6-4C	1.78	4.0	9.18	6.23
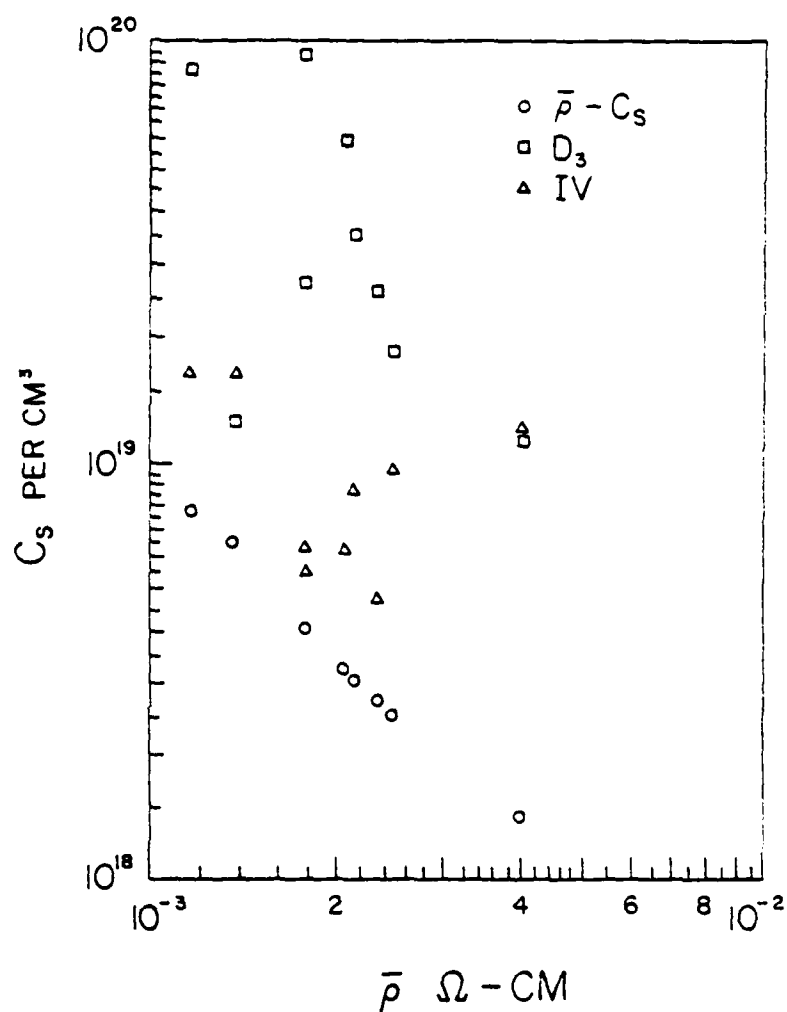
Figure 5.1   Variation of C_s vs. $\bar{\rho}$. C_s determined using various
calculations. $\bar{\rho}$ determined from van der Pauw
measurements.

110

resistivity, R_s , from which $\bar{\rho}$ is calculated if the thickness of the conducting layer is known. Therefore, $\bar{\rho}$ was not determined directly, but rather through:

$$\bar{\rho} = R_s x_j \tag{5.1}$$

where x_j was the layer thickness (junction depth). The measurement of R_s is quite accurate, as was the measurement of x_j using the interferometer. However, in order to delineate the junction a lapping and staining technique was used and some degree of variability is inherent with this step.

Therefore, if the value of x_j was somewhat in error due to inaccurate junction delineation, use of a $\bar{\rho}$ value in determining C_s through Figure 3.3 would result in errors in C_s. From the van der Pauw measurement, an error of 10% in x_j would give an error of 10% in $\bar{\rho}$. Using Figure 3.3, this error of 10% in $\bar{\rho}$ would then give an error of about 10% in C_s.

An error in the value of x_j, or even D_3, greatly affects the value of C_s as calculated using Eq. (4.2) because of the sensitivity of the erfc term. An error of 10% in either x_j or $\sqrt{D_3}$ results in errors in C_s on the order of 80%. Therefore, the scatter in these data points is even greater.

If the data points for samples 7A-1B and 8A-1B are neglected in Figure 5.1, due to probable errors in x_j, the other values show a general trend of decreasing C_s for increasing $\bar{\rho}$. If the curve from Figure 3.3 is shifted up by approximately a factor of two in C_s for all points, then a crude fit is obtained. Given the previously mentioned difficulty in accurate determination of x_j, the scatter around this shifted line appears to be a more reasonable experimental data point scatter.

The set of C_s data points determined from the I-V measurements. taken as being the most accurate and lying consistently above the $\bar{\rho}$-C_s curve and following the same trend, implies that the basis concepts used in the calculation of the $\bar{\rho}$-C_s curve are valid. Therefore, if slight changes were made in the calculation, the $\bar{\rho}$-C_s curve could be shifted upward and be made to correspond well to the experimental data.

One change could lie with the assumption of full ionization. The calculation of the $\bar{\rho}$-C_s curve was based on the assumption that the dopant had an erfc profile and that all donors were ionized. An electrical measurement of $\bar{\rho}$ detects only the free carrier concentration but, under this assumption, the free carriers have the same profile as the dopant atoms and therefore a measurement of $\bar{\rho}$ along with the use of Figure 3.3 will give an accurate value of the dopant concentration, C_s.

For the case of partial ionization, though not as incomplete as that implied by Figure 3.2, the number of free electrons is less than the donor dopant concentration. Therefore, for a given erfc donor atom distribution, the value of $\bar{\rho}$ with partial ionization would be higher. Or alternatively, for a given $\bar{\rho}$ value, the value of C_s must be larger in the case of partial ionization, since not all donors contribute a free electron.

This is exactly what is seen in Figure 5.1. For a given value of $\bar{\rho}$, the value of C_s as determined from I-V data, lies above the value of C_s predicted by the $\bar{\rho}$-C_s curve wherein full ionization was assumed. It should be pointed out that the I-V measurements yield a response based on the characterisitcs of the MS contact space charge region. In this region, all the donors are ionized due to the band bending caused by ϕ_B and therefore the value of C_s calculated from IV data refers to donor atom concentration directly and not just bulk ionized donor concentration.

The fitting of the I-V-C_s data in Figure 5.1 to a $\bar{\rho}$-C_s curve for incomplete ionization would follow a similar calculation to that used to obtain Figure 3.2. The degree of partial ionization would not be the same but would be closer to full ionization since the difference in I-V-C_s values and $\bar{\rho}$-C_s values is only about a factor of two.

One problem with the above argument is that the reasoning applied to reject the use of Figure 3.2 in favor of full ionization applies here also. For high levels of doping impurity band formation and band tailing are highly likely and therefore full ionization is the case. However, an upward shift of the $\bar{\rho}$-C_s curve to fit experimental data can also be realized by a change in the assumption concerning carrier mobility.

The calculation of Figure 3.2 was based on Eq. (3.9) which used a value of electron mobility, μ_n from Sze (9). These values of μ_n for a given carrier concentration N_D were for bulk GaAs samples. In this research the conduction was in an n-type diffused layer instead of bulk material. Therefore, it is possible that Sze's values are somewhat higher than is actually the case. For diffused areas in which a large amount of dopant has been incorporated, as is the case here, the mobility of the electrons is very likely less than that for bulk material due to stress to the lattice incurred during the diffusion. If the actual mobility is less than that represented by Eq. (3.16), then to obtain a given value of $\bar{\rho}$, more electrons, meaning a larger C_s, are needed than for the case of Figure 3.3. The result is to shift the $\bar{\rho}$ -C_s curve upward for all values of $\bar{\rho}$.

However, since the values of I-V-C_s in Figure 5.1 are about a factor of two larger than the values from the $\bar{\rho}$-C_s curve, a mobility decrease by a factor of two is needed to give twice the C_s for a given $\bar{\rho}$. A very rough check can be obtained by comparing the values of

112

average mobility, $\bar{\mu}_H$, and average carrier concentration, $\bar{N}_D$, as listed in Table 4.3, to those from Sze. From Sze's graph, in the range $N_D \approx 2 \times 10^{18}/cm^3$, the mobility is about 2500 cm^2/V-sec. While this is not exactly twice the values of $\bar{\mu}_H$ in Table 4.3, it is significantly larger. Therefore, an upward shift in the $\bar{\rho}-C_s$ curve could be realized by assuming a lower value of mobility for the electrons in the diffused layer. This would account for much of the disagreement between the $\bar{\rho}-C_s$ and $I-V-C_s$ values in Figure 5.1 and would still be within the assumption of full ionization.

If impurity band conduction is occuring due to the high doping levels then it is probable that the electron impurity band mobility is less than the normal conduction band mobility. However, Sze's graph actually takes this into account indirectly since his plot is with respect to actual measured carrier concentrations. The plotted mobilities are experimentally observed values at that particular doping level. The only difference in the case of this research is that diffused layers instead of bulk material are used.

A final check on the validity of the $I-V-C_s$ data and the assumption of full ionization is in relating the $I-V-C_s$ data and x_j to Eq. (4.2). From Figure 5.1 it is evident that the actual diffusion coefficient is not equal to D_3, given by Eq. (4.14), since the C_s values predicted using $D = D_3$ are too large. If the $I-V$ data values of C_s from Table 4.5 are used with values of x_j from Table 4.3 and C_B from Table 4.4, a value of appropriate diffusion coefficient can be calculated using Eq. (4.2). The results of such a calculation are presented in Table 5.2. The diffusion time, t, was taken as 6 hours. The diffusion temperature was 950° C.

From Table 5.2 it is evident that an assumption of full ionization and an erfc dopant profile does give consistent results. The value of diffusion coefficient, $D \approx 1.5 \times 10^{-13} cm^2$/sec, is very similar for all samples. This value of D is slightly larger than $D_3 = 9.066 \times 10^{-14}$ but is in the same range.

The value of D for sample 7A-1B is unusually low, indicating a possibility of error in the measurement of x_j. The values of D for sample 8A-1B and 4A1-2B are close to each other and to D_3 but are lower than for the other samples. This could be due to some dependence of D on substrate doping. The substrate doping for the above two samples was less than for the others by about a factor of two.

In summary, the discussion presented in this section shows that a Sn diffusion in GaAs can be described by an erfc profile with all donor atoms assumed to be fully ionized. Also, a theoretically determined $\bar{\rho}-C_s$ curve, relating layer resistivity to surface concentration, is applicable if a correction for surface effects is made for the values of electron mobility used in the calculation.

113

Table 5.2

Diffusion Coefficient for Sn in GaAs Calculated Using C_S Values

Determined from I-V Measurements

Sample #	x_j Microns	C_B /cm^3 x 10^{17}	C_S / cm^3 x 10^{18}	D cm^2/sec x 10^{-13}
6-1B	1.91	1.97	16.8	1.33
6-2D	1.68	1.97	5.45	1.48
6-3B	1.67	1.97	4.68	1.56
6-4C	1.44	1.97	6.23	1.04
5-3B	1.83	2.0	6.19	1.69
5-4B	1.73	2.0	8.60	1.34
7A-1B	1.02	1.98	9.64	0.45
8A-1B	1.64	1.03	11.8	0.90
4A-1-2B	1.64	1.1	16.6	0.84

5.2 Variation of ϕ_B

Previous research on MS contacts and barrier heights has led to the general conclusion that an Au-GaAs contact barrier is subject to Fermi level pinning with a resultant ϕ_B relativity constant in the range 0.9 to 1.0 eV. The exact mechanism of pinning are not clear but the effect is too make ϕ_B invariant with respect to doping level in semiconductor.

As regards the research presented here, the above implies that the variation of R_C should be due only to a variation in C_S with a fixed ϕ_B = 0.9 eV. The I-V data as given in Table 4.5 indicated that ϕ_B was also varying, although most values were near 1.0 eV. However, use of these unexpectedly larger ϕ_B values in the theoretical equations resulted in good fits to the I-V curves and quite close predictions to the R_C vs. T response. This means that the Schottky barrier model is generally valid in describing contact tunneling properties but requires the use of a somewhat larger value of ϕ_B than usually quoted in the literature.

Since there is very much experimental evidence supporting Fermi level pinning in Au-GaAs barriers, another explanation for the large ϕ_B was sought. The most probable cause is due to the effect of an additional interfacial oxide layer between the Au and the GaAs surface (71). Some researchers have suggested that this oxide may be formed during the contact evaporation step (72). The effect of this additional layer is to reduce the value of the saturation tunneling current, J_S , and therefore to present an effectively higher barrier.

The model for such a structure is shown in Figure 5.2. This model is the one proposed in the Bardeen model to explain Fermi level pinning (38). The actual barrier height in the semiconductor, ϕ_B , can still be subject to pinning as long as the oxide layer is thin enough to allow the metal Fermi level to affect the position of the semiconductor Fermi level and band structure through the difference in work functions. For a barrier thin enough to allow electron tunneling to occur, the above assumption is quite valid.

This means that the effect of any surface states in pinning ϕ_B are still felt and that a ϕ_B = 0.9 eV would be formed. The band bending in the semiconductor and the shape of the Schottky barrier are exactly the same as for a pure MS contact with the same ϕ_B. Therefore, electron tunneling through the space charge region, the Schottky barrier portion of the diagrams, is accurately given by the theoretical equations presented in previous chapters.

The effect of the oxide layer is to present an additional width of insulator, acting as an effectively wider space charge region, in the path of the tunneling electrons. This effective widening of the insulating region acts to reduce the value of contact current at all
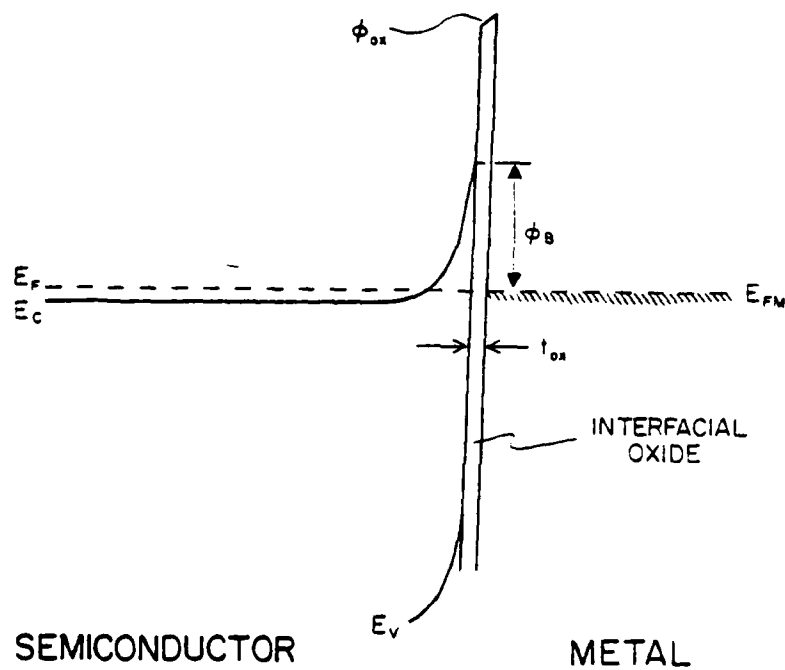
115

Figure 5.2 Model of a MS contact with an interfacial
oxide layer.

116

applied biases. For a contact I-V characteristic which is given by an equation such as Eq. (2.40) or Eq. (2.55), the result is a reduction in the J_S terms. The slope of the I-V response in the exponential region is not affected as long as the barrier is thin enough so that the applied contact bias is taken up mostly across the space charge region and not across the oxide layer. If a small portion of the applied bias is taken up across the oxide, the effect is seen as an increase in the value of E_o or E_∞ in Eqs. (2.40) and (2.55).

The reason that an effective decrease in J_S leads to an apparent increase in ϕ_B may be understood by considering the process by which ϕ_B is obtained from the curve fitting process. In the curve fit, a Schottky barrier model without an interface oxide is assumed. As explained in Chapter II, this gives rise to an I-V response as given by Eq. (2.40) or Eq. (2.55). The parameters of J_S and E_o and E_∞ are then chosen to give a good fit. The value of C_S is determined from the E_∞ term. The J_S term is proportional to various physical constants and also to the value of E_∞ or E_o through an $ex(-\phi_B/E_o)$ term. Therefore, once E_o and J_S have been determined, a value of ϕ_B is chosen to fit the theoretical value of J_S, through Eq. (2.41) or Eq. (2.57), to the experimental value.

If an interfacial oxide layer exists, the physical effect is for the contact to exhibit a value of J_S lower than would be observed with no oxide layer. Since in the Schottky barrier model, a lowering of J_S evidenced by an increase in ϕ_B through the $\exp(-\phi_B/E_o)$ term, an experimentally fit value of J_S lower than expected would result in a value of ϕ_B higher than expected, as observed in Table 4.5.

An estimate of the thickness of the interfacial oxide layer can be obtained by considering the reduction in J_S from that expected for barrier with $\phi_B = 0.9$ eV. If Fermi level pinning results in $\phi_B = 0.9$ eV in the semiconductor portion of the contact then without any oxide layer the tunneling electrons would experience only the $\phi_B = 0.9$ eV Schottky barrier and the value of J_S would be determined by Eqs. (2.41) or (2.57). Since, in the model of Figure 5.2, it is assumed that the semiconductor side still has the above properties, Eqs. (2.41) and (2.57) would still predict accurate values of J_S. However, the total contact J_S would be reduced because the oxide barrier has transparency less than 100%.

For a sample with a given C_S and J_S, the ratio of the measured J_S to that predicted by Eq. (2.41) or (2.57) for $\phi_B = 0.9$ eV with the same C_S gives an indication of the transparency of the interfacial oxide layer. If the WKB approximation is used to calculate the transparency of a rectangular barrier as in Figure 5.2, an estimate of oxide thickness can be obtained.

For example, using data from Sample 6-1B, the curve fit yielded:

117

$$C_S = 1.68 \times 10^{19}/cm^3$$

$$\varphi_B = 1.22 \text{ eV}$$

$$E_\infty = 8.43 \times 10^{-2} \text{ eV}$$

$$J_S = 1.544 \text{ A/cm}^2$$

under Fe at $T = 23°$ C. Using the above C_S and $\phi_B = 0.9$ eV, the theoretical J_S as calculated using Eq. (2.41) is

$$J_S = 64.31 \text{ A/cm}^2$$

Therefore, the ratio of the objserved J_S, with the assumed interfacial oxide, to the value of J_S for no oxide and $\phi_B = 0.9$ eV is:

$$\text{Ratio} = \frac{1.544}{64.31} = 2.4 \times 10^{-2} \tag{5.2}$$

This should equal the transparency of the oxide layer at the interface.

From a WKB approximation, the transparency of a rectangular barrier of height $V(x)$ is given by (63):

$$T = \exp \left\{ -2(\frac{2m^*}{h^2})^{1/2} \int_{x1}^{x2} [V(x)-E]^{1/2} dx \right\} \tag{5.3}$$

where x_1 and x_2 are the points where $V(x) = E$. For this case $E = n_F = $ Fermi level is te=aken as the reference energy. For a constant oxide barrier height measured with respect to the Fermi level, $V(x) - E = q\phi_{ox}$, the integral becomes:

$$\int_{x1}^{x2} [V(x)-E]^{1/2} dx = q^{1/2} \phi_{ox}^{1/2} t_{ox} \tag{5.4}$$

where $t_{ox} = x_2-x_1$ is the width of the oxide layer. Substituting Eq. (5.4) into Eq. (5.3) and equating this to Eq. (5.2) gives the result:

$$\phi_{ox}^{1/2} t_{ox} = 1.379 \times 10^{-9} \text{ (ev)}^{1/2} \text{ m} \tag{5.5}$$

Therefore, if an approximation of $\phi_{ox} \approx 2$ eV is used:

$$t_{ox} = 9.75 \text{ Å}$$

or the oxide thickness is only on the order of 10 Å or about two mono-layers. For other estimates of ϕ_{ox} in Eq. (5.5) the value of t_{ox} will

118

change but the order of magnitude of t_{ox} is still only a few mono-layers.

It is very likely that an oxide of this thickness could form on the surface during contact processing before the metal evaporation. Therefore, the observance of ϕ_B values slightly greater than 0.9 is probably due to the presence of a thin interfacial layer that originated from an oxide.

The application of the simple Schottky barrier model, with the increased ϕ_B, to the prediction of R_c vs. T is thus reasonable. It must be remembered that the values of R_c are measured near zero bias and therefore the electrons are tunneling through a nearly unperturbed barrier at energies about 0.9 eV from the top of the barrier. This tunneling is affected mostly by the thickness of the barrier and not by its shape. Therefore, an ideal Schottky barrier with increased ϕ_B or a two piece barrier as shown in Figure 5.2, with the same effective tunneling width, should give very similar results. As seen in the plots of R_c vs. T, the use of an increased ϕ_B in the standard Schottky barrier model, although not absolutely physically accurate, can still give quite good predictions of contact performance since the increased ϕ_B does, to first order, account for the additional tunneling barrier thickness.

5.3 General applicability of the Schottky barrier tunneling model

From the fair curve fits obtained to experimental I-V data, it is apparent that the use of the Schottky barrier model and the resulting I-V equations for FE and TFE type tunneling can characterize contact behavior sufficiently accurately for contact modeling. The use of the model is further supported by the fact that the parameters obtained from the I-V curve fit, C_S and ϕ_B , can adequately predict contact resistivity with respect to another independent variable, temperature, as seen in the plots for R_c vs. T.

The variables C_S and ϕ_B , as calculated from the use of the model, can be considered to be accurate since they could be verified by other measurements. The values of C_S were verified by a calculation of C_S based upon resistivity measurements on the diffused layer. However, as explained before, it was necessary that some additional consideration be given to the estimation of carrier mobility in developing the $\bar{\rho}$ -C_S curve. The values of ϕ_B were verified from the data of other researchers wherein ϕ_B ≈ 0.9 eV was given as an expected value. Values of ϕ_B obtained from the curve fit data in this research were somewhat greater than 0.9 eV but, as was explained in section 5.2, the discrepancy arose from the presence of thin interfacial oxides and the manner in which ϕ_B was obtained from the curve fitting process.

119

This model then implies that to obtain non-alloyed, Au-GaAs contacts with "ohmic" properties, i.e., R_c in the 10^{-6} Ω-cm^2 range, FE type tunneling must be present. This then puts very specific requirements on the values of ϕ_B and C_s which would be necessary. If an actual ϕ_B of 0.9 eV could be realized, meaning necessary care in processing to eliminate any interfacial oxides or insulating layers, then values of C_s in the 10^{20}/cm^3 range are required. This has further implication for the type of processing steps which would be required to obtain this level of C_s.

5.4 Contact resistivity of Au-Sn doped GaAs contacts

For the non-annealed Au-Sn doped GaAs contacts studied in this research, the minimum value of R_c obtained was in the 10^- Ω-cm^2 range. When the contacts were analyzed using the Schottky barrier model, the main limiting factor preventing the realization of lower R_c's was the apparent limitation in C_s. Incorporating Sn into the GaAs surface by diffusion produces a maximum C_s of only on the order of $1 \sim 2 \times 10^{19}$/ cm^2. This means that even if the surface oxides which gave an apparent $\phi_B \approx 1.2$ eV had been removed, allowing a larger J_s and the more normal $\phi_B \approx 0.9$ eV to be realized, the value of R_c would still be only in the 10^{-3} - 10^{-4} Ω/cm^2 range. This is nearly two orders of magnitude larger than the values of R_c reportedly being obtained for various alloying methods.

Solid solubility data for Sn in GaAs are not readily available but other researchers (17, 44) give values of maximum C_s for Sn diffused layers in the high 10^{18}/cm^3 low 10^{19}/cm^3 range. If this represents the maximum C_s due to a solid solubility limit, then R_c values lower than the 10^{-2} Ω/cm^2 observed here are not possible using Sn diffusion. Other possible dopant materials will also be under solid solubility restrictions and if they result in only $\approx 10^{19}$/cm^3 values for C_s then their use will also not result in lower values for R_c.

The above considerations mean that if a non-alloyed contact is desired, then a method to dope the GaAs surface to $C_s \approx 10^{20}$/cm^3 is necessary to get $R_c \approx 10^{-6}$ Ω-cm^2. It appears that a predeposition type of diffusion of dopant is unsuitable since solid solubility effects are likely to limit C_s to less than the 10^{20} range.

Some very recent research (30) has produced low R_c (10^{-6} Ω-cm^2 range) contacts using an initial diffusion of Sn but including a subsequent laser treatment of the diffused surface before application of the contact metal. Most likely, the laser treatment results in a localized melting-regrowth condition on the surface and under such conditions dopant segregation during regrowth occurs. For Sn in a GaAs melt, the Sn collects in the melt during regrowth and since the surface would be last to solidify, the Sn would be collected at the surface and result in the large C_s needed for low values of R_c. Another possibility is that the laser treatment allows tin atoms to go from interstitial to substitutional sites.

120

One problem with creating a surface with $C_s \approx 10^{20}/cm^3$ is that the dopant concentration is becoming an appreciable percentage of the semiconductor material. This can result in large changes in band structure and semiconductor properties in general. The modeling of the MS contact would become extremely difficult in such cases and little could be quantitatively explained about contact performance other than that it exhibited a low value of R_c.

Alloying a contact metal into a GaAs surface to create a low R_c contact is also presumed to work according to some type of dopant redistribution and regrowth. The problem is that trying to fit the FE or TFE model to such contacts is difficult when the fabricated R_c is very low. For such cases the expected exponential variation of I and V is seen only for I values larger than those appropriate for useful experimentation and therefore effective values of ϕ_B and C_s cannot be determined. Also, without suitable knowledge of ϕ_B and C_s, tunneling, if it occurs, cannot be characterized.

In summary, the verification of the FE and TFE Schottky model implies that:

1. For non-alloyed MS contacts with large C_s, TFE or FE tunneling is responsible for the low R_c values and "ohmic" behavior and contact performance can be predicted using the appropriate tunneling equations.

2. To obtain extremely low R_c values (10^{-6} Ω-cm^2 range) for non-alloyed contacts, C_s must be very large, in the $10^{20}/cm^3$ range, and such a value is not likely to be attained by a diffusion type of process. Therefore, another type of doping process, perhaps such as ion implantation or subsequent heat treatments of the surface, along with their inherent complications, must be utilized.

3. The processing involved in making non-alloyed contacts is critical in regard to the surface preparation of the semiconductor just before the application of the metal. Interfacial oxides can adequately be modeled by an increase in apparent ϕ_B and if present the increased ϕ_B results in increased values of R_c and poor contact properties.

BLANK PAGE

SECTION VI

APPLICATION OF THE SCHOTTKY MODEL

TO ANNEALED CONTACTS

6.1 Au-Sn diffused layer annealed contacts

Having shown in the previous section that the Schottky barrier model and the associated FE and TFE tunneling equations can adequately characterize non-annealed (non-alloyed) contacts, the model was then applied to attempt to analyze annealed structures. Selected samples of the Au-Sn diffused GaAs contact structures were given sequential annealings in flowing N_2 at temperatures to 425° C. The annealing step was performed for 5 minutes at each temperature.

After each anneal, I-V curves were taken in the same manner as previously explained. Figures 6.1, 6.2, and 6.3 show the results of the I-V tests. From the figures it is apparent that the curves have an overall exponential shape but bend over due to the effect of R_S of the conducting layer, which doesn't change with annealing. The effect of the successively higher temperature anneals is to push the I-V curves upward.

When the theoretical equations for TFE or FE tunneling were applied and curve fitted to the experimental data, values of ϕ_B and C_S were determined for each of the contact I-V curves. Figure 6.4 gives the variation with annealing temperature of ϕ_B, as obtained from the curve fits. Figure 6.5 gives the variation with annealing temperature of C_S.

One apparent fact is that for T up to 275° C or 300° C both ϕ_B and C_S are seen to decrease with successive anneals. The values of ϕ_B move nearer to the value of 0.9 ~ 1.0 eV normally associated with a Au-GaAs Schottky barrier. The values of C_S also move closer to the value of C_S determined from $\bar{\rho}$ measurements.

This decrease can easily be related to a reduction in the thickness of the interfacial oxide. As mentioned before, the presence of an interfacial oxide on the order of 10 to 20 Å was suspected as resulting in apparent experimental values of $\phi_B > 0.9$ eV. The thinning of this oxide layer with successive anneals, due to Au migration or other effects, results in an increase in J_S since this additional

Figure 6.1 I-V response of Au-Sn diffused sample # 5-3B
after successive anneals. T = 23°C.

124
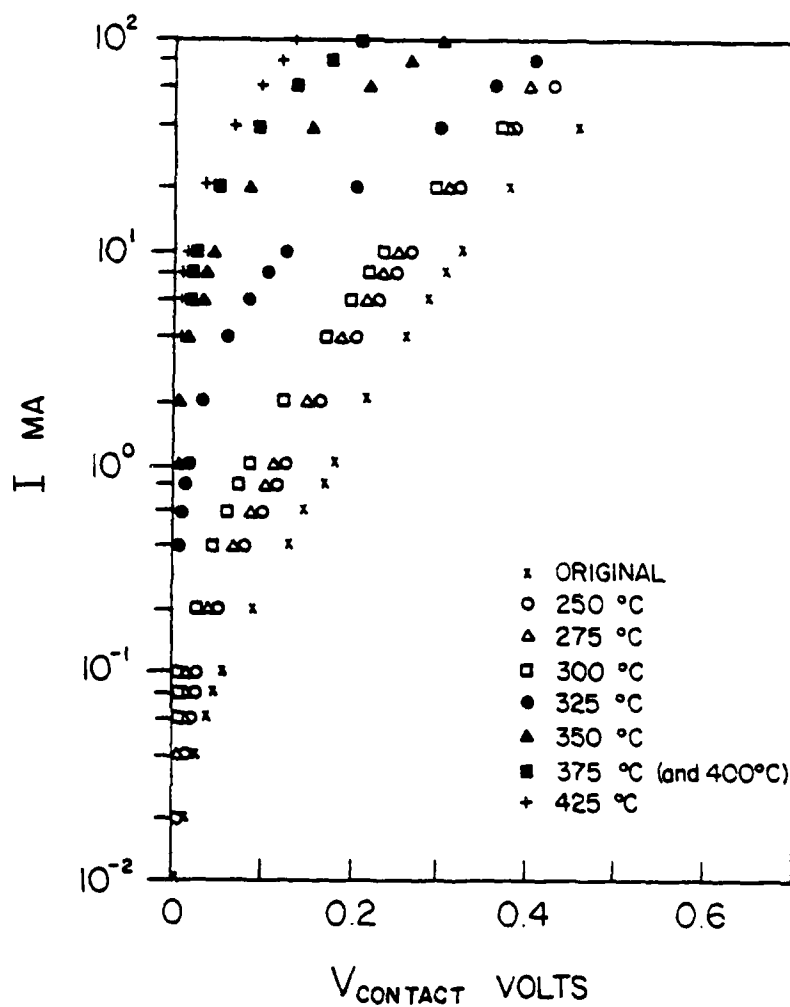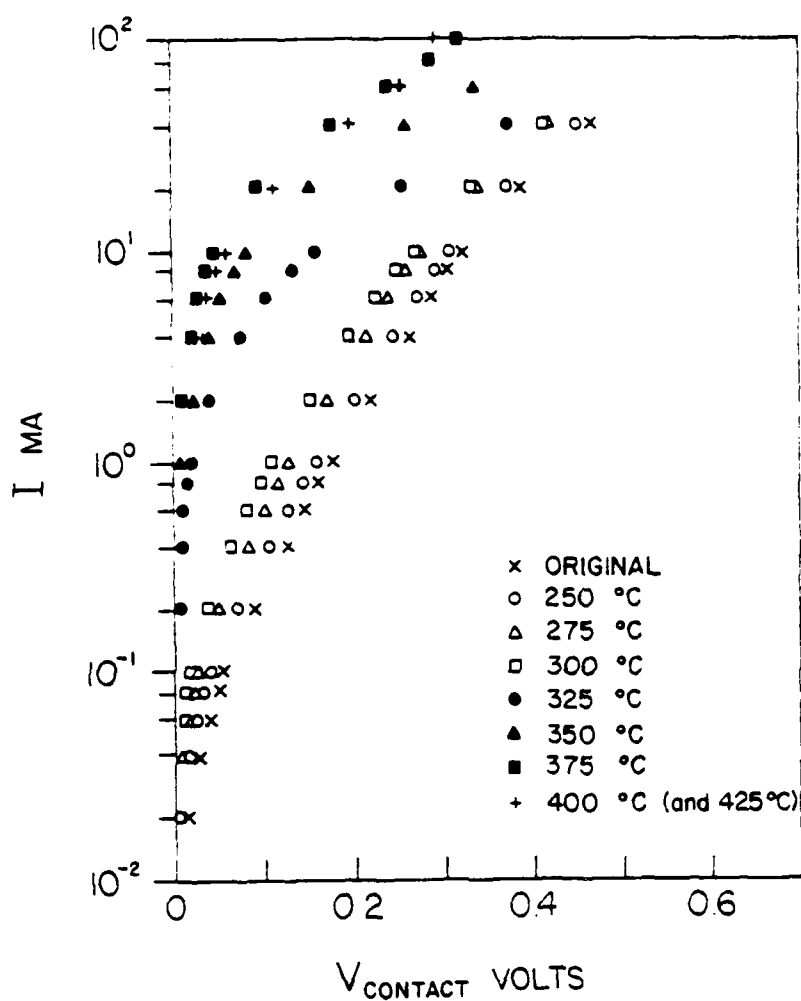
Figure 6.2 I-V response of Au-Sn diffused sample # 6-4C
after successive anneals. T = 23°C.
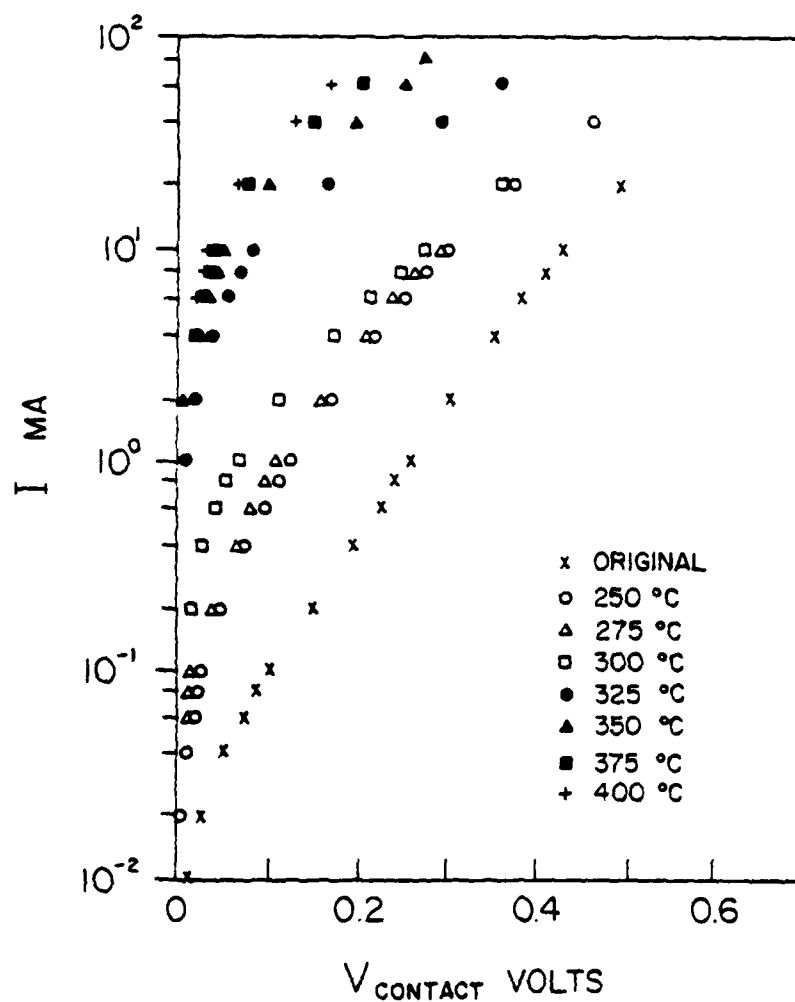
Figure 6.3   I-V response of Au-Sn diffused sample # 7A-1C
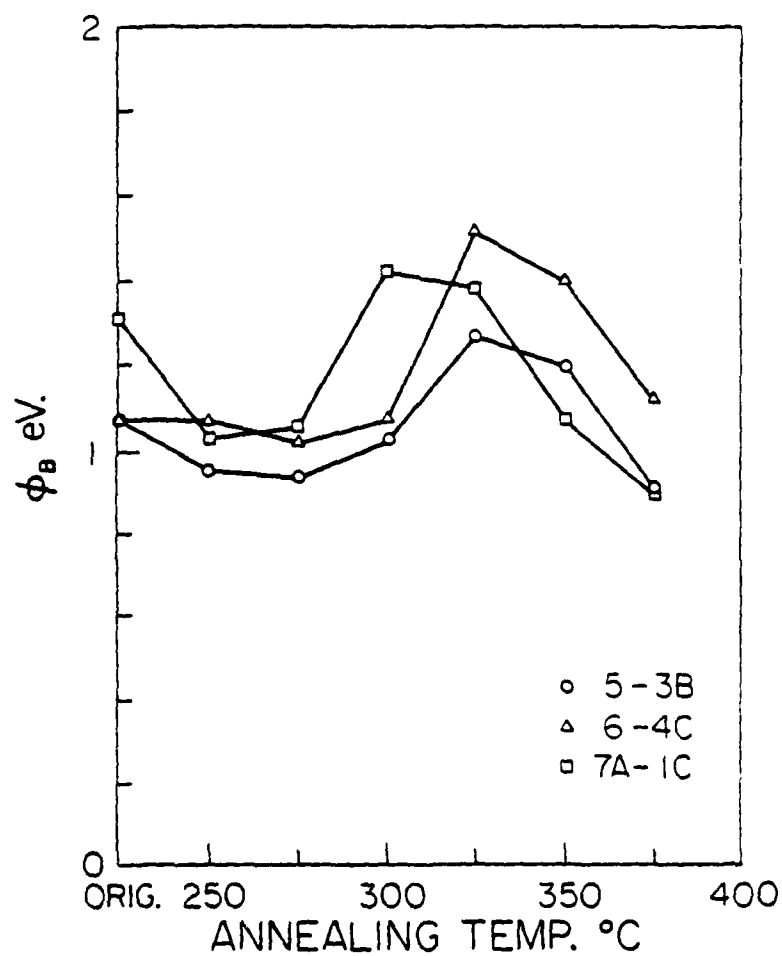after successive anneals.   T = 23°C.

126

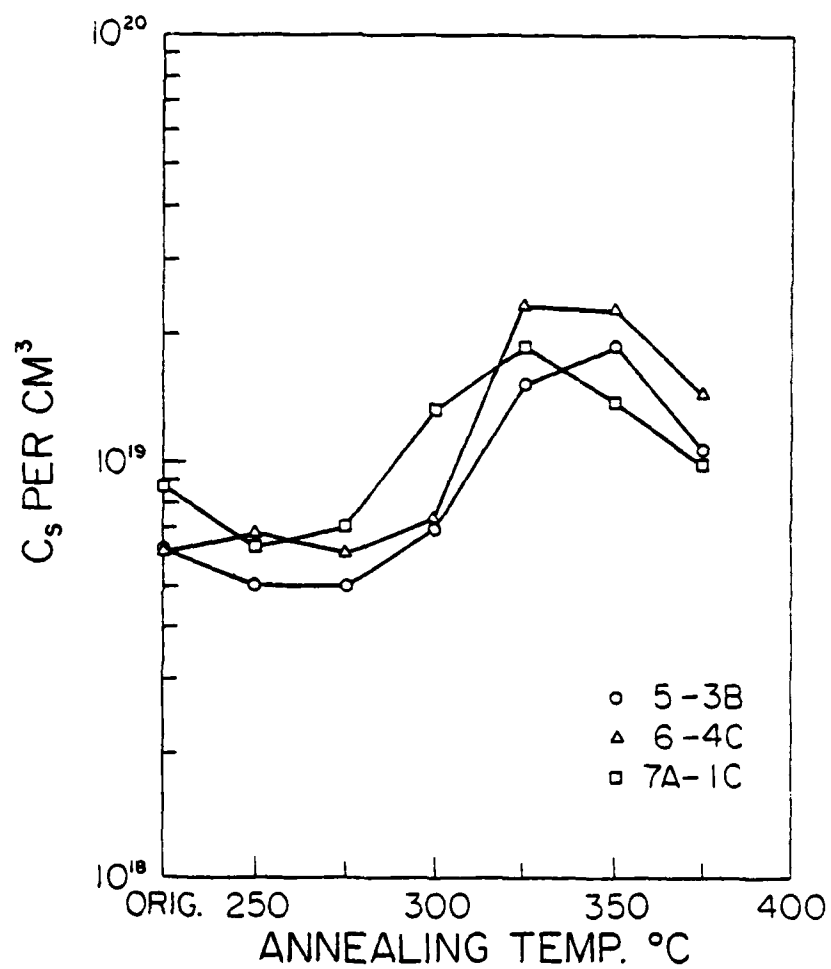Figure 6.4 Variation of ϕ_B for Au-Sn diffused samples after successive anneals.

Figure 6.5 Variation of C_s for Au-Sn diffused samples after successive anneals.

tunneling barrier is decreased. An increase in J_S is reflected in the analysis as a decrease in ϕ_B.

The decrease in apparent value of C_S is also due to a thinning of the oxide layer. With a thinner oxide layer, less of the applied contact bias is dropped across the oxide. Therefore, more of the applied bias appears across the space charge region and gives rise to an increase in current. The slope of the exponential region, $\frac{1}{E'}$, is proportional to $\frac{1}{C_S}$. With the effects of an increased IR drop in the conducting layer taken into account, it is seen that as T increases, the value of E' decreases which implies a decrease in the apparent C_S.

Past the 300° C point, ϕ_B and especially C_S exhibit erratic behavior. The value of ϕ_B increases again and C_S becomes very large. This is clearly opposite to the trend up to this point. It is felt that this behavior is due to the non-uniform formation of contact pinholes.

A contact pinhole is considered to be a small area in which the interfacial oxide has been essentially reduced to zero. At this point, a near ideal MS contact is made. The ϕ_B for such points should be near 0.9 eV. The result is that this point is a much better conducting point for current flow and the current applied to the contact is there-fore concentrated at this pinhole point.

The increase in conductivity at these points results in a large increase in J_S. However, the localization of the current into a single entry point into the conducting surface layer radically alters the model of the contact structure. The effect is to insert a large additional resistance, due to R_S, into the path of current flowing from the pinhole to the x = 0 contact edge. The increase in current path resistance flattens out the exponential portion of the I-V curve due to the additional IR_S drop. Since the curve fitting procedure is based on a normally distributed R_S and uniform contact conduction, the flattened curve is interpreted as an increase in E' and therefore an increase in C_S.

The increase in ϕ_B is related to the increase in C_S since ϕ_B is obtained by a calculation involving the experimental J_S and an $\exp(-\phi_B/E\circ)$ term. If J_S increases then ϕ_B should decrease, but since an effectively higher C_S was used in the calculation, an effective increase in ϕ_B is obtained as the result.

The point is that if the Schottky model is used in determining ϕ_B and C_S when contact conduction is non-uniform, misleading informa-tion results. However, the presence of some type of interfacial oxide was confirmed and the implied trend is that with ideal processing this interfacial oxide could be reduced to zero uniformly across the con-tact. The contact would then exhibit properties related to conditions near $\phi_B \approx 0.9$ eV with C_S near the value determined by ρ measurements.

One important consideration for the above is that the annealing must not proceed so far as to drastically change the essentially non-alloyed, abrupt, nature of the MS interface. It was found that for T > 423° C, significant melting and balling up of the Au occurred. Presumably this would also affect the nature of the interface other than by merely thinning the interfacial oxide to zero. The end result of such high temperature treatment is usually more highly conducting contacts with higher J_S and lower R_C but the mechanism responsible for the better properties would not be a simple reduction in the ϕ_B of a standard tunneling Schottky barrier. Furthermore, at temperatures above 400° C substantial atomic migration and departure from stoichiometry occurs (26).

The effect of increasing the annealing period at each temperature was also examined for one sample, #5-4D. In this case the contacts were annealed at 250° C for increasing periods and then at 300° C for increasing periods. Figure 6.6 shows the I-V response of the contact after the various annealing temperature and times. The maximum temperature was limited to 300° C to avoid the previously mentioned problem with possible pinholes.

Curve fitting of the theoretical TFE equations was done and the results are summarized below, and also presented in Figures 6.7 and 6.8.

1. At a given temperature, subsequent anneals result in an upward shift of the I-V curve, in the same manner as the higher temperature anneals used in the previous experiment. Eventually the contact seemed to stabilize to a final C_S, ϕ_B combination for a given temperature.

2. At 300°c, C_S and ϕ_B appear to increase from the 250° C data due to the probable contact nonuniformity problems mentioned earlier. However, further heat treatment at the same temperature seems to stabilize the change in C_S and ϕ_B but both values at 300° C are higher than at 250° C.

The implication of the above is that the reduction in the interfacial oxide can be partially accomplished by longer annealing times at lower temperatures. However, it appears that the effective elimination of the oxide depends on physical changes related to the magnitude of the annealing temperature and not just to the annealing time.

6.2 Au-Ge-GaAs annealed contacts

The previous contact model and associated FE and TFE equations were also used to attempt to analyze the behavior of Au-Ge-GaAs contacts after successive annealing-alloying steps. An Au-Ge combination is the most widely used material for the formation of a low
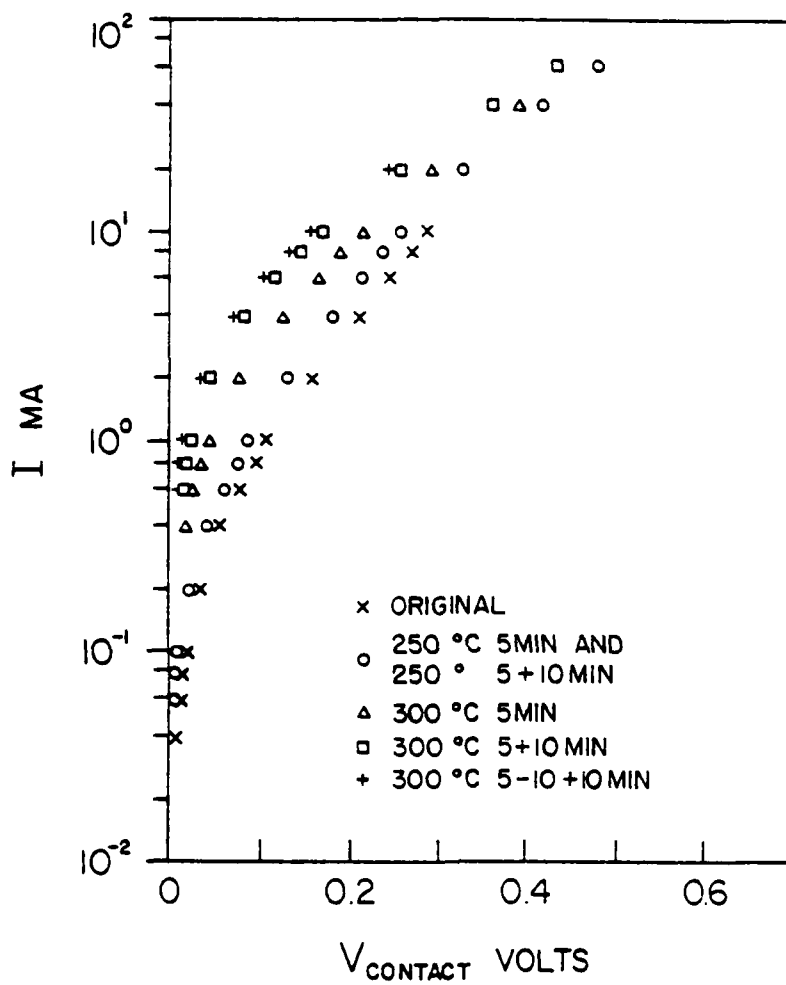
130

Figure 6.6 I-V response of Au-Sn diffused sample # 5-4D
after successive anneals at the same temperature
but for increasing times. T = 23°C.

131

R_C contact to n-type GaAs using the alloying method. In such a method a contact structure is delineated on the GaAs using an Au-Ge eutectic alloy or a Au-Ge-GaAs layer sandwich and heated above the eutectic point in an annealing furnace or with a laser. The Ge is believed to go into the surface forming a highly doped layer which results in tuneling and a low R_C.

For this experiment, n-type bulk GaAs substrates with the following specifications were used.

Si doped

$\bar{\rho} \approx 2.6 \times 10^{-3}$ Ω-cm

$C_B \approx 9 \times 10^{17}/cm^3$

thickness   15 mils

To make the Au-Ge contact a method similar to Anderson, et.al. (21) was used. On a cleaned wafer, a few hundred angstrom layer of Ge was evaporated and over this a layer of Au was evaporated. This differs from Anderson's method where the evaporated Ge layer was first formed into a crystalline epi layer by substrate heating prior to the Au evaporation. After the contact structure was delineated using a photoresist lift-off technique, individual strucutres were scribed apart and given successive anneals and tested.

The resulting I-V curves from selected samples are shown in Figures 6.9, 6.10, and 6.11. The curve fitting of the theoretical FE and TFE equations to this data is much simpler than previously since the IR_S drop in the conducting substrate is negligible since R_S is very small being ≈ 0.607 Ω/square. Therefore, the exponential portion can be directly fitted to a straight line of slope $1/E'$, and current squeezing effects in the contact are not important. For the As deposited unannealed curves, the I-V response bends over slightly due to the effect of the GeLayer acting as a slight additional series resistance. For these, a fit was made to the lower current portion of the curve where IR drops are negligible.

Similar to the annealed contacts discussed in Section 6.1, these contacts have I-V curves which shift generally upward with increasing annealing-alloying. However, in many cases the I-V curve shape is not strictly exponenial implying that alloying is modifying the interface characteristics so that perhaps a simple Schottky barrier cannot accurately characterize its performance. Curve fitting to these curves was done on the lower portion of the I-V curve above the knee. In all cases, since the curves shift upward, higher values of J_S are implied and since R_C is roughly proportional to $1/J_S$ increased alloying gives lower values for R_C.

The I-V data was curve fit and analyzed to give values of ϕ_B and C_S which are plotted in Figures 6.12 and 6.13. The ϕ_B and C_S data for
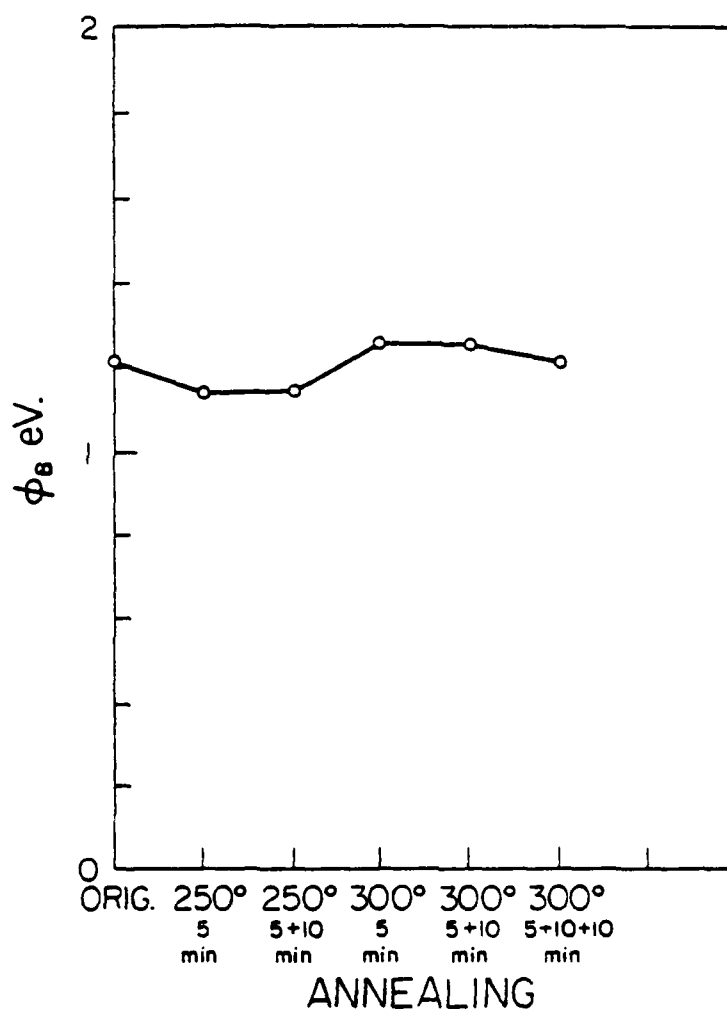
Figure 6.7 Variation of ϕ_B for Au-Sn diffused sample #5-4D after successive anneals for increasing times.
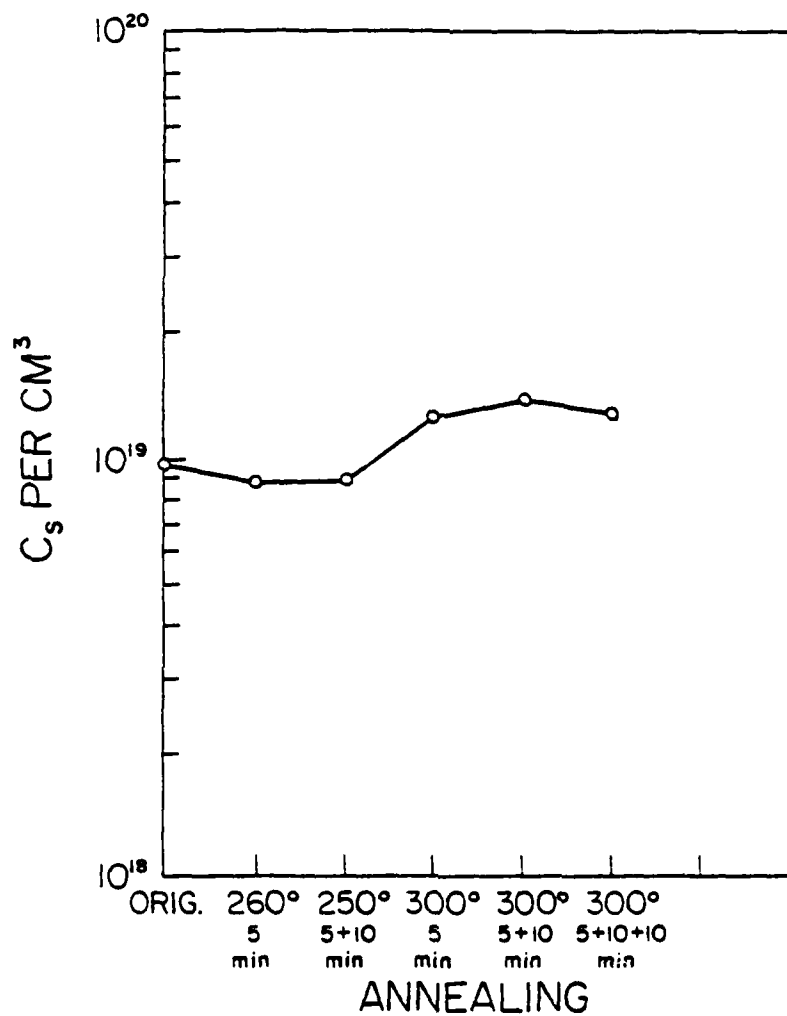
Figure 6.8 Variation of C_s for Au-Sn diffused sample #5-4D
after successive anneals for increasing times.

134

Figure 6.9   I-V response of Au-Ge sample # 5G-3 after
successive anneals.   T = 24°C.

Figure 6.10   I-V response of Au-Ge sample # 5G-2 after
successive anneals.   T = 26°C.

Figure 6.11 I-V response for Au-Ge sample # 7G-1 after
successive anneals. T = 25°C.
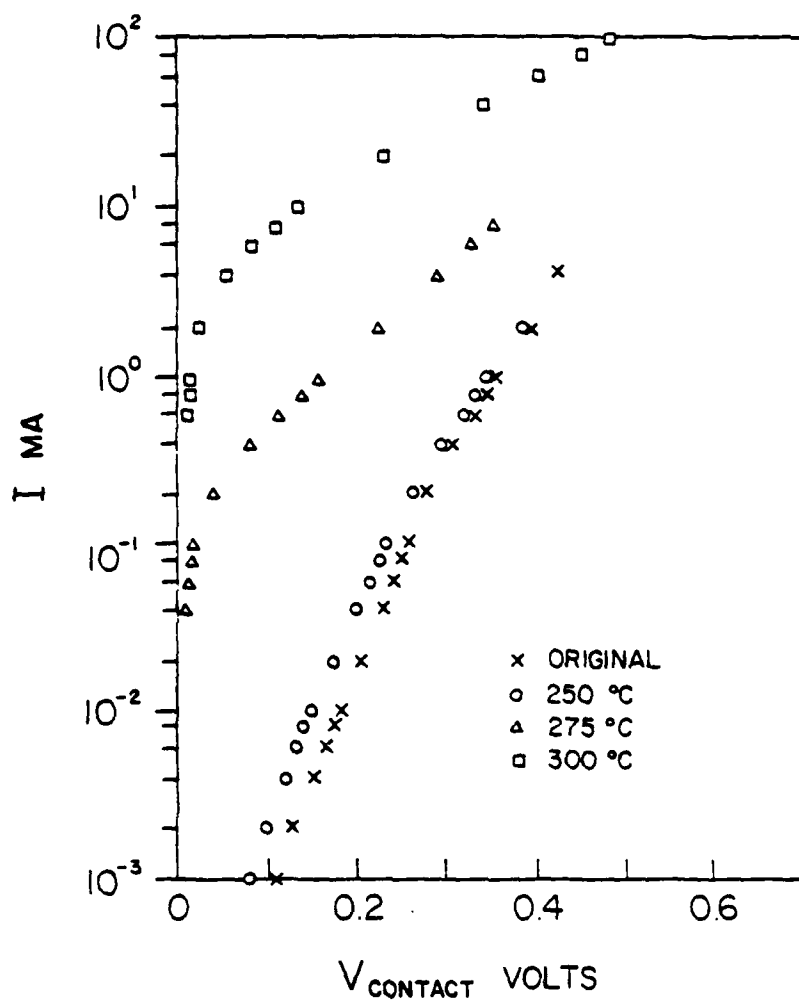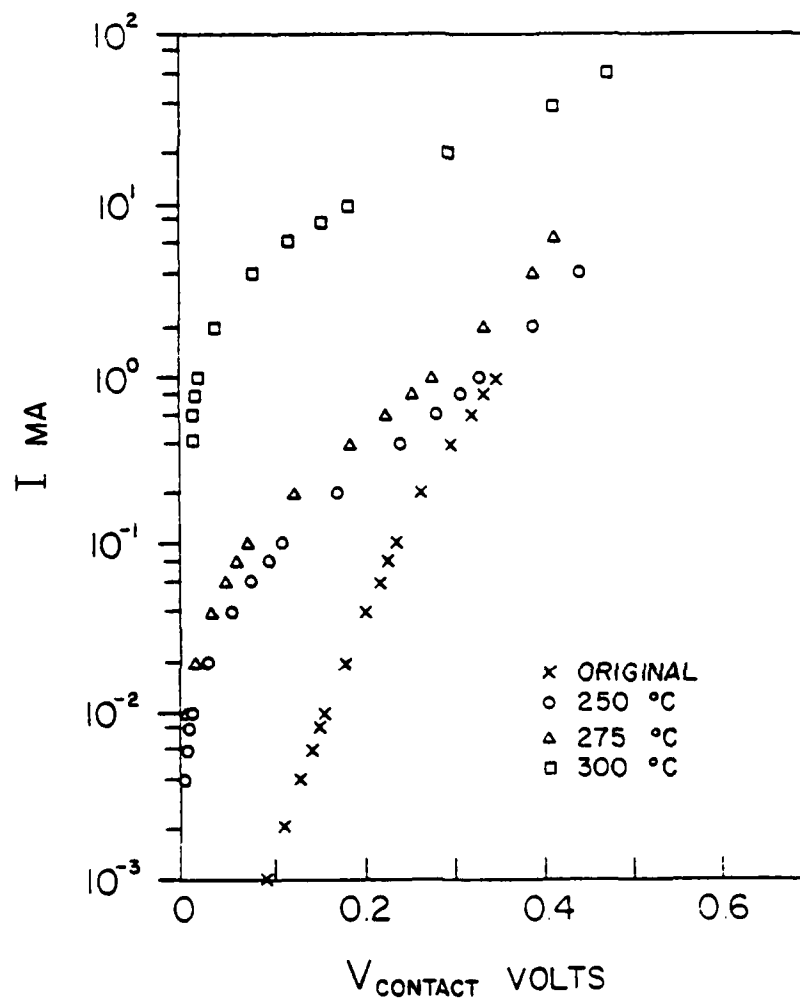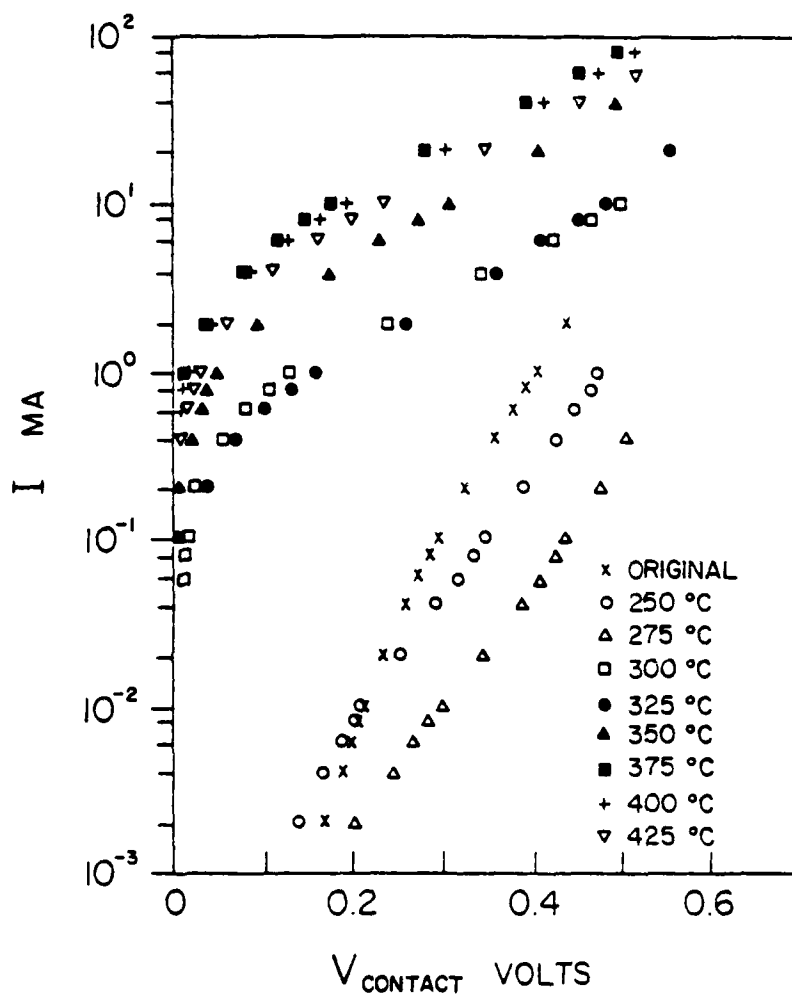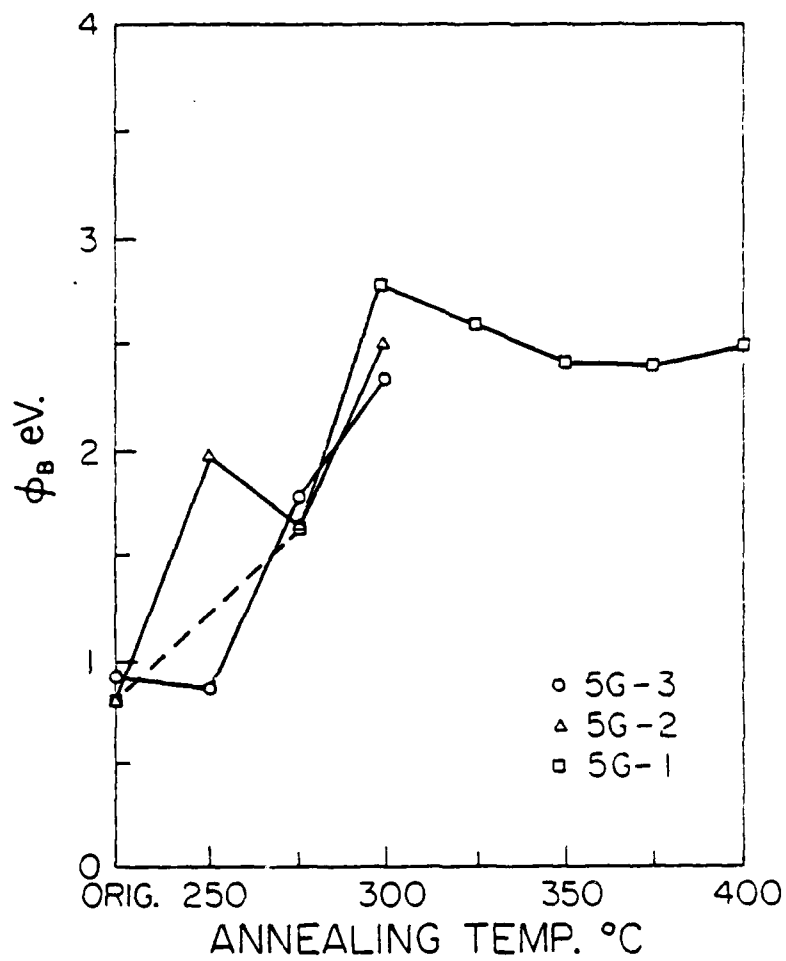
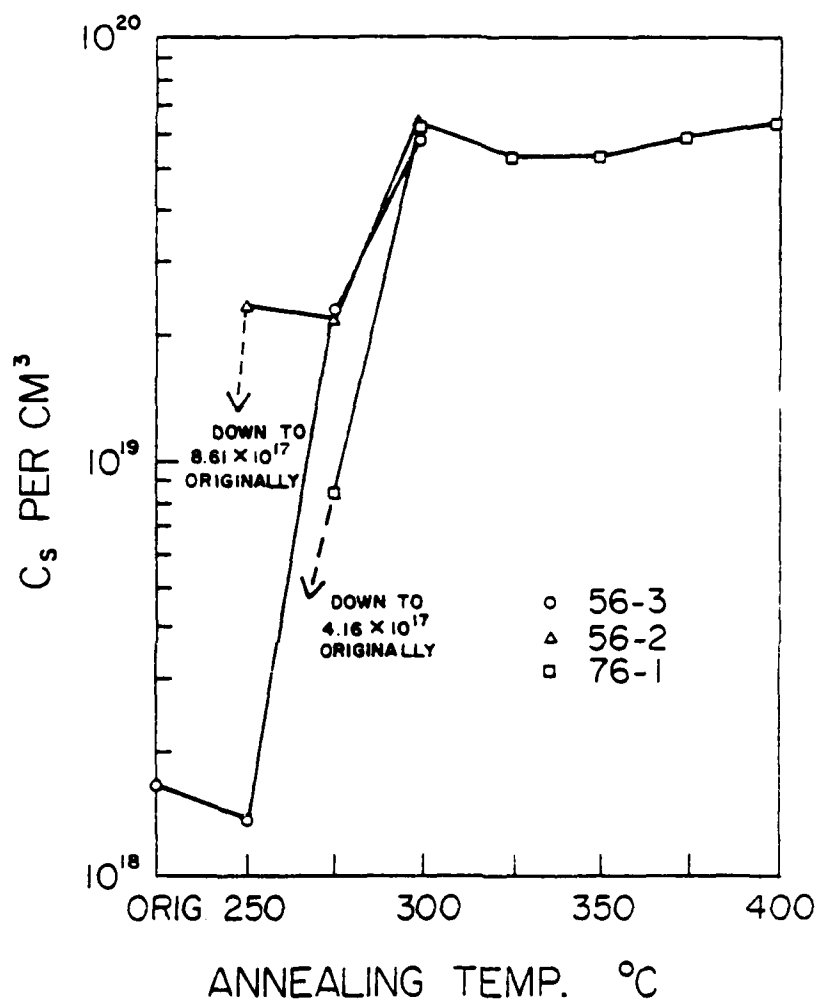Figure 6.12 Variation of ϕ_B for Au-Ge samples after
successive anneals.

Figure 6.13 Variation of C_s for Au-Ge samples after
successive anneals.

the original unannealed contacts are very similar for all samples and
yield a C_s value which matches closely with the original specified C_s.
The values of   are also in agreement but are slightly lower
than the 0.9 eV standard value.

The variation of C_s with annealing indicates an increase in C_s
with increasing temperature. This is to be expected if, as usually
assumed, the Ge is moving into the GaAs and acting like an n-type
dopant giving rise to a highly doped layer and increased tunneling. A
maximum temperature of $\approx$ 425° C was for the one case, used since
balling up of the Au was observed for higher temperatures. The
eventual value of C_s reached at a temperature of $\approx$ 300° C was
$\approx$ 5 ~ 6 x 10^{19}/cm³ and was nearly the same for all samples.

One problem with the data is the extraordinarily high values of
ϕ_B which resulted from the curve fit. They are clearly out of line
with a physically valid Schottky model. However, it is felt that these
high values are due to the presence of localized conduction pinholes
and arise from the manner in which the data is interpreted when pinhole
conduction is neglected.

Other researchers (19) have shown that alloyed Au-Ge contacts
have a problem with localized formation of various Au-Ge-GaAs phases
with their differing conduction properties. A conduction pinhole in
this case may be regarded as a localized area where rapid incorporation
of Ge has occured giving rise to a highly doped point in the GaAs
surface. This point then allows easier tunneling than the rest of the
surface and such points would effectively act as a current-hogging
points. Any current through the contact would essentially be confined
to these easily conducting pinholes and the measured I-V characteristic
would then indicate only the properties of the pinholes and not of the
entire Au contact area.

The problem concerning the data analysis arises when a value of
J_s is calculated for a given I-V experimental curve. The actual
quantity measured is a value of saturation current I_s and a value of
saturation current density, J_s , is calculated by dividing I_s by the
measured contact area. However, if the current is flowing mostly
through isolated pinholes then the I-V response reflects the values of
C_s and ϕ_B applicable to only those pinholes. For any single pinhole
supporting conduction of the test current I, the value of J_s is quite
large implying a much smaller ϕ_B. However, if the measured value of I_s
is divided by the total contact area, the main portion of which is not
supporting conduction, the apparent value of J_s is reduced which
results in a larger apparent value of ϕ_B.

Pinhole conduction does not affect the calculated value of C_s as
much as it did in the previous experiment on annealed Au contacts to Sn
diffused layers. The reason is that for the Au-Ge contacts the
substrate is much more highly conductive and the IR_s drops due to the

current flowing from an internal pinhole are negligible. That is, these IR_s drops do not cause the I-V response curve to be bent and therefore the slope is only slightly affected by the doping level.

The observed high values of ϕ_B for the Au-Ge case are probably not due to the effects of an interfacial oxide as was assumed to be the case in the diffused Sn layer case. One reason is that the unannealed contact data yielded a ϕ_B lower than expected. The presence of an oxide should have made this value greater. Also, the observed values do not progress through an initial period of decrease in ϕ_B and C_s as was seen before. Only increases are observed. The evaporation of the Ge appears to effectively remove any effects of an interfacial oxide layer.

The Schottky barrier model can be applied as a general guide to the analysis of Au-Ge alloyed contacts, but some strong reservations must be made in the interpretation of the data, as regards C_s and ϕ_B, because of the non exponential shape of the I-V response and the probably formation of isolated tunneling points.

BLANK PAGE

SECTION VII

OPTICAL MEASUREMENTS

The argon ion laser, dye laser, cavity dumper, and active mode
locking unit arrived in October of 1979. The assimilation of these
components into a synchronously pumped cavity dumped dye laser began in
late November and was completed in July of 1980. The installation of
the accousto-optic modelocker causes the argon ion laser to have a
pulsed output. The acousto-optic modelocker is driven by a stable RF
synthesizer. This RF signal produces an acoustic standing wave in the
acousto-optic crystal when the RF matches the resonance frequency of
the crystal. Since the acoustic wave velocity and crystal dimensions,
which determine the resonance frequency, are temperature dependent a
stable temperature controlled oven is installed around the crystal. By
modulating the cavity losses the mode-locker causes approximately 1000
modes to have a fixed phase relation. The interference of these modes
produces the pulsed output. The pulses are ~ 160 psec in length and
the interpulse spacing is 12 nsec. The maximum average power is 1W but
is usually run at 600 mW for stability and pulse length considerations.
Thus, the peak power is 45 W when the wavelength is 514.4 nm. The dye
currently being used in the dye laser is Rhodamine 6G. This dye will
produce output in the range from 550 to 650 nm with the peak power near
600 nm. The laser system is termed as being synchronously pumped, this
is achieved by lengthening the cavity of the dye laser until it matches
the length of the argon ion cavity. Thus the round trip time of pulses
travelling in both cavities is the same. The pulse length of a
modelocked laser is determined by the number of longitudinal modes
which can be locked together. By synchronously pumping, the gain
bandwidth of the dye laser is larger at the time tht the dye laser
pulse hits the dye jet. Thus the dye laser pulse can be and is much
shorter i.e. pulse lengths on the order of 1 psec are possible. Peak
power in these pulses extractable through a 10% mirror are on the order
of 50 W at 80 Mhz repition rate. However, also installed in the system
is a cavity dumper. The main mechanism of the cavity dumper is an
acousto-optic crystal which like the modelocker is driven by an RF
signal. However, this RF signal is pulsed producing a travelling wave
in the crystal. This RF pulse though longer than a round trip time of
the cavity is synchronized with the light pulse such that only one
pulse is dumped out per RF pulse. Since with the cavity dumper the dye
laser cavity is defined by only high reflectance mirrors higher
intracavity power is possible and a much greater fraction of
intracavity pulse power may be switched out giving a factor of 30

increase in output pulse peak power, i.e. the peak power is 1.5 kW with a repition rate up to 4 Mhz. The average power with the cavity dumper is specified to be 25-30 mW. These peak powers are, with optical focusing, sufficient to do optical excitation studies in solids.

In the proposed experiment small changes in the reflectivity of the material will be measured by a technique based on the principles of ellipsometry.[1] A typical block diagram of an ellipsometer is shown in Fig. 1. The plane polarized light from the laser is converted to circularly polarized by the first quarter wave plate, this ensures that the intensity does not vary as the polarizer P is rotated. The plane polarized light emerging from P then passes through the second retardation plate C which is oriented such that its fast axis is at 40° to the horizontal plane, which is also the plane of incidence. The emerging light is generally, elliptically polarized. On reflection from the sample surface, the two components of the electric field of the incident light $E_\perp$ and $E_\parallel$ undergo different changes in their respective amplitudes and phases. The reflected light passes through the analyser A and is detected by the photomultiplier tube (PMT). In the experiments P and A are rotated to such positions that the elliptically polarized light from C becomes linearly polarized after reflection from the sample surface and can then be extinguished by the analyzer A. In this configuration the angles that P and A make with the plane of incidence can be related to the (complex) refractive index of the sample. However, in the proposed experiment, the quantity of interest is the change in the refractive index of the material caused by the excitation of the electron-hole plasma. It can be shown [2], that for small changes δn in the refractive index, the intensity of light transmitted through the ellipsometer arrangement is proportional to $(\delta n/n)^2$. Thus if P and A are adjusted for extinction in the absence of the pump beam, then the change in the signal reaching the PMT when the pump beam is turned on can be used to calculate the change in the refractive index and thus the change in the electron-hole plasma density. This plasma density can be measured as a function of the delay between the pump pulse and the probe pulse yielding information about the relaxation time constants of the plasma.

The sensitivity of this procedure as reported in literature [2] is $\delta n/n < 10^{-3}$ and an initial change of 5% gave sufficient information to obtain characteristic time constants in the reported experiment. Taking into account the coupling of the pump beam energy to GaAs and its absorption constant at the laser wavelength (600 nm) the initial plasma density excited in the material can be estimated. Using the simple Drude model to relate the plasma density to the change in the refractive index, it was estimated that an energy density of 5 mJ/cm² would be required to produce the initial 5% change in the refractive index. The dye laser system is capable of providing energy of 30 nJ per pulse. Thus in order to obtain the required energy density it is necessary to focus the pump beam to a spot with dimensions of a few microns. It is also desirable that the probe beam should probe the
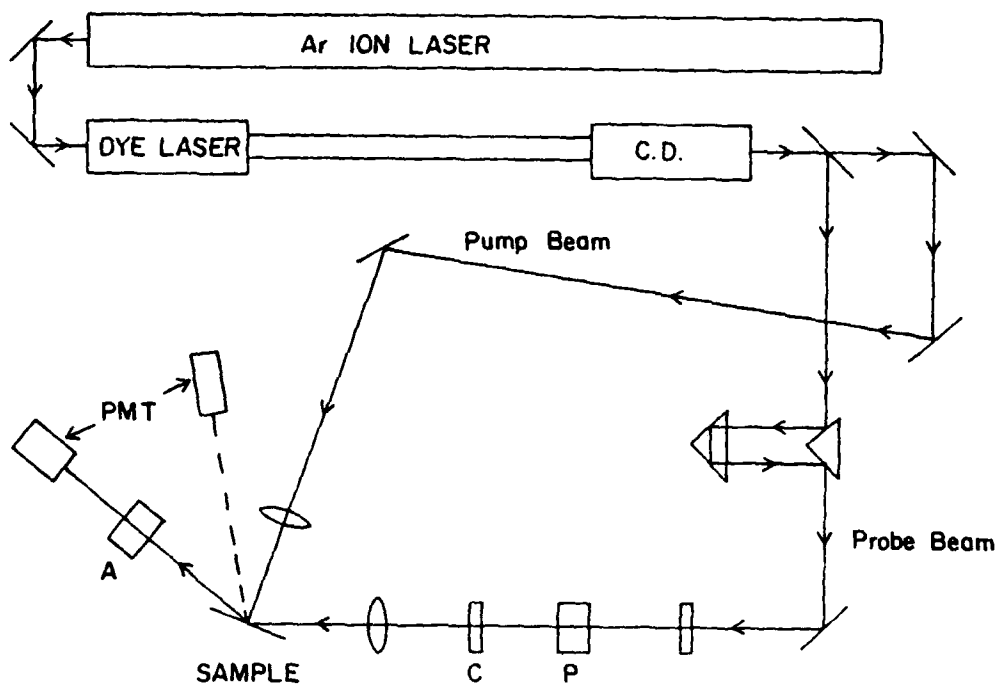
144

Figure 7.1 Block diagram of the ellipsometry arrangement
for measuring small changes in the reflectivity
of the sample as a function of delay between the
pump and the probe beams.

145

region of the sample where the pump beam excites the plasma. This makes it necessary to spatially overlap the two spots. Also in order to calculate the time constants of the material it is necessary to know the zero-delay position of the delay line.

The spatial and temperal overlap was obtained by maximizing the second harmonic signal, generated by a combined effect of the electric fields of the two beams in reflection from a (110) surface of GaAs.

In order to evaluate the sensitivity of the PMT (RCA 4837) in the uv range and to gain familiarity with the process of generating second harmonic light, a one beam experiment was initially performed. A block diagram of the experimental arrangement is shown in Fig. 2. The vertically polarized beam was reflected from the sample and the reflected primary beam was filtered out using two uv-pass glass filters. The transmitted light was detected by the PMT. The dye laser beam was chopped with a mechanical chopper which also provided the reference for the lock-in amplifier.

To confirm that the signal thus observed is due to the 300 nm second harmonic and not due to the residual transmittance of the 600 nm primary, the dependence of the signal on the angle Ψ between the (100) axis in the plane of the sample and the plane of incidence was studied. [3] The SH signal has two components, one polarized in the plane of incidence and the other polarized perpendicular to the plane of incidence. The reflected SH intensity can be calculated according to

$$I(2\nu) \quad I_\perp (2\nu) + I_\parallel (2\nu) \tag{7.1}$$

where $I_\perp (2\nu)$ is proportional to $(P_\perp NSL)^2$ and $I_\parallel (2\nu)$ to $(P_\parallel NLS)^2$. P^{NLS} are the non-linear polarizations induced by the electric field E_1 of the primary beam. The dependence of P^{NLS} on Ψ is given by:

$$P_\perp^{NLS} \quad = \quad 3/2 \; \chi^{NL} \; E_1^2 \; \sin^2 \Psi \; \cos \Psi \tag{7.2}$$

and

$$P_\parallel^{NLS} \quad = \quad 1/2 \; \chi^{NL} \; E_1^2 \; \sin \Psi \; (1-3 \cos^2 \Psi) \tag{7.3}$$

Here χ^{NL} is the non zero term in the second order non-linear susceptibility for GaAs.

Figure 3 shows the experimental data of $I(2\nu)$ as a function of Ψ, plotted along with the theoretical curve obtained from Equations 2 and 3. The theoretical curve has been scalled to account for the proportionality factor. Agreement between theory and experiment is excellent indicating that the observed signal is indeed the second harmonic.
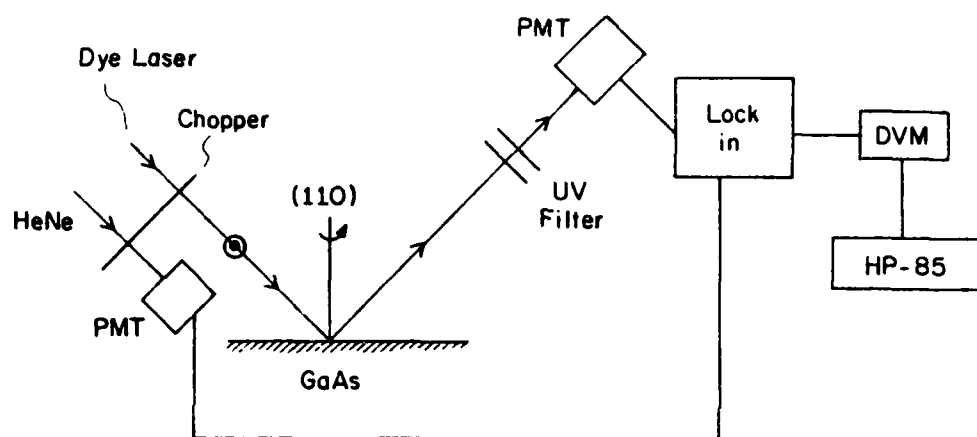
Figure 7.2 Block diagram of the experimental arrangement
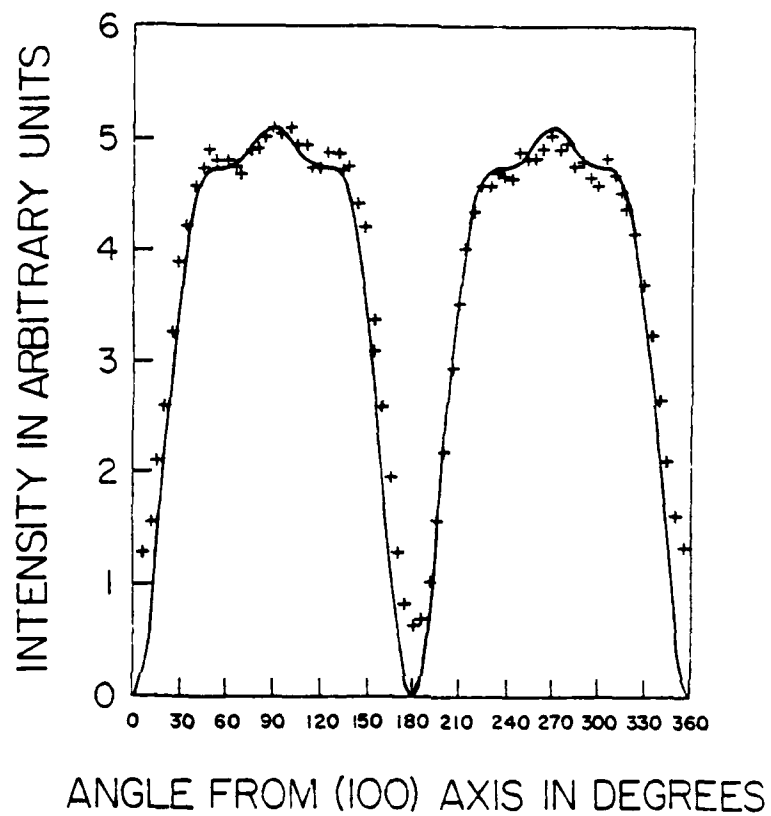for second harmonic generation for a GaAs crystal.

147

Figure 7.3   The intensity of the second harmonic signal generated
from GaAs as a function of the angle Ψ between the (100) axis and the
normal to the plane of incidence and reflection.

148

After observing the single beam second harmonic, a two beam experiment was performed. The angle θ_3 at which the SH signal appears is given by [4]

$$\sin \theta_3 = \frac{\sin \theta_1 + \sin \theta_2}{2}$$

where θ_1 and θ_2 are the angles of incidence of the two beams. In the initial experiment a beam splitter giving approximately equal intensities for the two beams was used. θ_1 and θ_2 were chosen to be of opposite sign so that the SH signal appeared near the film normal. A block diagram of the arrangement is shown in Fig. 4.

The observed signal was easily confirmed as being the SH by qualitatively observing its dependence on Ψ and comparing it to Fig. 3. To further evaluate the noise levels in the system and to check the alignment of the delay line, this SH signal was measured as a function of the delay introduced in one of the beams. The resulting curve duplicated the auto correlation trace obtained from the commercial unit (Spectra Physics 409) as shown in Fig. 5. The actual geometry to be used in the ellipsometry was then set up with the pump beam incident normally and the probe beam with an angle of incidence of 70°. Due to this shallow incidence, positioning the spots on the sample became more difficult requiring harder focusing and smaller lens mounts. A variable beam splitter was used in place of the fixed one in Fig. 4. After finding the SH signal with the two beams of approximately equal intensity, the ratio can be changed while tracking the SH signal. At the sample the probe beam can be made to be a factor of twenty weaker than the pump beam.

To numerically subtract the background signal caused by the probe beam scattered into the PMT and by the residual transmittance through the analyzer, a shutter controlled with the stepper motor is placed in the pump beam. This way, for each psoition of the delay line the output of the PMT can be measured with or without the pump beam striking the sample.

In any laboratory there are many pieces of apparatus necessary to perform the experiments successfully. In addition to the standard needs of lens, mirrors, mounts, and positioners several other mechanical and electrical devices have been acquired, built, and investigated for use.

Crucial to the experiments performed is the operation of an optical delay line. The difficulties are mechanical stability, reproducibility, and trueness of travel. The probe beam in the experiments passes through this delay line and then another meter to the sample. At the sample the beams are focused to 20 micron diameter spots. Thus it is necessary to have the delay line translate and be

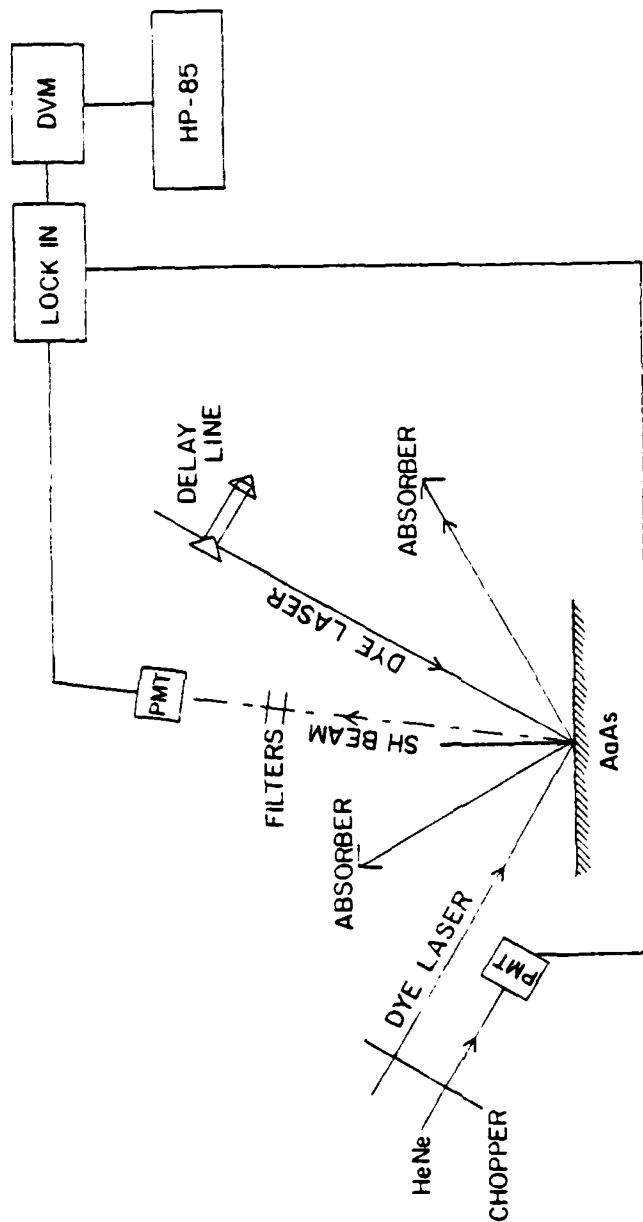Figure 7.4 Block diagram of the essential features of the system to detect two-beam second harmonic generation by reflection from the (110) surface of GaAs.
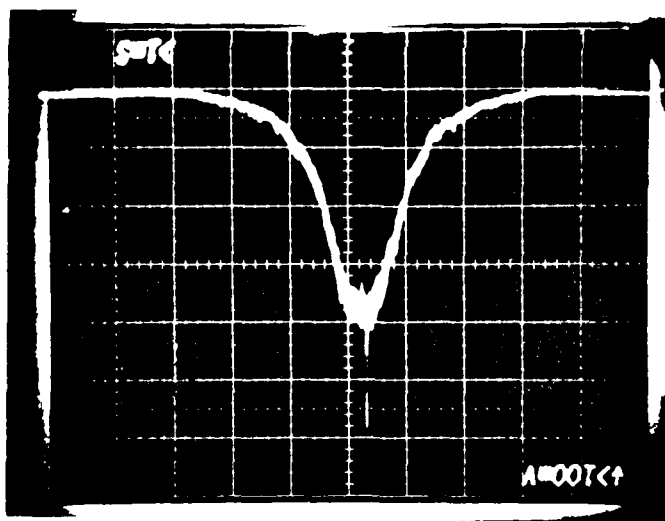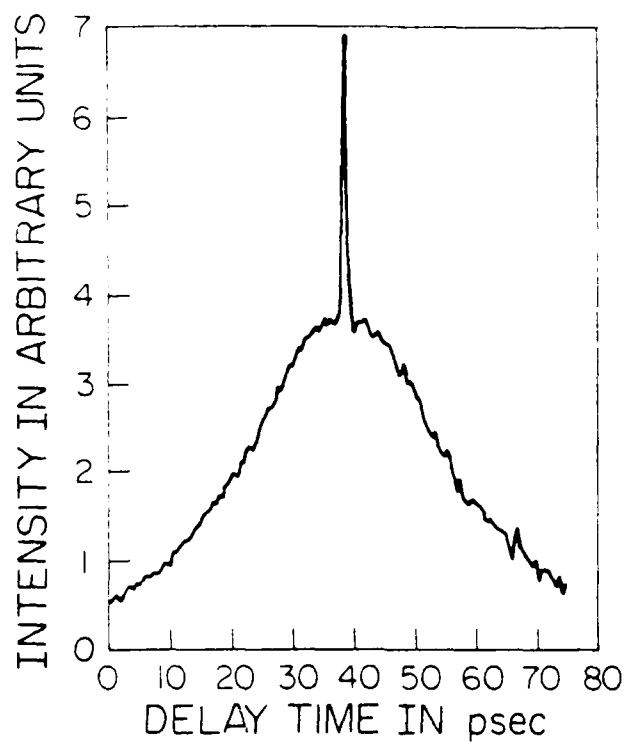
150

Figure 7.5 <u>Top</u>: Second harmonic intensity as a function of time delay between the two pulses in Figure 7.4.
<u>Bottom</u>: Auto correlation trace produced by a commercial system which employs second harmonic generation by transmission (20 psec/div. horizontal).

151

aligned very true in order to keep the two spots overlapped. Also this delay line is coupled to a stepper motor and provides the independent variable in the experiment. This has been accomplished by rebuilding a commercial translation stage and prism table with much stiffer springs, developing an alignment algorithm, using flexible and sliding coupling mechanisms, and building a positioning device to make the micrometer and stepper motor axes colinear. A significant advantage also is that the lens tends to reduce the magnitude of spot movement.

A device which was needed was designed and built here. In order to get small spot sizes it is necessary to use short focal length lenses. This causes a space restriction near to the sample. Mounts to hold small lenses near the sample and yet have the necessary degrees of freedom were not commercially available. A commercial system was reduced in size and more degrees of freedom were added to result in a positioning device 1 inch square and providing 5 degrees of freedom.

In order to facilitate a study of different samples and the use of separate materials for delay line calibration and actual measurements, a sample mount that allows the easy exchange of samples while retaining optical alignment by always bringing the front optical surface the sample into contact with a reference plane was designed and built. The reference plane can then be adjusted to bring its normal parallel to a rotational axis through the center of the sample. This rotational axis can then be swept, keeping a fixed orientation to the sample, to give optical alignment.

As expected we have found the signal to be small. Therefore the use of some type of signal recovery was demanded. Two methods have been employed. One being the use of a lock-in amplifier. A chopper wheel which also generates a timing signal was built to modulate the signal at a known frequency. The lock-in then only amplified signals which had the same specific frequency and phase. However, the lock-in detects mainly DC signals and so it only detected the average of one pulse over the duty cycle. This reduces the signal level by a factor of 100. Depending on the signal strength only marginal to acceptable results were obtained.

The second method used was a Boxcar integrator. The aperture over which the signal is integrated was held fixed in time with respect to the pulsed output and had a duration of 10 ns. With a pulse width of 10 ns and needing only an integral of the pulse this method should be much better than a lock-in since it is not affected by the low duty cycle. However the sensitivity of the Boxcar is much worse than the lock-in and in fact was not sufficient. A preamp for the Boxcar is being obtained which should correct this.

Before the completion of the stepper motor assembly, a few runs for data acquisition were made by manually controlling the delay

line and shutter. Although the data showed the expected trends, the scatter was too large for quantitative analysis. The actual data taking has so far been beset with problems, some of them minor, requiring modifications and rebuilding of machined parts. But other problems involving breakdowns in the laser system or malfunctions in the detector electronics required shipment of parts to the manufacturer causing delays of several weeks at a time.

Besides the ellipsometric technique described above in detail, other methods for measuring the life times are also being considered. Preparations for one type of experiment based on the Haynes-Shockley techqniue [5,6] are well under way.

The experiment would measure the transit time t of the minority carriers from the point of injection to the collector. The excess minority carrier density moves with a velocity v between the emitter and collector which are a distance d apart. Hence vt = d. A homogeneous field E is assumed between the emitter and the collector. If μ is the minority carrier drift mobility then v = μE or $\mu = \frac{v}{E} = \frac{d}{Et}$.

The traditional Haynes-Shockley experiment generates minority carriers by applying a short current pulse to an emitter contact whereas in the proposed experiment minority carriers are generated using a picosecond optical pulse. The injection point and hence the distance to the collector can be varried by steering the beam across the sample.

The sample consists of a rectangular block of GaAs, length 0.5 cm; width ~ 25 μm and thickness ~ 5 μm. Assuming a resistivity of (.01) Ω cm a resistance of 4 KΩ is obtained. A pulse generator providing 200 volt pulses was constructed. This will provide an electric field of 400 V cm^{-1}. The rationale behind preparing samples of as small a width and thickness possible is to obtain a high resistance. This, along with a pulsed field minimizes the heating effects As soon as technistrip-Au, an etchant for gold overlays existing on present samples, or a new batch of samples arrives the experiment will be performed.

The other method being considered involves the use of a CW source for the probe beam.[7] The pulsed pump beam and the CW probe beam, which can be obtained from a diode laser, hit the same area of the sample. The reflectivity of the material would change as a function of time after the arrival of the pump-pulse. The intensity of the reflected probe beam follows this change in the reflectivity (Fig. 6). This beam is mixed with a portion of the dye laser output in a nonlinear crystal. The sum frequency light generated in the crystal can be measured as a function of the delay between beam 1 and the pump beam to obtain information about the decay of the reflectivity of the semiconductor. This procedure would have the advantage of having the delay line on a beam that does not have to be focused as hard as in ellipsometry. Thus any misalignment of the delay line would not have
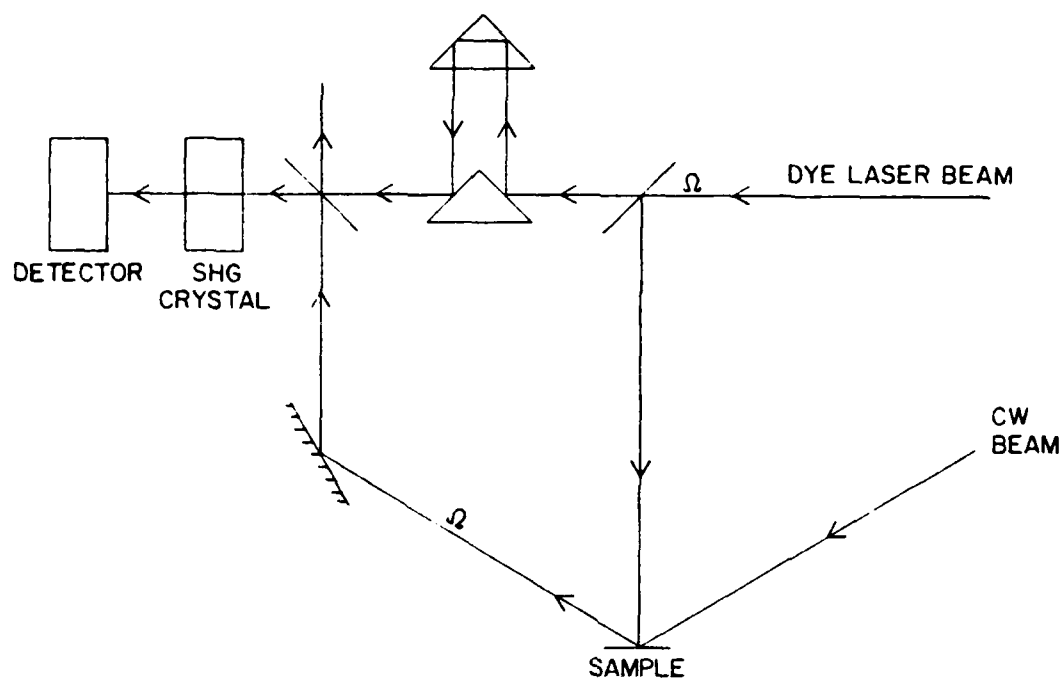
Figure 7.6 Block diagram of the essential features of the
proposed experiment to measure the reflectivity
of the sample using a CW beam as a probe.

154

as pronounced an effect on the data as observed in the llipsometry arrangement. Also, if the CW laser is chosen to have energy less than the band gap of the material, this experiment can easily be modified for transmission measurements. Towards performing this experiment, diode laser sources for the CW beam are being evaluated and calculations to find the most suitable non-linear material and its orientation for the cross-correlation are being undertaken.

REFERENCES

1. F.L. McCrackin, E. Passaglia, R.R. Stromberg, and H.L. Steinberg. J. of Res. of the National Bureau of Standards, 67A, 363 (1963).

2. D.H. Auston and C.V. Shank, Phys. Rev. Lett. 32, 1120 (1974).

3. J. Ducuing and N. Bloembergen, Phys.Rev.Lett. 10, 474 (1963).

4. R.K. Chang and N. Bloembergen, Phys. Rev., 144, 775 (1966).

5. J.R. Haynes and W. Shockley, Phys. Rev., 81, 835 (1951).

6. S. Middlehoek and M.J. Geerts, IEEE Trans. Educ. E-21, 31 (1978).

7. T. Gillbro and V. Sundstrom, Chem. Phys. Lett, 74, 188 (1980).

SECTION VIII

CONCLUSIONS

8.1 Research on non-annealed contacts

The aim of this research was to investigate the possible method
for fabricating non-alloyed, low resistance (ohmic) contacts to GaAs
and to determine whether the performance of such contacts could be
accurately characterized and predicted using a Schottky barrier model
with the inclusion of electron tunneling.

The initial step in the contact fabrication was the formation,
by high temperature diffusion, of a heavily doped Sn layer in the
surface of an p-type GaAs substrate. Testing of the characteristics of
this layer before the application of contact metal revealed the follow-
ing

1. The Sn diffused layer can be accurately character-
ized with an erfc profile.

2. Use of this erfc profile shape in the theoretical
prediction of average layer resistivity, $\bar{\rho}$, with
respect to surface dopant concentration, C_s, will
give results which can be experimentally verified.
However, some additional consideration is needed in
assuming a significantly lower value for electron
mobility in the diffused layer than would be
expected for bulk material.

3. The assumption of full ionization of Sn donors is
valid, even though the material is degenerate,
apparently because of the effects of band tailing
and impurity band formation.

4. At the diffusion temperature used, 950° C., a
maximum Sn surface concentration of $C_s = 2 \times
10^{19}/cm^3$ was observed, implying a solid solubility
limit for Sn in GaAs near this level. This
presents a direct limitation on the lowest value of
contact resistivity, R_c, obtainable for a contact
made to this doped surface.

157

After the Au contact metal was applied and the contact structure delineated, the contact was tested for its value of specific contact resistivity, R_c, using the transfer length method. Samples were tested for R_c over a temperature range of $T = -15°$ C to $T = 25°$ C to determine the R_c response to temperature. The current voltage (I-V) characteristics of the contact were measured and used as base data for a curve fit to theoretical I-V equations as developed from a Schottky barrier model for the contact. The theoretical equations gave the I-V response for the contact when field emission (FE) or thermionic field (TFE) type tunneling was present. These equations also formed the basis for the theoretical equations predicting R_c for the contact.

The above investigation revealed the following:

1. The theoretical equations predicting contact TFE or FE I-V response can be accurately fitted to the experimental I-V data for the contacts and this procedure yields values for the controlling parameters, C_s, and barrier height, ϕ_B. The values of C_s so obtained were verified from the previous $\bar{\rho}$ -Cs measurements. The values of ϕ_B were larger than expected and varied from the usually reported constant value of $\phi_B \approx 0.9$ eV. The higher values of ϕ_B are attributed to monolayers of interface oxide.

2. Use of the C_s and ϕ_B values, obtained from the I-V curve fit, in the calculation of a theoretical R_c vs. T response yielded results which fairly well matched experimental data. This means that the Schottky barrier model can adequately characterize non-alloyed contact tunneling behavior and can be used quantitatively in the study of such contacts to GaAs.

8.2 Research on annealed contacts

The above procedure was also applied to the analysis of selected Au-Sn doped GaAs contacts and Au-Ge-GaAs contacts which were given successive anneals from 250° C to ≈ 425° C and revealed the following:

1. Annealing tests on the Au-Sn doped GaAs contacts confirmed the existance of a thin (≈ 10Å) oxide layer between the Au and GaAs. This layer acts to increase the effective ϕ_B , and therefore raise R_c but does not substnatially effect the analytical application of the simple Schottky barrier model.

158

2. Annealing the Au-Sn doped contacts up to ≈ 300° C gradually removes the interfacial insulating layer or perhaps makes it a conductor.

3. Annealing above 300° C results in the formation of small iolated current conduction areas (conduction pinholes) which prevents further quantitative use of the Schottky model for accurate determination of C_S and ϕ_B .

4. Results from the annealed Au-Ge-GaAs contacts also were affected by the apparent formation of contact pinholes but it seems that successive annealings result in increasing C_S, due to the doping action of the Ge, up to $C_S ≈ 10^{19}$ /cm^3 . Results on ϕ_B were not conclusive.

5. For both cases, when annealing temperatures above 425 ~ 450° C were used, Au balling up and contact surface disruption were seen.

6. The Schottky tunneling model has limited usefulness in the analysis or prediction of contact perform-ance of annealed or alloyed contacts unless the processing is uniform over the interface area of the contact. However, the trend implied from the above investigation is that for alloyed contacts tunneling is the major phenomenon involved in causing ohmic performance. Whether or not the contact behaves as predicted by the simple Schottky model cannot be quantitatively verified with the experimental procedure used in this research.

8.3 Implications for improvement in contact performance

The verification, by this research, of the applicability of the Schottky tunneling model in the analysis of nonannealed contacts to GaAs allows for its straightforward use in trying to realize contact improvement. In order to obtain non-alloyed contacts with lower R_c, the model and theoretical equations point to two possibilities, lowered ϕ_B or increased C_S.

In view of the evidence favoring pinning of $\phi_B ≈ 0.9$ eV, lowering ϕ_B appears unlikely. However, this research has shown that the presence of interfacial oxides, on the order of only 10 Å , can effectively increase ϕ_B and therefore increase R_c. The implication is

159

that contact processing is therefore extremely critical in the case of non-alloyed contacts to avoid the formation and subsequent detrimental effects of thin interfacial oxide layers.

If a ϕ_B value of ≈ 0.9 eV is the lowest value obtainable then only an increase in C_S will give lower values of R_C for non-alloyed contacts. As mentioned before, for a desired range of $R_C \approx 10^{-6} \Omega$-cm^2, with ϕ_B 0.9 eV, the above implies that C_S on the order of 10^{20}/cm^3 is needed. Obtaining this large of a value by normal diffusion or implantation techniques with tin seems highly improbable because of the solid solubility limits. Perhaps a combination of short period dopant diffusions (predepositions) or implantations and subsequent short period surface melting and regrowth would concentrate the dopant into a thin surface layer with a C_S above the equilibrium solubility limit.

It may also be possible to find other donors or combinations of donors with higher solubility limits. Since the literature on solubility limits in GaAs is somewhat limited this would be a good area for further research.

Another very important, but experimentally and theoretically difficult topic for further research is the nature of the band structure in the transition region between the metal and semiconductor. Even for very moderate annealing temperatures it is known that there is not a sharp transition from metal to gallium arsenide, but rather a complex interpenetration for a distance of at least a few attice constants. For such a transition the potential barrier would probably not be sharply peaked and under some conditions might be reduced to a low value resulting in good quality contacts.

LIST OF REFERENCES

1. Rideout, V.L., "A review of the Theory and Technology for Ohmic Contacts to Group III-V Compound Semiconductors," Solid State Elec., 18, 541, (1975).

2. Yoder, M.N., "Ohmic Contacts to GaAs," Solid State Elec., 23, 117, (1980).

3. Eckhardt, G., "Overview of Ohmic Contact Formation on N-type GaAs by Laser and Electron Beam Annealing," in Laser and Electron Beam Processing of Materials, Academic Press, New York, (1980).

4. Rhoderick, E.H., Metal-Semiconductor Contacts, Clarendon Press, Oxford, (1978).

5. Mott, N.F., Proc. Camb. Phil. Soc., 34, 568, (1938).

6. Schottky, W., Naturwiss, 26, 843, (1938).

7. Bethe, H.A., MIT Radiation Lab., Report 43-12, (1942).

8. Crowell, C.R. and Sze, S.M., "Current Transport in Metal-Semiconductor Barriers," Solid State Elec., 8, 395, (1965).

9. Sze, S.M., Physics of Semiconductor Devices , John Wiley and Sons, New York, (1969).

10. Nordheim, L., "The Effect of Image Force on the Emission and Reflexion of Electrons by Metals, Proc. Roy, Soc., (London), A121, 626, (1928).

11. Padovani, F.A. and Stratton, R., "Field and Thermionic Field Emission in Schottky Barriers," Solid State Elec., 9, 695, (1966).

12. Crowell, C.R. and Rideout, V.L., "Normalized Thermionic-Field (T-F) Emission in Metal-Semiconductor (Schottky) Barriers," Solid State Elec., 12, 89, (1969).

13. Chang, C. ., and Sze, S.M., "Carrier Transport Across Metal-Semiconductor Barriers," Solid State Elec., 13, 727, (1970).

14. Padovani, F.A., "The Voltage-Current Characteristics of Metal-Semiconductor Contacts", in Semiconductors and Semimetals, Editors: Willardson, R.K. and Beer, A.C., Vol. 7, Part A, 75, Academic Press, New York, (1971).

15. Yu, A.Y.C., "Electron Tunneling and Contact Resistance of Metal-Silicon Contact Barriers," Solid State Elec., 13, 239, (1970).

16. Chang, C.Y., Fand, Y.K., and Sze, S.M., "Specific Contact Resistance of Metal-Semiconductor Barriers," Solid State Elec., 14, 541, (1971).

17. Cox, R.H. and Strack, H., "Ohmic Contacts for GaAs Devices," Solid State Elec., 10, 1213, (1967).

18. Klohn, K.L. and Wandinger, L., "Variation of Contact Resistance of Metal-GaAs Contracts with Impurity Concentration and its Device Implication," Jour. Elec. Soc., 116, 507, (1969).

19. Gyulai, J., et. al., "Alloying Behavior of Au and Au-Ge on GaAs," J. Appl. Phys., 42, 3578, (1971).

20. Otsubo, M., Kumabe, H., and Miki, H., "Liquid Phase Epitaxial Growth of GaAs from Au-Ge-Ni Melts," Solid State Elec., 20, 617, (1977).

21. Anderson, W.T., Cristou, A., and Davey, J.E., "Development of Ohmic Contacts for GaAs Devices Using Epitaxial Ge Films," IEEE Jour. Solid State Circ., SC-13, 430, (1978).

22. Guha, S., Arora, B.M., and Salvi, V.P., "High Temperature Annealing Behavior of Schottky Barriers on GaAs with Gold and Gold-Gallium Contacts," Solid State Elec., 20, 431, (1977).

23. Inada, T., et.al., "Ohmic Contacts on Ion Implanted N-type GaAs Layers, J. App. Phys., 50, 4466, (1979).

24. Madams, C.J., Morgan, D.V., and Howes, M.J., "Outmigration of Gallium from Au-AuGaAs Interfaces," Elec.Lett., 11, 574, (1975).

25. Sinha, A.K. and Poate, J.M., "Effect of Alloying Behavior on the Electrical Characteristics of N-GaAs Schottky Diodes Metallized with W, Au, and Pt," App. Phys. Lett., 23, 666, (1973).

26. Kim, H.G., Sweeney, G.C., and Heng, T.M.S., "Analysis of Metal-GaAs Schottky Barrier Diodes by Secondary Ion Mass Spectrometry," in Gallium Arsenide and Related Materials, Inst. of Physics, London, (1975).

27. Barnes, P.A. and Cho, A.Y., "Non-Alloyed Ohmic Contacts to N-GaAs by Molecular Beam Epitaxy," Appl. Phys. Lett., 33, 651, (1978).

28. DiLorenzo, J.V., Niehaus, W.C., and Cho, A.Y., "Nonalloyed and in situ Ohmic Contacts to Highly Doped N-Type GaAs Layers Grown by Molecular Beam Epitaxy (MBE) for Field Effect Transistors," J.Appl. Phys., 50, 951, (1979).

29. Mozzi, R.L., Fabian, W., and Piekarski, F.J., "Nonalloyed Ohmic Contacts to N-GaAs by Pulse-Electron-Beam Annealed Selenium Implants," Appl. Phjys. Lett., 35, 337 (1979).

30. Nissium, Y.I., Gibbons, J.F., and Gold, R.B., "Non-alloyed Ohmic Contacts to N-GaAs by CW Laser-Assisted Diffusion from a SnO2 / Si2 Source," IEEE Trans. on Elec. Dev., ED-28, No. 5, 607, (1981).

31. McCaldin, J.O., McGill, T.C., and Mead, C.A., "Correlation for III-V and II-VI Semiconductors of the Au Schottky Barrier Energy with Anion Electronegativity," Phy.Rev.Lett., 36, 56, (1976).

32. Amith, A. and Mark, P., "Schottky Barriers on Ordered and Disordered Surfaces of GaAs (110)," Jour. Vac. Sci. Tech., 15, 1344, (1978).

33. Brillson, L.J., "Chemical Reaction and Charge Redistribution at Metal-Semiconductor Interfaces," Jour. Vac. Sci. Tech., 15, 1378, (1978).

34. Lindau, I., et. al., "New Phenomena in Schottky Barrier Formation on III-V Compounds," Jour. Vac. Sci. Tech., 15, 1332, (1978).

35. Lindau, I., et. al., "The Interaction of Thin Au and Al Overlayers with the GaAs (110) Surface," Surface Science, 99, 192, (1980).

36. Schuldt, S.B., "An Exact Derivation of Contact Resistance to Planar Devices," Solid State Elec., 21, 715, (1978).

37. Fang, Y.K., Chang, C.Y., and Su, Y.K., "Contact Resistance in Metal Semiconductor Systems, " Solid State Elec., 22, 933, (1979).

38. Bardeen, J., "Surface States and Rectification at a Metal Semi-conductor Contact, Phys., Rev., 71, 717 (1947).

39. Stratton, R.J., "Volt-Current Characteristics for Tunneling Through Insulating Films," Four. Phys. Chem. Solids, 23, 1177, (1962).

40. Stratton, R., Lewicki, G., and Mead, C.A., "The Effect of Non-Parabolic Energy Bands on Tunneling Through Thin Insulating Films," Jour. Phys. Chem. Solids, 27, 1599, (1966).

41. Stratton, R., "Theory of Field Emission from Semiconductors," Phys. Rev., 125, No. 1, 67, (1962).

42. Murphy, E.L., and Good, R.H., "Thermionic Emission, Field Emission, and the Transition Region," Phys. Rev., 102, No. 6, 1464, (1956).

43. Gibbon, C.F., and Ketchow, D.R., "Diffusion of Tin into GaAs from Doped SiO2 Film Sources," Jour. Elec. Soc., 118, 975, (1971).

44. Tuck B. and Badawi, M.H., "Diffusion of Tin in N-Type GaAs," Jour. Phys. D., 11, 2541, (1978).

45. Baliga, B.J. and Ghandi, S.K., "Planar Diffusion in Gallium Arsenide from Tin Doped Oxides," Jour. Elec. Soc., 126, 135, (1979).

46. Nissim, Y.D., et. al., "Thermal Diffusion of Tin in GaAs from a Spin-on SnO2/SiO2 Source," Appl. Phys. Lett., 37, 89, (1980).

47. Emulsitone Co., 19 Leslie Court, Whippany, N.J. 07981.

48. Safe-t-Stain, type DSS-1, Philtec Instrument Co., 608 Carpenter Lane, Phila, Pa. 19119.

49. van der Pauw, L.J., "A Method of Measuring Specific Resistivity and Hall Effect of Discs of Arbitrary Shape," Philips Resch. Repts., 13, 1, (1958).

50. Irvin, J.C., "Resistivity of Bulk Silicon and of Diffused Layers in Silicon," Bell System Tech. J., 41, 387, (1962).

51. Grove, A.S., Physics and Technology of Semiconductor Devices, John Wiley and Sons, New York, (1967).

52. Sze, S.M., and Irvin, J.C., "Resistivity, Mobility, and Impurity Levels in GaAs, Ge, and Si at 300 K," Solid State Elec., 11, 599, (1968).

53. Spenke, E., Electronic Semiconductors, McGraw Hill, New York, (1958).

54. Fetterman, H.R., et. al., "Identification of Donor Species in High Purity GaAs Using Optically Pumped Submillimeter Lasers," App. Phys. Lett., 21, 434, (1972).

55. Baliga, B. J., "Conductivity of Complementary Error Function N-Type Diffused Layers in Gallium Arsenide," Solid State Elec., 20, 321, (1977).

56. Battocletti, F.E., "Polynomial Approximation of the Fermi Integral, " Proc. of the IEEE, 12, 2162, (1965).

57. Fistul, V.I., Heavily Doped Semiconductors, Plenum Press, New York, (1969).

58. Madelung, O., Physics of III-V Compounds, John Wiley and Sons, New York, (1964).

59. Blakemore, J.S., Semiconduction Statistics, Pergamon Press, New York, (1962).

60. Hower, P.L., et. al., "The GaAs Field Effect Transistor," in Semiconductors and Semimetals, Editors: Willardson, R.K. and Beer, A.C., Vol. 7, Part A, 147, Academic Press, New York, (1971).

61. Berger, H.H., "Models for Contacts to Planar Devices," Solid State Elec., 15, 145, (1972).

62. Thornton, R.D., et. al., Characteristic and Limitations of Transistors, John Wiley and Sons, New York, (1966).

63. van der Ziel, A., Solid State Physical Electronics, Prentice Hall, New Jersey, (1968).

64. Crystal Specialties, 419 W. Maple Ave., Monrovia, CA. 91016.

65. McColl, M., Millea, M.F., and Mead, C.A., "Zero-Bias Contact Resistance of Au-GaAs Schottky Barriers," Solid State Elec., 14, 677, (1971).

66. Fane, R.W. and Goss, A.J., "The Diffusion of Tin and Selenium in Gallium Arsenide," Solid State Elec., 6, 383, (1963).

67. Kendall, D.L., "Diffusion," in Semiconductors and Semimetals, Editors: Willardson, R.K., and Beer, A.C., Vol. 4, 163, Academic Press, New York, (1968).

68. Casey, H.C., "Diffusion in the III-V Compound Semiconductors," in Atomic Diffusion in Semiconductors, Editor: Shaw, D., Plenum Press, London, (1973).

69. Goldstein, B. and Keller, H., "Diffusion of Tin in Gallium Arsenide," J. Appl. Phys., 32, 1180, (1961).

70. Squire, W., Integration for Engineers and Scientists, American Elsevier, New York, (1970).

71. Ashok, S., Borrego, J.M., and Guttmann, R.J., "Electrical Characteristics of GaAs MIS Schottky Diodes," Solid State Elec., 22, 621, (1979).

72. Chye, P.W., et. al., "Oxygen Sorption and Excitonic Effects on GaAs Surfaces," Jour. Vac. Sci. Tech., 14, 917, (1977).

FILMED

8-8